Development of the x-ray standing waves methodology to probe the interfaces of periodic multilayers

Meiyi Wu

To cite this version:

Meiyi Wu. Development of the x-ray standing waves methodology to probe the interfaces of periodic multilayers. Theoretical and/or physical chemistry. Sorbonne Université, 2018. English. NNT : 2018SORUS175 . tel-01930509v2

HAL Id: tel-01930509
https://theses.hal.science/tel-01930509v2

Sorbonne Université

Ecole doctorale 388

Laboratoire de Chimie Physique - Matière et Rayonnement

Development of the x-ray standing waves methodology to probe the interfaces of periodic multilayers

Par Meiyi Wu

Thèse de doctorat de Chimie Physique et Chimie Analytique

Dirigée par Dr. Philippe Jonnard

Présentée et soutenue publiquement le 14 Septembre 2018

Devant un jury composé de :

M.	Michel Goldmann	Professeur	Rapporteur
Mme.	Marie-Christine Lépy	Directrice de recherche	Rapporteuse
M.	Franck Delmotte	Professeur	Examinateur
M.	Philippe Walter	Directeur de recherche	Examinateur
Mme.	Regina Soufli	Rechercheur	Examinatrice
M.	Ian Vickridge	Directeur de recherche	Examinateur invité
M.	Philippe Jonnard	Directeur de recherche	Directeur de thèse

This thesis is dedicated to my beloved parents.

To my father Jianming Wu who taught me to be respectful and curious about this world, who showed me the wisdom hidden within our history and culture and who demanded me not only to read the books but also to question them.

And to my mother Yan Mei, a strong and gentle woman who risked her own life giving birth to me. I honor you with my name and every single achievement I have.

仅以此文献于我敬爱的父母。

献给我的父亲吴建明。他教导我敬畏自然、求知于世，为我展现从历史和文化中萃取的智慧并激励我勤读书而不尽信书。

献给我坚强而善良的母亲梅艳。她置自身安危不顾让我来到这个世界。我愿以我之名以及我一切成就向她致敬。

Prepare for the battle constantly, win it with creativity.

-- Military Theory of Sunzi

以正合，以奇胜。

——孙子兵法

Remerciements

Cette thèse synthétise le travail de trois années d'octobre 2015 à septembre 2018 au Laboratoire de Chimie Physique-Matière et Rayonnement (LCPMR) [Université Pierre et Marie Curie puis Sorbonne Université et CNRS (UMR7614)]. Je tiens tout d'abord à remercier le directeur du laboratoire Alain Dubois pour m'avoir accueilli. Merci aux membres de mon jury d'avoir accepté la tâche d'évaluer mon travail.

Tous mes remerciements vont à Philippe Jonnard, mon directeur de thèse. Je pense avoir appris beaucoup à son coté grâce à son expérience scientifique. Son attitude très sérieuse pour la science m'a toujours inspiré. Je le remercie pour sa disponibilité et sa confiance quant à ce travail, pour son enseignement et sa gentillesse que j'ai pu apprécier, pour ses aides et ses précieux conseils pour mes difficultés pas seulement dans ma recherche scientifique mais aussi dans ma vie quotidienne en France. Je lui adresse ici le témoignage de mon plus profond respect et de ma plus vive reconnaissance.

J'adresse mes sincères remerciements à Jean-Michel André pour m'avoir guidé avec attention et gentillesse pendant ces trois années. Ses qualités scientifiques et humaines ont largement contribué à l'aboutissement de cette thèse.

Je tiens tout particulièrement à remercier Karine Le Guen pour ses nombreux conseils avisés et ses aides qui m'ont apportée dans la réalisation de cette thèse et dans ma mission d'enseignement dans notre université.

Je remercie grandement Stefano Nanaronne qui m'a accueilli sur la ligne BEAR du Synchrotron Elettra à Trieste et pour les discussions très utiles concernant les expériences réalisées chez eux. Merci également à Angelo Giglia et Konstantin Koshmak pour leurs participations à plusieurs projets scientifiques, pour la qualité des expériences et aussi pour notre précieuse amitié.

Je désire remercier Ian Vickridge de l'Institut des NanoSciences de Paris (INSP) de m'avoir permis de travailler à la plate-forme SAFIR sur le projet d'émissions générées par faisceaux d'ions et observées en mode Kossel. Suite à sa recommandation j'ai pu obtenir ma première invitation pour une presentation orale à la conférence IBA2017. Cela fut une étape importante pour moi. Merci également pour Didier Schmaus et tous autres collaborateurs de l'INSP pour leur participation au projet avec beaucoup d'attention.

Je tiens à remercier Zhanshan Wang (王占山), Qiushi Huang (黄秋实), Runze Qi (齐润泽) et Xiaowei Yang (杨笑微) de IPOE (Institute of Precision Optical Engineering, Tongji University, China) pour nos différentes collaborations sur l'étude des multicouches, pour les communications et discussions, et aussi pour les échantillons de haute qualité fabriqués chez eux.

Je souhaite remercier les membres du groupe OPTIQUE XUV de Laboratoire Charles Fabry de l'Institut d'Optique. Franck Delmotte pour m'avoir enseigné les techniques de dépôt des échantillons et de caractérisation des couches minces; Françoise Bridou pour me permettre d'utiliser FLUORT, le code de calcul de la fluorescence sous effet d'ondes stationnaires qui joue un rôle très important pour la partie de simulation dans cette thèse; Catherine Burcklen pour les nombreuses discussions constructives.

Je voudrais remercier Franz Schäfers, Andrey Sokolov et Mewael Sertsu à la ligne Optics de Synchrotron BESSY-II à Berlin et Elena O. Filatova de Saint Petersburg State University pour leur collaboration sur le projet sur des multicouches Mg/Co. Leur attitude de travail passionnante m'a beaucoup inspiré.

Merci également à Jean-Pascal Rueff à la ligne GALAXIES de Synchrotron SOLEIL à Saint-Aubin pour son guide et sa participation sur l'expérience au projet sur l'étude des multicouches Pd/Y.

Je remercie Marie-Christine Lépy à la ligne METROLOGIE de Synchrotron SOLEIL à Saint-Aubin pour sa disponibilité et son aide et d'avoir accepté d'être rapporteur de mon travail de thèse.

Merci à Philippe Walter de Laboratoire d'Archéologie Moleculaire et Structurale (LAMS) pour sa collaboration qui nous aide à améliorer la technique PIXE-Kossel.

Je tiens à remercier Emiliano Principi et Alberto Simoncig à la ligne de laser d'électron libre (FEL) FERMI à Trieste pour diriger mon travail chez eux.

Je remercie Birgit Kanngießer, Ioanna Mantouvalou et Veronika Szwedowski-Rammert de BLiX (Berlin Laboratory for innovative X-ray Technologies) pour leur collaboration sur la diffraction Kossel des multicouches irradiées par rayons X.

Plus généralement, je remercie l’ensemble du personnel du LCPMR pour l’ambiance de travail chaleureuse et conviviale. Ma reconnaissance s’adresse particulièrement à toute l’équipe des thésards: Alaaeldine, Carla, Hang, Jiaping, Jiatai, Junwen, Moustafa, Mehdi, Xuan, ...

Mes remerciements vont aussi à mes proches, famille, belle-famille et amis qui m’ont constamment supporté dans tous les sens du terme. J’adresse particulièrement mes profonds remerciements à mon épouse, Chujiao Li, pour partager sa vie avec moi et m’avoir accompagné durant ces trois années.

Je remercie mon chat Pudding pour sa compagnie pendant ces trois ans.

Content

Chapter 1: Periodic multilayer mirrors for X-ray

In this chapter, we start by introducing X-ray range, a special range in the electromagnetic spectrum. Following the presentation of X-rays are the periodic multilayer mirrors, which are the main research subject of this thesis. A principal description is given as well as their fabrication methods. We close the chapter by discussing the performance of the mirrors and their applications.

1.1 General introduction to X-rays

An electromagnetic radiation is classified by its energy or wavelength. As presented in Figure 1, from long to short wavelength (or from low to high energy) there are radio waves, microwaves, infrared rays (IR), visible light, ultraviolet rays (UV), X-rays and gamma rays. The discovery of X-rays dates back to the end of the 19th century. X-rays were first observed emitted from Crookes tubes invented around 1875 [1]. But the credit of the discovery is given to German physicist Wilhelm Röntgen for systematically studying them [2]. The great application potential soon drew much attention ever since the famous “medical” X-ray image of the hand of Röntgen’s wife. Other than medical uses, X-rays have also many notable applications in domains such as security control, astronomy and materials science.

X-rays have an energy ranging from 100 eV to 100 keV between UV and gamma rays, corresponding to wavelengths from about 0.01 to 10 nm. They can be divided into soft and hard X-rays due to their penetration abilities. X-rays with high photon energies above 5-10 keV (or below 0.2-0.1 nm in wavelength) are called hard X-rays, while the X-rays that have lower energies are called soft X-rays.

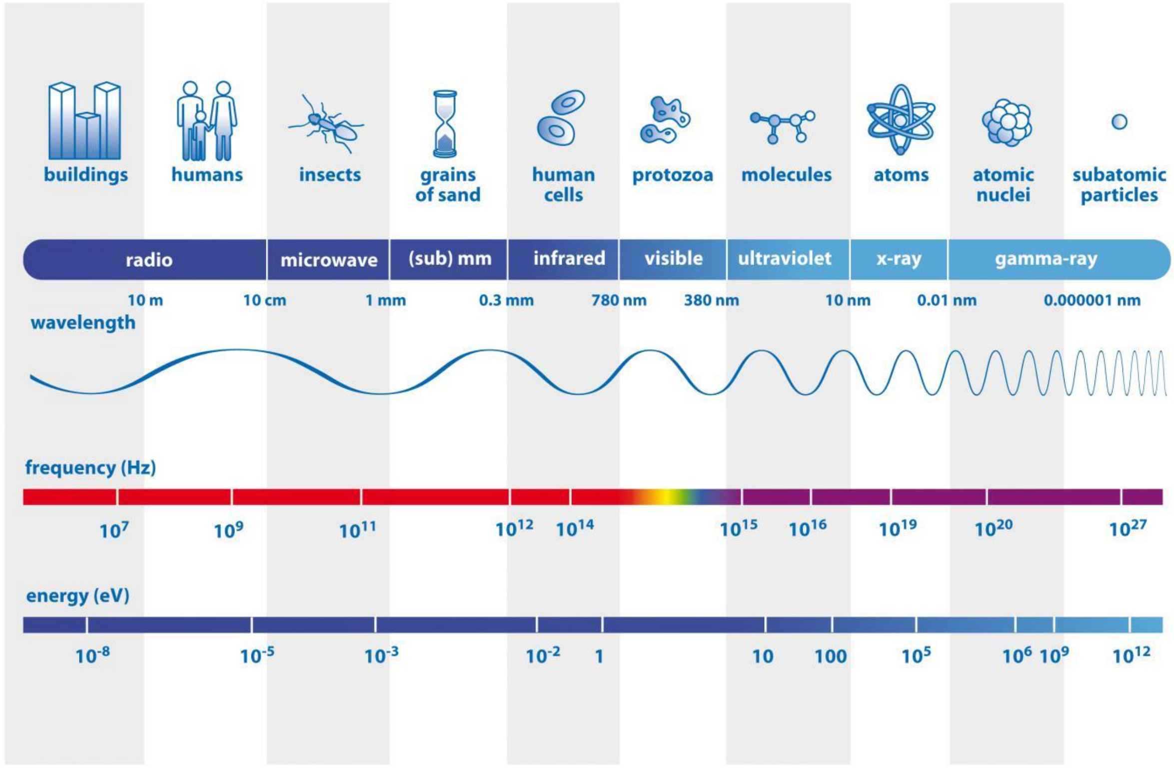

Figure 1.1: Classification of electromagnetic radiations.

Source: [http://solar-center.stanford.edu/about/uvlight.html]

The propagation of X-rays, as well as other electromagnetic waves, in a material can be briefly and classically described by several phenomena. Reflection is the process by which X-rays are returned by the material. This happens either at the boundary between a medium and vacuum or air (surface reflection) or at the interior of the medium (volume reflection). Transmission (or refraction in the case of propagation through different materials) is the passage of X-rays through a medium. Absorption is the way in which the energy of a photon is taken up by matter, typically the electrons of an atom. These phenomena highly depend on the material or medium in which the X-rays travel as well as the energy of the X-rays. Macroscopically speaking, a medium can be characterized by its refractive index (or index of refraction, optical constants):

$$n = \frac{c}{v} \qquad 1.1$$

where c and v are the phase velocities of the electromagnetic waves propagating in vacuum and in the medium respectively. The refraction of light travelling from one medium to another can be easily predicted by the Snell's law using the refractive indexes.

Unlike the visible light, X-rays possess refractive indexes which are very close to and smaller than 1, indicating a weak refraction in the materials. For distinguishing more clearly their differences, refractive index is written as:

$$n = 1 - \delta \tag{1.2}$$

The absorption of the X-rays in the materials, on the other hand, is much higher compared to the visible light. Another optical parameter is then introduced to take into account the absorption:

$$\beta = \frac{\mu\lambda}{4\pi} \tag{1.3}$$

where μ is the coefficient corresponding to the photo-absorption and λ is the wavelength of the radiation. In the end a complex refractive index which contains a real part and an imaginary part is defined as:

$$\tilde{n} = 1 - \delta + i\beta \tag{1.4}$$

For each material used in this thesis, the complex refractive index as a function of the energy/wavelength of the electromagnetic wave is taken from the CXRO X-ray Interaction With Matter database [3] unless a reference is mentioned particularly. The detailed description of the photon-matter interactions will be presented in the later chapters.

1.2 Periodic multilayer mirrors

Optical systems often need redirection of the photon beams. Thus mirrors are essentially required. Unlike the visible light for which a simple silver coating is enough to obtain a good reflection, X-rays endure much more intensity loss after being reflected by a material surface. As a consequence, specially composed optics are needed for X-rays. Periodic multilayer mirrors are critical optical components designed to reflect electromagnetic radiations which include but are not limited to X-rays.

1.2.1 Principle

A multilayer, by its name, consists a combination of thin layers of materials. Periodic multilayer mirrors have a much finer definition. The layers must be periodically arranged and deposited on a planar and preferably polished substrate (silicon, silica, etc). The materials must be well selected to be respectively absorbent and transparent to the incident radiation. In general, two materials with high and low atomic numbers Z are used. A scheme of a multilayer mirror reflecting a photon beam is presented in Figure 1.2, in which *d* is the period of the multilayer. The good selection of the materials contributes to the high performance of the mirrors as optical components to reflect radiation of certain energy/wavelength.

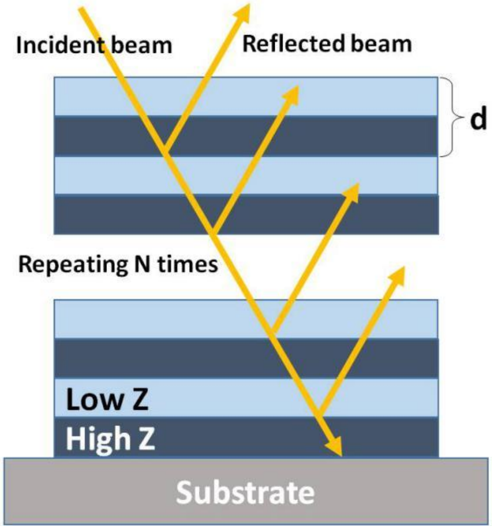

Figure 1.2: Scheme of a multilayer mirror.

The principle of a periodic multilayer mirror can be analogously compared to the diffraction (or reflection) of a monochromatic radiation by a natural crystal, a well-known phenomenon which can be described by the famous Bragg's law presented in Figure 1.3 where n_{diff} represents the diffraction order (to be distinguished from the refractive index n), λ is the wavelength of the diffracted radiation, d is the distance between two neighbor atomic planes of the crystal (or the crystalline period compared to the multilayer period with the same notation d) and θ is the angle between the incident radiation beam and the reflecting atomic plane. This formula allows us to develop techniques to analyze crystalline materials and to design X-ray optics like reflecting mirrors. A high reflectance is obtained by the constructive interference of the diffracted radiation. Yet the working wavelength of a crystalline reflecting mirror is limited by the lattice spacing of the crystal (d in the Bragg's law). A higher value of the spacing is required if we want to design a mirror that reflects X-rays that are relatively "softer" with longer wavelength. However the lattice spacing of natural crystal is too small, only several tenths of nm. It is mandatory to find an alternative way.

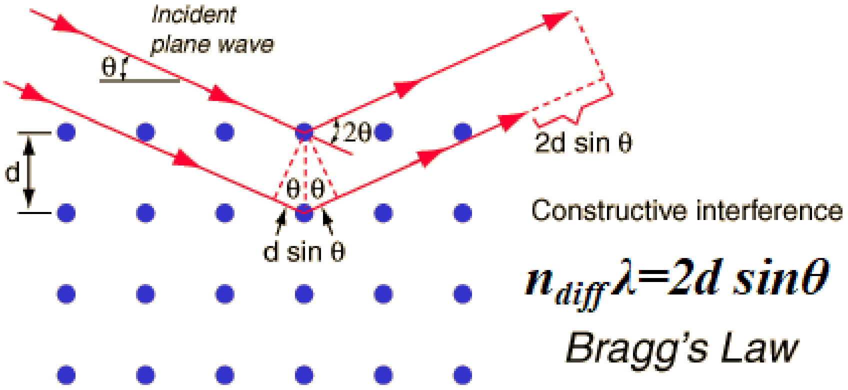

Figure 1.3: Schema of the Brag's law. Source: [hyperphysics.phy-astr.gsu.edu]

One of the best solutions so far is to make periodic multilayers for which we can design the lattice spacing as we like as long as the deposition technique allows. For the diffraction of a monochromatic radiation by a periodic multilayer, the definition of the parameter d changes in the Bragg's law. It becomes the period of the multilayer, or the thickness of each period.

As a mirror, its performance is naturally described by its reflecting ability. The performance of a periodic multilayer mirror is characterized by its reflectance which is introduced as the intensity ratio of the reflected radiation over the incident radiation. The reflectance depends on the structure of the multilayer as well as the optical properties of the selected elements of the component layers. For certain applications, a good reflectance for a sufficient energy or angular range is an important standard for the performance as well. Yet it is out of the discussion of this thesis.

Reflection and transmission at a perfect interface

Starting with a simple model as presented in Figure 1.4, where an electromagnetic plane wave propagates through a perfect interface, the reflectance as well as the transmittance can be theoretically calculated. Depending on the experimental situation, grazing angles θ and normal angles ψ, complementary for each other, are used equivalently for convenience. The relationship among the normal angles are given by the law of reflection $\psi_i = \psi_r$ and Snell's law $n_1 \sin\psi_i = n_2 \sin\psi_t$.

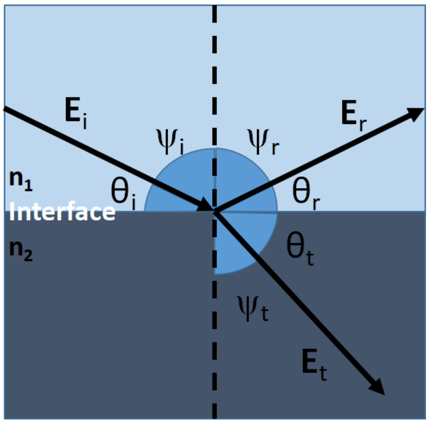

Figure 1.4: Diagram of an incident plane wave propagating through the interface between two materials with different refractive indexes.

The reflection coefficient (r) and the transmission coefficient (t) are defined by the ratio between the amplitude of the reflected and transmitted electric fields and the amplitude of the incident electric field.

$$r = \frac{|\mathbf{E}_r|}{|\mathbf{E}_i|} \qquad 1.5a$$

and

$$t = \frac{|\mathbf{E}_t|}{|\mathbf{E}_i|} \qquad 1.5b$$

The calculation of the coefficients r and t is based on the Fresnel equations as presented below considering different polarizations of the incident light:

$$r_s = \frac{\mathbf{n}_1 \cos\psi_i - \mathbf{n}_2 \cos\psi_t}{\mathbf{n}_1 \cos\psi_i + \mathbf{n}_2 \cos\psi_t} \qquad 1.6a$$

and

$$t_s = \frac{2\mathbf{n}_1 \cos\psi_i}{\mathbf{n}_1 \cos\psi_i + \mathbf{n}_2 \cos\psi_t} \qquad 1.6b$$

for s-polarization where the electric field **E** of the incident radiation is perpendicular to the incident plane;

$$r_p = \frac{\mathbf{n}_2 \cos\psi_i - \mathbf{n}_1 \cos\psi_t}{\mathbf{n}_1 \cos\psi_t + \mathbf{n}_2 \cos\psi_i} \qquad 1.7a$$

and

$$t_p = \frac{2\mathbf{n}_1 \cos\psi_i}{\mathbf{n}_1 \cos\psi_t + \mathbf{n}_2 \cos\psi_i} \qquad 1.7b$$

for p-polarization where the electric field **E** of the incident radiation is parallel to the incident plane. The formulas for magnetic materials are slightly different, but are not discussed in this thesis. The reflectance and transmittance of the radiation are expressed by these coefficients as:

$$R = |r|^2 \qquad 1.8a$$

and

$$T = \mathrm{Re}\left\{\frac{\mathbf{n}_2 \cos\psi_t}{\mathbf{n}_1 \cos\psi_i}\right\}|t|^2 \qquad 1.8b$$

The calculation of the transmittance considers only the real part for the refractive indexes. The energy conservation is satisfied by the absorption of the radiation, defined by absorbance A:

$$A = 1 - R - T \qquad 1.9$$

One must note that this equation is merely available for a perfect interface. The photons will be scattered out of the specular directions in the case of interface imperfection, which will be discussed later.

Calculation for a multilayer

In the case of a periodic multilayer mirror, the situation is much more complicated. The phenomena (reflection and transmission) described above repeatedly happen at each interface between two neighboring layers. We consider a photon beam incident with the wavelength λ on a multilayer stack of N layers where the ith layer has a thickness l_i and refractive index $\boldsymbol{n_i}$ as described in Figure 1.5.

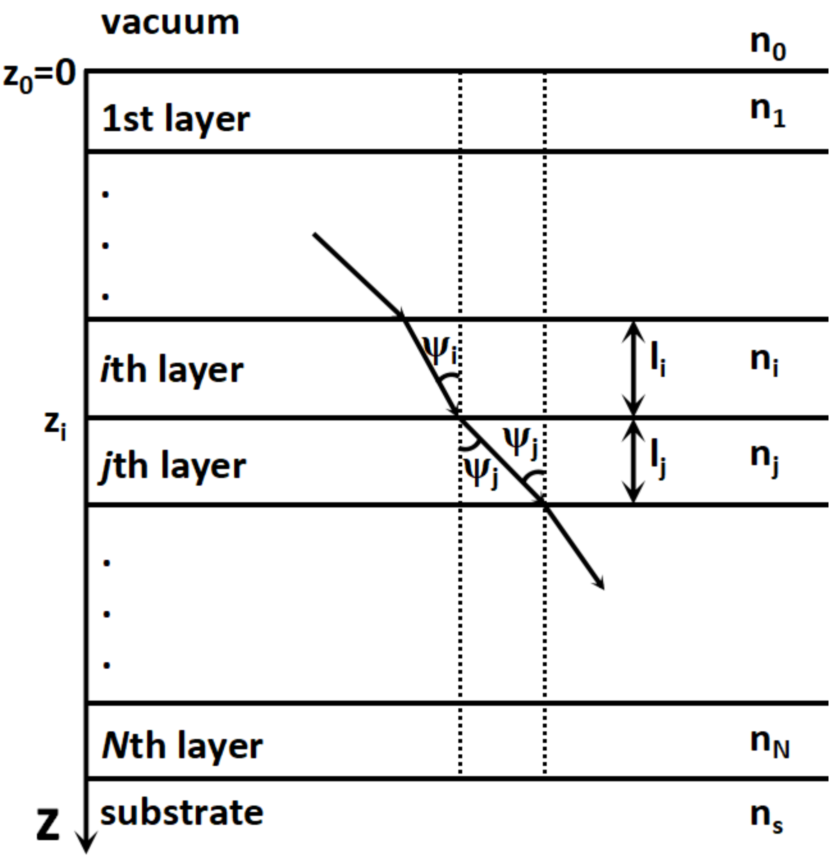

Figure 1.5: Diagram of a N-layer stack with a photon beam propagating within.

The relation among the net reflection coefficients (r_i and r_j) and transmission coefficients (t_i and t_j) of the ith and jth layers respectively are given by the following equations:

$$r_i = \frac{r_{ij} + r_j e^{2i\beta_i}}{1 + r_{ij} r_j e^{2i\beta_i}} \qquad 1.10a$$

$$t_i = \frac{t_{ij} t_j e^{2i\beta_i}}{1 + t_{ij} t_j e^{2i\beta_i}} \qquad 1.10b$$

where r_{ij} and t_{ij} are given by formulas 1.6 and 1.7 considering the polarization of the incident light, βi is defined as:

$$\beta_i = 2\pi d_i \mathbf{n}_i \sin \psi_i / \lambda \qquad 1.11$$

To calculate the net reflection, one may apply equations 1.10 recursively. Since there is no reflection from the substrate, the iteration has boarder conditions: $r_{N+1}=0$ and $t_0=1$. Finally, the reflectance of the multilayer can be obtained by applying the formula 1.8a using r_0 as the reflection coefficient.

Consideration of an imperfect interface

It is clear that the performance of a periodic multilayer mirror highly depends on its period and the refractive indexes of its component materials. There are also other critical factors which have inevitable negative effect. In the real case, it is impossible to obtain a perfectly flat interface. The imperfection is mainly due to the interface roughness and the diffusion of the materials. The specular reflectance suffers a loss when the X-ray beam is reflected by an imperfect interface.

Figure 1.6 shows different types of interfaces: rough interface, diffused interface and a perfect one as reference. Interfacial roughness and diffusion coexist at the interface between two neighbouring layers. They can be described by an interface profile function $p(z)$ and its derivative $w(z)=dp(z)/dz$. $p(z)$ is defined as the normalized average value of the dielectric function $\varepsilon(x,y)$ along the z direction:

$$p(z) = \frac{\iint \varepsilon(x,y)\,dxdy}{\Delta\varepsilon \iint dxdy} \qquad 1.12$$

where $\Delta\varepsilon$ is the difference between the dielectric coefficients of the pure materials on the two sides of the interfaces and the relation between refractive index and dielectric coefficient is:

$$\mathbf{n} = \sqrt{\varepsilon} \qquad 1.13$$

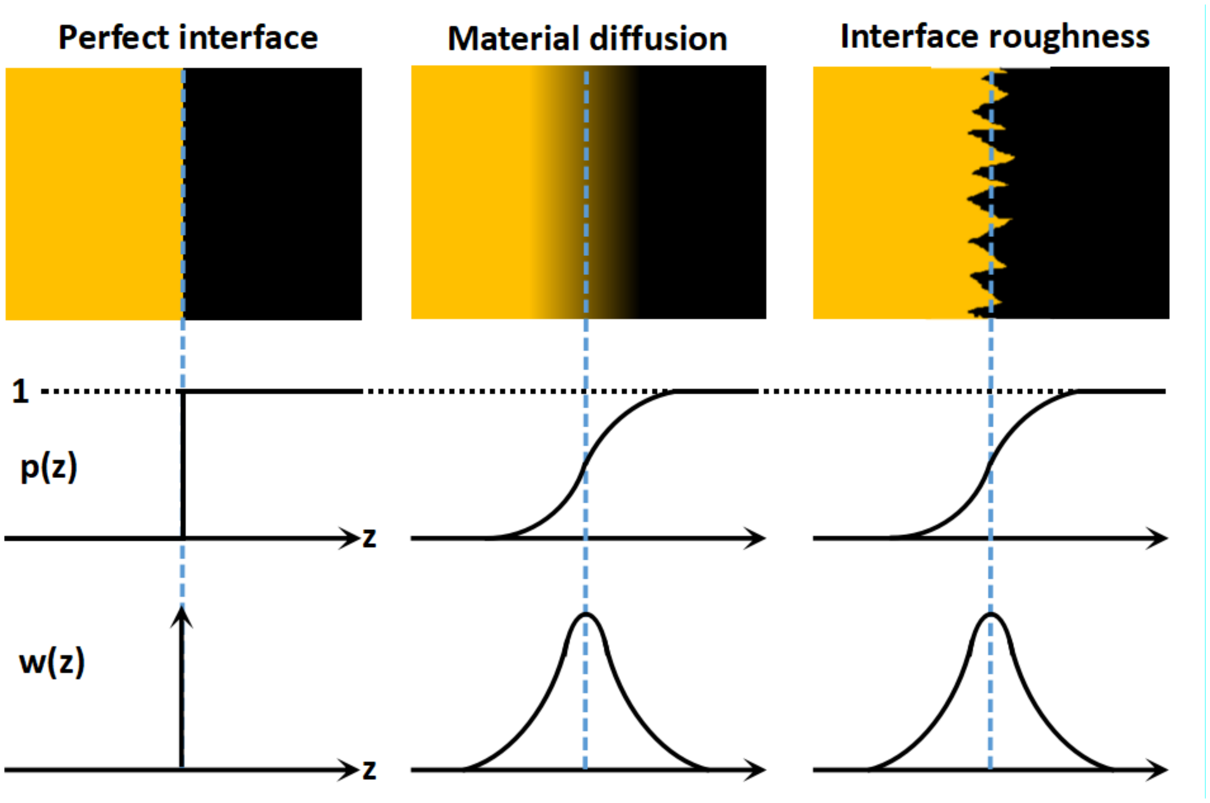

Figure 1.6: One-dimensional representation of different types of interfaces with their interface profile functions p(z), and derivatives w(z).

To introduce the consideration of the imperfect interface onto the calculation of reflectance, one needs to multiply the reflection coefficient by the Fourier transform of the derivative of the interface profile,

$$r_{ij}' = r_{ij}\tilde{w}(s_i) \qquad 1.14$$

where $s_i = 4\pi\cos\psi_i/\lambda$ and then one may proceed the iteration to calculate the reflectance using the new reflection coefficient r_{ij}'.

Matrix calculation

Other than the recursive calculation method, the reflectance and transmittance of a radiation propagating in the media of a multilayer can be equally calculated with matrix algorithm [4]. Starting with a single layer of material, the transfer matrices for radiations for s and p polarizations traveling through this layer can be defined as:

$$\mathbf{M}_s = \begin{pmatrix} \cos(lk_0\tilde{n}\cos\theta) & -\frac{i}{\cos\theta}\sin(lk_0\tilde{n}\cos\theta)\frac{1}{\tilde{n}} \\ -i\cos\theta\sin(lk_0\tilde{n}\cos\theta)\tilde{n} & \cos(lk_0\tilde{n}\cos\theta) \end{pmatrix} \qquad 1.15a$$

$$\mathbf{M}_p = \begin{pmatrix} \cos(lk_0\tilde{n}\cos\theta) & -\frac{i}{\cos\theta}\sin(lk_0\tilde{n}\cos\theta)\tilde{n} \\ -i\cos\theta\sin(lk_0\tilde{n}\cos\theta)\frac{1}{\tilde{n}} & \cos(lk_0\tilde{n}\cos\theta) \end{pmatrix} \qquad 1.15b$$

where l is the thickness of the layer, k_0 is modulus of the incident radiation wave vector, θ is the angle between the interface of the media and the radiation wave vector in the layer. For a multilayer, all layers are taken into account. When the radiation propagates through N layers, the characteristic matrix become:

$$\mathbf{M} = \mathbf{M}_1\mathbf{M}_2 \ldots \mathbf{M}_{N-1}\mathbf{M}_N = \prod_{i=1}^{N} \mathbf{M}_i(l_i, \tilde{n}_i) = \begin{pmatrix} m_{11} & m_{12} \\ m_{21} & m_{22} \end{pmatrix} \qquad 1.16$$

The transmission and reflection coefficients can then be calculated with the characteristic matrix (Equation 1.16) considering different polarization types:

$$t_s = \frac{2n_0\cos\theta_0}{(m_{11} + m_{12}\tilde{n}_{sub}\cos\theta_{sub})n_0\cos\theta_0 + m_{12} + m_{22}\tilde{n}_{sub}\cos\theta_{sub}} \qquad 1.17a$$

$$r_s = \frac{(m_{11} + m_{12}\tilde{n}_{sub}\cos\theta_{sub})n_0\cos\theta_0 - (m_{12} + m_{22}\tilde{n}_{sub}\cos\theta_{sub})}{(m_{11} + m_{12}\tilde{n}_{sub}\cos\theta_{sub})n_0\cos\theta_0 + m_{12} + m_{22}\tilde{n}_{sub}\cos\theta_{sub}} \qquad 1.17b$$

and

$$t_p = \frac{2\frac{\cos\theta_0}{n_0}}{(m_{11} + m_{12}\frac{\cos\theta_{sub}}{\tilde{n}_{sub}})\frac{\cos\theta_0}{n_0} + m_{12} + m_{22}\frac{\cos\theta_{sub}}{\tilde{n}_{sub}}} \qquad 1.18a$$

$$r_p = \frac{(m_{11} + m_{12}\frac{\cos\theta_{sub}}{\tilde{n}_{sub}})\frac{\cos\theta_0}{n_0} - (m_{12} + m_{22}\frac{\cos\theta_{sub}}{\tilde{n}_{sub}})}{(m_{11} + m_{12}\frac{\cos\theta_{sub}}{\tilde{n}_{sub}})\frac{\cos\theta_0}{n_0} + m_{12} + m_{22}\frac{\cos\theta_{sub}}{\tilde{n}_{sub}}} \qquad 1.18b$$

where n_0 is the refractive index of the incident medium (which is normally vacuum or atmosphere) and θ_0 is the grazing incident angle of the radiation. $\tilde{n}_{sub}$ and θ_{sub} correspond to the ones of the substrate.

In the case of a periodic multilayer, the formula can be simplified by calculating the matrix M of one period first. The matrix for the whole stack can be obtained by the multiplication of M [5,6]:

$$\mathbf{M}_{stack} = \mathbf{M}^K = \begin{pmatrix} m_{11} & m_{12} \\ m_{21} & m_{22} \end{pmatrix}^K = \begin{pmatrix} m_{11}U_{K-1}(a) - U_{K-2}(a) & m_{12}U_{K-1}(a) \\ m_{21}U_{K-1}(a) & m_{22}U_{K-1}(a) - U_{K-2}(a) \end{pmatrix} \quad 1.19$$

where K is the number of periods of the multilayer and U is the trigonometric Chebyshev polynomial of the second kind:

$$U_K(a) = \sin[(K+1)\arccos(a)] / \sqrt{1-a^2} \quad 1.20a$$

$$a = \frac{m_{11} + m_{22}}{2} \quad 1.20b$$

1.2.2 Deposition process

Deposition of a periodic multilayer requires reproducible coatings of alternative materials. There are a variety of methods based on physical vapor deposition (PVD) to manufacture the periodic multilayer mirrors such as magnetron sputtering [7], electron beam evaporation and ion beam sputtering. All the samples studied in this thesis are fabricated using magnetron sputtering technique. Figure 1.7 presents the instrumental setup for magnetron sputtering installed at the Institute of Precision Optical Engineering of Tongji University in China.

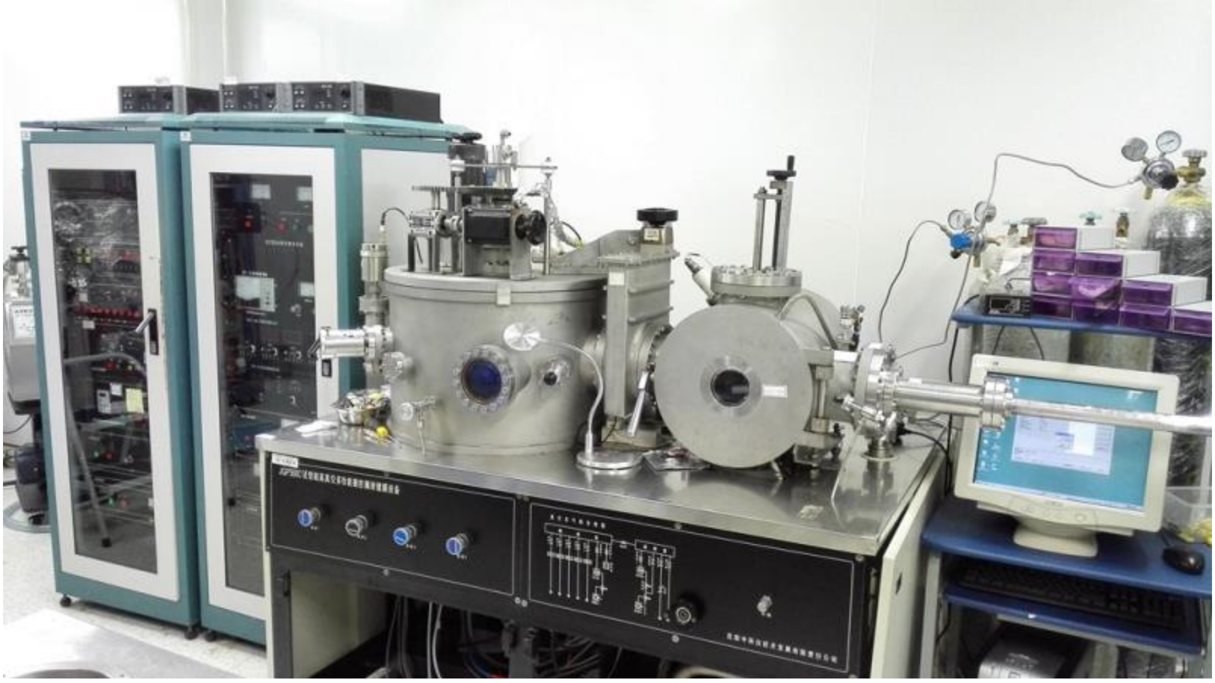

Figure 1.7: Magnetron sputtering setup of Institute of Precision Optical Engineering of Tongji University in China.

John S. Chapin is credited with inventing the first planar magnetron sputtering source with a patent filed in 1974 [8]. Magnetron sputtering differs into two types by the source which excites the material target: direct current (DC), which is applied to deposit conductive materials; radio frequency (RF), which is for not only conductors but also semiconductors and insulating materials. A diagram of the DC magnetron sputtering process is presented in Figure 1.8. The deposition system is placed in a vacuum chamber which is initially evacuated to a base pressure removing air and then back-filled with sputtering gas, which is in general Ar with the purity of 99.999%. A DC electrical current is applied to the target material located on the cathode, the substrate on which the material is deposited becomes the anode.

The electrically neutral argon gas atoms are first ionized by the electric tension between cathode and anode and a plasma is formed which consists of weakly charged gas like particles with roughly half ions and half electrons that emits the visible plasma glow. The argon ions then bombard onto the surface of the negatively charged target, passing the momentum to the surface atoms so that the atoms may have enough energy to be ejected off into the plasma. These vaporized target atoms form a thin film coating on the substrate.

Since ions are charged particles, magnetic fields can be used to control their behavior. Magnets are installed behind the cathode. The magnetic field forms a boundary area which traps electrons near the surface of the target. The electrons collide with the ejected target atoms to form negatively charged ions, which are driven by the electric field towards the substrate, improving the deposition rate.

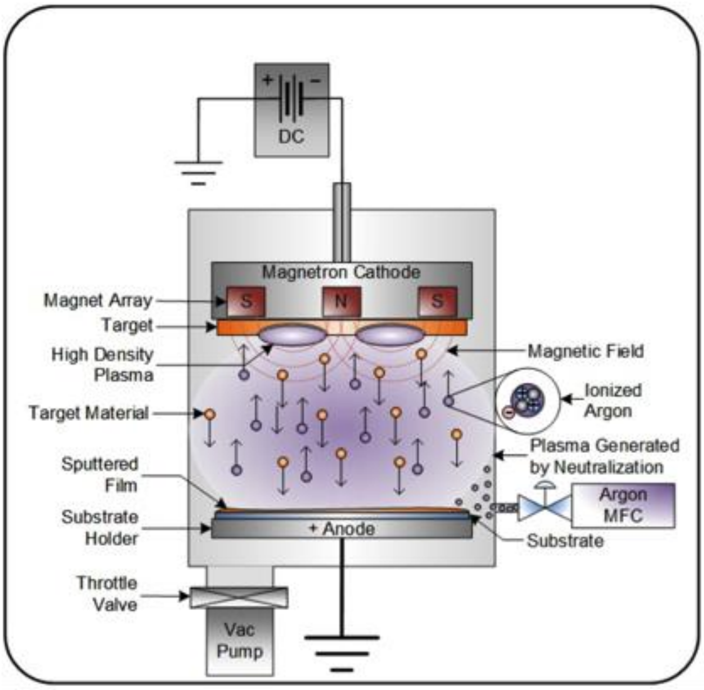

Figure 1.8: Diagram of the DC magnetron sputtering process. Source: [http://www.semicore.com/images/photos/diagram-dc-magnatron.png]

To deposit a periodic multilayer mirror onto a substrate, 2-3 targets are used depending on the materials required for the multilayer. The targets rotate under the substrate during the sputtering, alternatively depositing different materials onto the substrate. The thickness of each layer of the mirror can be controlled by the electromagnetic field as well as the deposition time.

1.2.3 Applications

The applications of a periodic multilayer mirror depend on its working energy/wavelength, for example the water window [9,10]. The water window is a very special spectral region. It extends from carbon K absorption edge (284 eV in energy or 4.4 nm in wavelength) to oxygen K edge (533 eV or 2.3 nm). Since the energy is lower than the oxygen absorption edge, water is transparent to the soft X-rays; yet carbon, which is the main component element of all organic and biological molecules, is absorbing. Radiations which possess energies in water window could be used in X-ray microscopy for imaging living specimens like organs or even cells. The microscopes, like other optical instruments, require reflecting mirrors for focusing or changing of the radiation direction. This is where the periodic multilayers come into use. In this thesis, Cr/Sc-based multilayers are designed for the water window.

Normal incident multilayer mirrors for X-rays make feasible high resolution X-ray microscopes with relatively large fields of view which are ideal for laser fusion research, biological investigations. The application also covers astronomical studies. For the past two decades, normal incidence multilayer telescopes have been installed on a number of solar physics satellite and sounding rocket instruments. A Cassegrain telescope, which consists of a large concave primary mirror and a small convex secondary mirror, is illustrated in Figure 1.9.

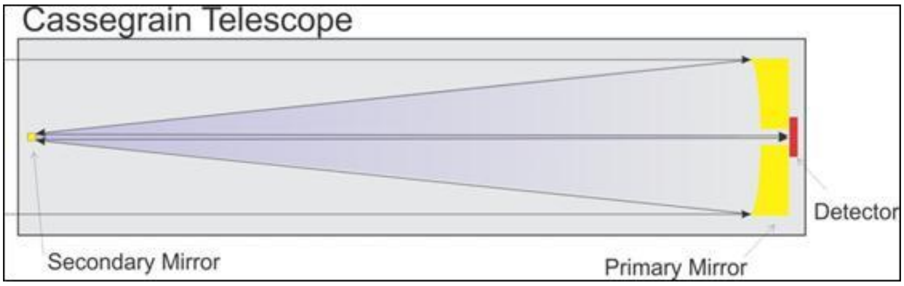

Figure 1.9: Illustration of a Cassegrain telescope. Source: [http://www.rxollc.com/technology/ni_optics.html]

Multilayer mirrors that works at glancing incident angle have been applied to the astronomical exploration. Designed by Tongji University, the first high energy X-ray astronomical telescope in China consists of several arrays of multilayer mirrors deposited on curved glass substrates as presented in Figure 1.10. The focusing is realized by multiple reflection of the received X-ray signal.

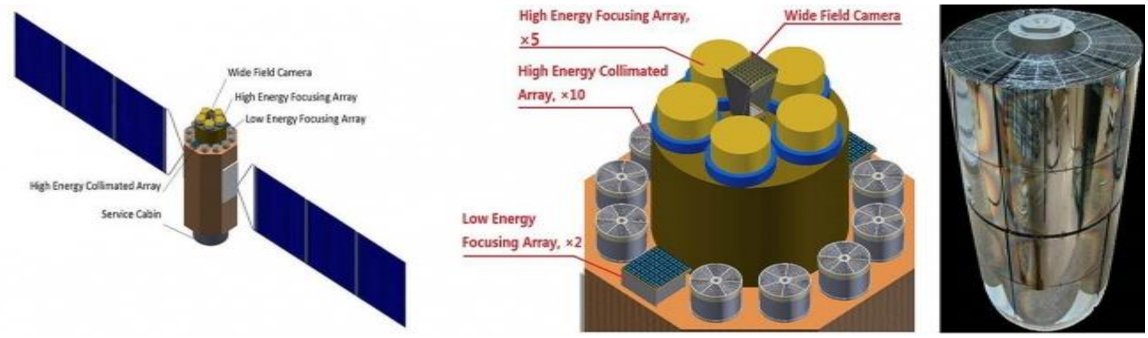

Figure 1.10: Focusing system of an astronomical telescope designed by Tongji University. Source: [https://news.tongji.edu.cn/classid-182-newsid-50661-t-show.html]

Besides, multilayer mirrors also serve as critical optical parts in scientific research institutes such as synchrotron radiation and free electron laser facilities.

Chapter 2: X-ray standing waves and their generation

In this chapter, a general introduction of the concept of X-ray standing waves is given first along with some historical milestones concerning its development. Two types of X-ray standing waves (XSW) resulting from different interferences are described: standard X-ray standing waves and Kossel diffraction. Then the sources used to generate the X-ray standing waves are exhibited which cover all the synchrotron beamlines and accelerator platform from where the experimental results presented in this thesis are obtained.

2.1 X-ray standing waves

Scientific theories and technologies concerning solid state physics and crystallography have developed rapidly ever since the discovery of Laue diffraction [11] and Bragg's law [12]. The concept of X-ray standing wave technique was first mentioned by B. W. Batterman in the 1960s [13]. It is essentially an X-ray interference technique. When two coherent X-ray beams cross each other, a periodic electric field is generated due to their interference as shown in Figure 2.1. The period of this electric field D is related to the wavelength of the X-ray beams and their directions. Such relation can be described by the following formula:

$$D = \frac{\lambda}{2\sin\theta} = \frac{2\pi}{Q} \qquad 2.1$$

where λ is the wavelength of the two X-ray beams, Q is the difference of their wave vectors (K_0 and K_R) and 2θ is the angle between them.

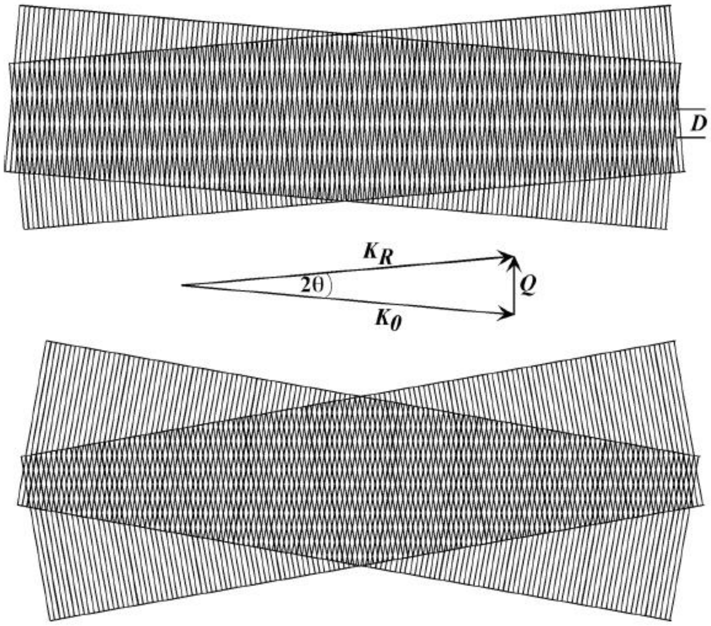

Figure 2.1: Scheme of the X-ray standing waves resulting from the interference of the two coherent X-ray beams crossing each other [14].

One may compare the X-ray standing waves with the mechanical standing waves such as the ones generated on a vibrating guitar string where we have nodes and anti-nodes. The nodes almost remain still while the anti-nodes possess an enhanced amplitude of the vibration. An X-ray standing wave field is two-dimensional. There are nodal planes where the amplitude of the electric field is suppressed and the anti-nodal planes where it is enhanced. The feature of the X-ray standing waves makes them quite suitable for the analysis of periodic layered structures where the electric field is formed under Bragg condition. By varying the parameters (wavelength, angle) of the X-ray beams, one may modulate the position of the anti-nodal planes of the electric field. By analyzing the phenomena such as X-ray emission or X-ray photoemission under the effect of X-ray standing waves, depth dependent information of the periodic structure can be obtained. Since the electric field is periodic, one may study not only the surface but also the buried interfaces of periodic materials, which in our case are the periodic multilayer mirrors.

In this thesis X-ray standing wave technique is used to study the structure of surfaces and interfaces of multilayers made of nanoscale thin films with high depth resolution and chemical selectivity. It makes the experimental acquisition specific on certain interfaces located on the anti-nodal plane.

2.1.1 Standard X-ray standing waves

A standard X-ray standing wave is generated by a X-ray beam reflected or diffracted by a periodic structure. The periodic electric field results from the interference between the incident and the reflected X-rays as schematically presented in Figure 2.2.

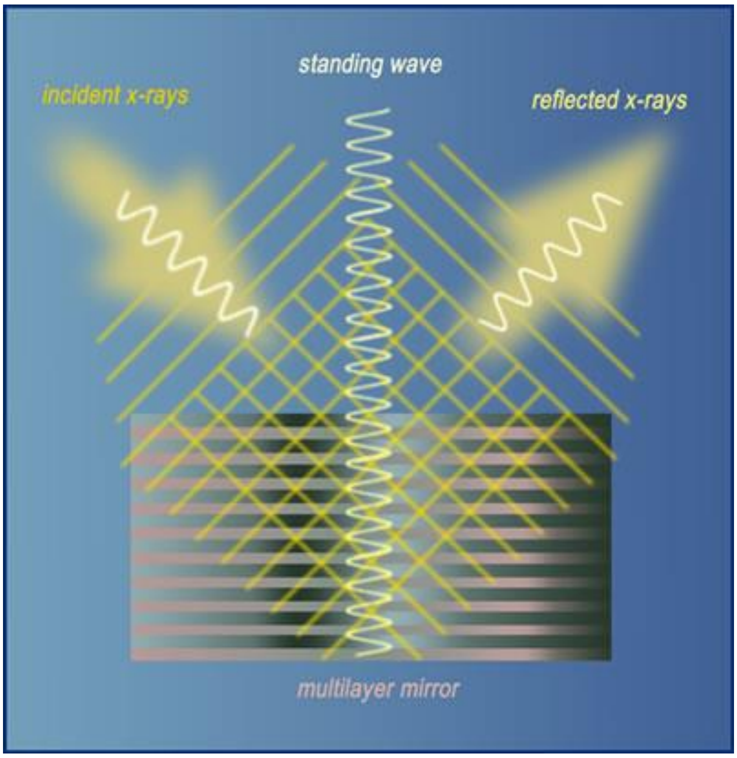

Figure 2.2: Scheme of the standard X-ray standing waves generated by a X-ray beam reflected by a multilayer mirror.

Source: [http://www2.lbl.gov/Science-Articles/Archive/sb/Oct-2004/1-ALS-What-Lies-Beneath.html]

According to the formula 2.1, if the wavelength of the incident X-ray is known and the grazing incident angle is fixed at the first order Bragg angle corresponding to the period of the periodic structure, ideally the period of the electric field will be equal to the period of the material and the anti-nodal planes will be located at each interface of two neighbor periods. Imagine that we vary the grazing incident angle of the X-rays around the first order Bragg angle, the anti-nodal planes in each period will move accordingly from one component layer to another. Taking the example of a Pd/Y multilayer mirror (with a B_4C capping layer on top) irradiated by a 10 keV synchrotron radiation beam, as presented in Figure 2.3, the periodic electric field (or the XSW field) possesses exactly the same period as the one of the multilayer itself. In this particular case, the anti-nodal planes are located at each Y-on-Pd interface when the incident angle (grazing) is placed at the first order Bragg angle. For an incident angle smaller than the Bragg angle the anti-nodal planes are located in the Y layers while the nodal planes are placed at the Pd layers. As a result, the ionization is enhanced for Y atoms while for Pd atoms it is reduced. If we move the incident angle through the Bragg angle towards a higher value, the anti-nodal planes move accordingly from Y layers to Pd layers. At a higher angle the ionization is then enhanced for Pd layers and reduced for Y layers.

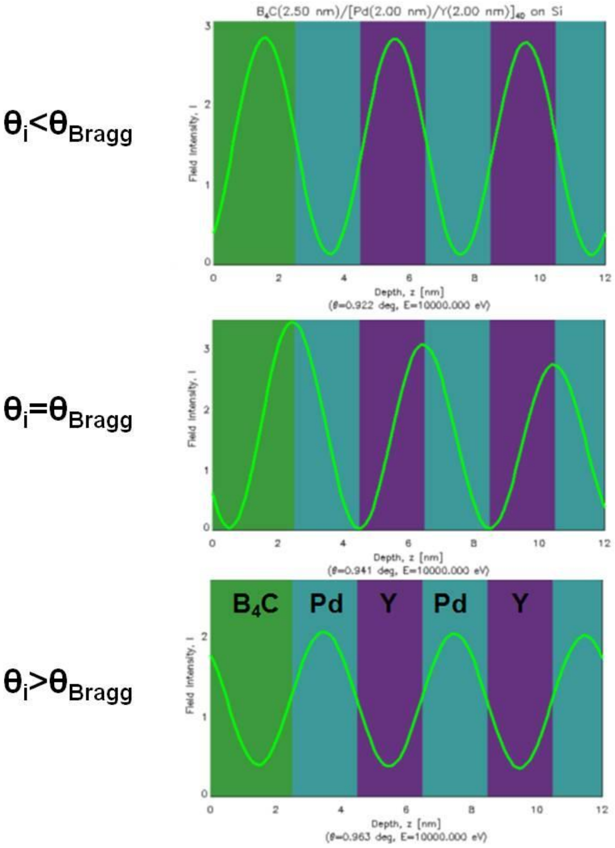

Figure 2.3: XSW field (intensity in yellow line) in a Pd/Y multilayer upon irradiation of a 10 keV photon beam.

Such variation of the ionization rate can be experimentally observed by measuring the related phenomena such as X-ray emission, photoemission and Auger emission as a function of the grazing angle of the incident X-ray. The experiment concerning the example of Pd/Y multilayer presented in Figure 2.3 will be discussed in detail in Chapter 5.

2.1.2 Kossel diffraction

Kossel diffraction is named after Walther Kossel who in 1934 experimentally demonstrated the lattice interference of X-ray spherical waves, emitted by a single-crystal copper itself, during the bombardment with a high-energy electron beam [15]. It is slightly different from the standard X-ray standing waves. Instead of the interference of the incident and the reflected X-ray, Kossel diffraction is generated by the characteristic X-ray emission following the ionization of the material. The X-ray emission is isotropic. A particular portion of the photons will propagate in directions where the Bragg's law is satisfied for a set of diffraction planes of the periodic lattice and for the energy of the emitted photons. The interference of the X-ray emission happens, as presented in Figure 2.4, in the shape of two opposite cones with an opening half-angle of $(90°-\theta_B)$ where θ_B is the Bragg angle. The central axe shared by the two cones is perpendicular to the diffraction planes. Each cone is doubled in the figure, representing the angular broadening of the diffraction.

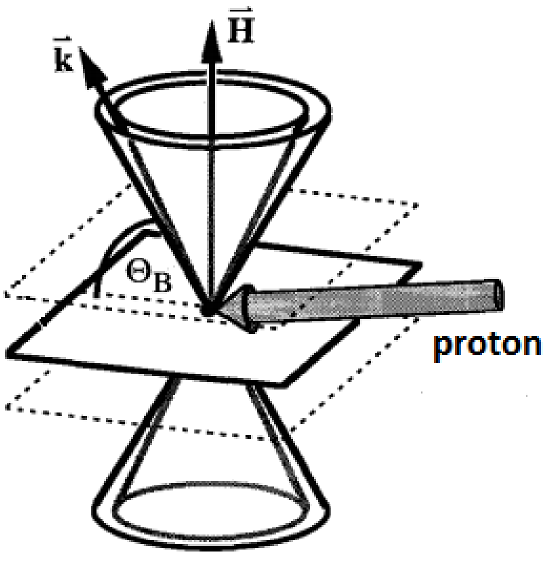

Figure 2.4: Scheme of the Kossel generated by a multilayer mirror irradiated (and ionized) by a proton beam. [16]

As the emitted photons in the directions of these two cones are both monochromatic and axially symmetric, X-ray standing waves are generated and can be exhibited by detecting the X-ray emission intensity as a function of the detection angle (the angle between the direction of the detected X-ray and the diffraction planes). From an experimental point of view, the observation of Kossel diffraction requires the detection of emitted photons, bringing a disadvantage compared to the standard XSW for which multiple detection methods can be applied. Yet Kossel diffraction possesses its unique advantages. For a start, the ionization source can be introduced from any directions and the incident angle can be fixed, bringing great instrumental convenience. In fact, with the help of a spatially resolved X-ray color camera, the whole experimental setup can be fixed. Detailed information about this setup will be introduced in Chapter 5. Although the detection signal is limited to photons, multiple options for the ionization source are available which is another advantage that broadens the use of this technique.

2.2 Generation of X-ray standing waves

In this section, the different sources that have been used, during the 3-year work of the thesis, to generate XSW are presented.

2.2.1 Synchrotron radiation

Most of the experiments described in this thesis are performed in synchrotron radiation facilities where high brilliance synchrotron light is generated. Synchrotron radiation is the electromagnetic radiation emitted when charged particles are deviated.

One may take a glimpse of the setup of a synchrotron radiation facility in Figure 2.5. There are several steps to obtain the synchrotron radiation. First, an electron beam is emitted by an electron gun. It is then accelerated by the electric field in a linear accelerator (linac) where the electrons reach a kinetic energy of a magnitude of 100 MeV. The electrons are then directed into the booster ring, a circular accelerator, where they are further accelerated up to a relativist speed close to the speed of light with an energy of several GeV. At this energy level, the electrons are injected into the storage ring where they circulate. The trajectory of the electrons in the storage ring is in fact not a perfect circle but an arrangement of alternating arcs and straight segments, which is guided by bending devices (bending magnets or undulators) where the electrons lose energy in the form of photons, the synchrotron radiation, that travel tangentially to the trajectory of the electron beam. In the line segment parts or the straight sections, the electrons are accelerated by radiofrequency cavities to compensate the energy loss due to the emission of synchrotron light so that the energy of the electrons in the storage ring maintains approximately a constant. An end station called beamline is installed tangentially to take advantage of the synchrotron light.

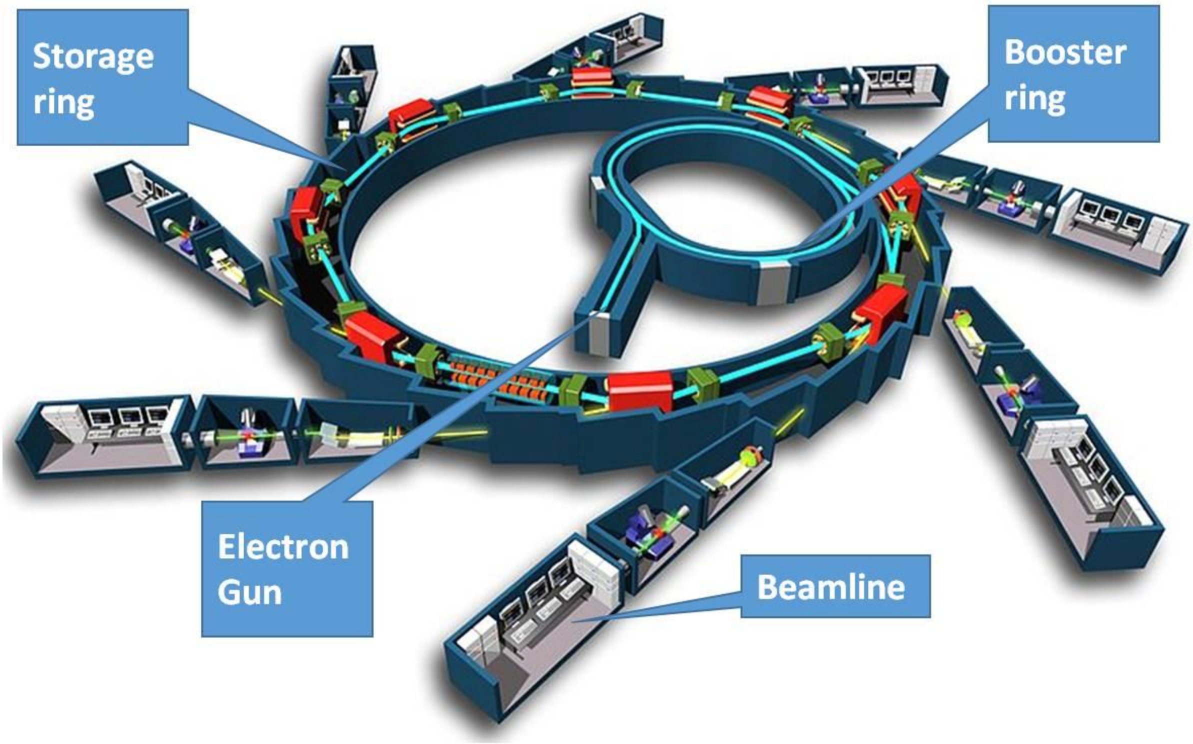

Figure 2.5: General diagram of SOLEIL synchrotron radiation facility in France. (Copyright © EPSIM 3D/JF Santarelli, Synchrotron Soleil)

Synchrotron radiation has great advantages compared to laboratory generated X-rays. Its spectral range is very broad, covering from microwaves to hard X-rays. One may select the photon energy required for the experiments. The light is not only highly brilliant but also highly monochromaticand emitted with a low divergence thanks to the monochromators and slits of the beamlines.

In this thesis, the synchrotron radiation is used to perform X-ray reflectivity measurements and to generate standard X-ray standing waves. Note that in the literature it is also possible to generate Kossel diffraction with synchrotron radiations [17]. Such method is not presented here with the purpose of avoiding repeating the work of others.

BEAR beamline of Elettra synchrotron radiation facility

The BEAR (Bending magnet for Emission, Absorption and Reflectivity) beamline is installed at the right exit of the 8.1 bending magnet at Elettra synchrotron facility in Trieste, Italy [18,19]. It provides synchrotron radiation of a wide spectral range from 2.8 to 1600 eV with the spot size on the sample down to 30 μm x 100 μm (vertical x horizontal). The monochromator parameters of BEAR beamline are presented in Table 2.1 where the resolving power, which represents the spectral resolution, is defined as:

$$R = \frac{\lambda}{\Delta\lambda} \qquad 2.2a$$

or equivalently

$$R = \frac{E}{\Delta E} \qquad 2.2b$$

Table 2.1: Monochromator parameters of BEAR beamline.

Grating	Energy range	Resolving power	Typical flux
G1200	40-1600 eV	3000 @ 400 eV	10^{11} photons/s at 100 eV
G1800	200-1600 eV	5000 @ 400 eV	10^{10} photons/s at 600 eV
GNIM	2.7-50 eV	2000 @ 20 eV	10^{10} photons/s at 20 eV

BEAR beamline is equipped with multiple spectroscopic instruments including (and not limited to) specular and diffused light scattering, X-ray fluorescence and photoemission. The XRR in soft X-ray range as well as X-ray standing wave enhanced XRF measurements presented in this thesis are performed at BEAR beamline.

GALAXIES beamline of SOLEIL synchrotron radiation facility

The GALAXIES beamline [20,21] is installed at the third-generation synchrotron SOLEIL (short name of “Source Optimisée de Lumière d’Energie Intermédiaire du LURE”) in Saint-Aubin, France. The beamline is dedicated to inelastic x-ray scattering (IXS) and hard X-ray photoemission. It is designed to provide a monochromatic and micro-focused beam using an in-vacuum U20 undulator with the highest flux possible in the 2.3-12 keV spectral range and an adaptable energy bandwidth between 50 meV and 2 eV. The spot size of the synchrotron beam is down to 20 (V) x 80 (H) μm^2 with the flux in the magnitude of 10^{11} to 10^{12} photons/s. HAXPES measurements described in this thesis are performed at GALAXIES beamline.

2.2.2 Proton beam

As discussed previously, the X-ray standing wave resulting from Kossel diffraction can be generated by different ionization sources [22]. Compared to other sources such as electrons [23-26] and photons [27-31], a proton beam [32-38] has its great and unique advantages, of which the major ones are briefly listed below.

1. Low scattering
2. Low Bremsstrahlung
3. Low energy loss

We start by discussing and comparing the properties of an electron beam and a proton beam in the case of the analysis of thin multilayer stacks of the order of 1 µm or less. A finely focused electron beam spreads rapidly as it enters the material as presented by Monte Carlo simulation in Figure 2.6 in the case of silicon. The scattering is three dimensional in reality (in the shape of a bubble). From an experimental point of view, the size of the electron scattering (about 4 µm) may not be much of an influence compared to the practical electron beam size. However the spreading trajectory of the electrons increases the ionization rate, making the situation much more complicated.

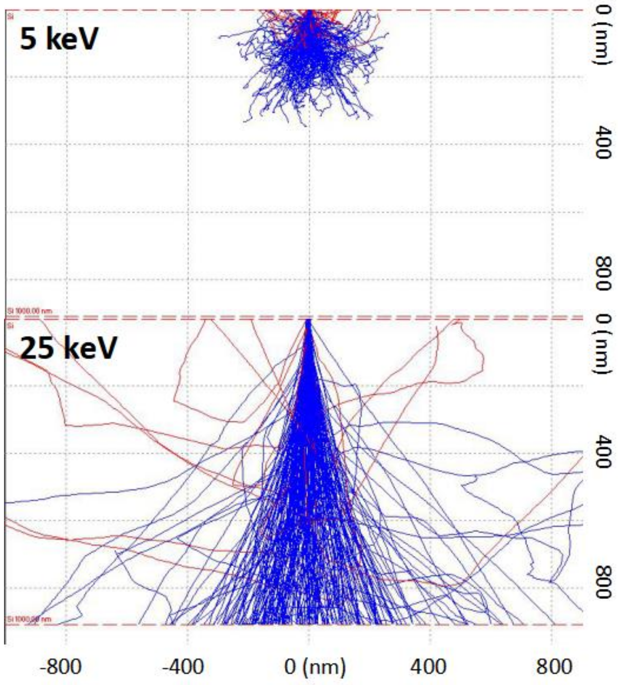

Figure 2.6: Monte Carlo simulation of electron trajectories of 5 kV and 25 kV scattering in silicon [39].

The energy loss of the electrons along with their complex trajectory result in a non uniform ionization rate along the depth of the material, as presented in Figure 2.7.

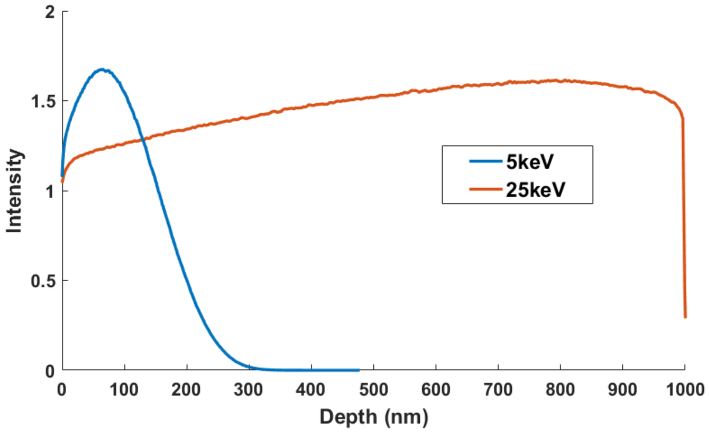

Figure 2.7: Depth distribution of the ionizations (Si K level) by electron of 5 keV and 25 keV scattering in silicon.

The proton beam, on the other hand, travels in a straight line apart from a small amount of end-of-range broadening. Figure 2.8 presents the calculation of the trajectory of 10000 protons with an energy of 2 MeV scattered in Si using the SRIM program [40]. There is barely any obvious divergence of the beam before 200 nm (which is approximately the total thickness of our samples). Besides, using proton instead of electron may reduce the Bremsstrahlung, resulting in a much “cleaner” background of the measured X-ray spectra. A third advantage of proton beam is mainly over X-rays, which attenuate exponentially in the multilayer. The exposure as the protons penetrate the material is relatively constant. According to the simulation, there will be merely 0.5% energy loss of a 2 MeV proton after penetrating through a 200 nm multilayer. Such nearly ignorable energy loss of the beam, along with its low scattering property, indicates a quasi-uniform ionization rate through the multilayer.

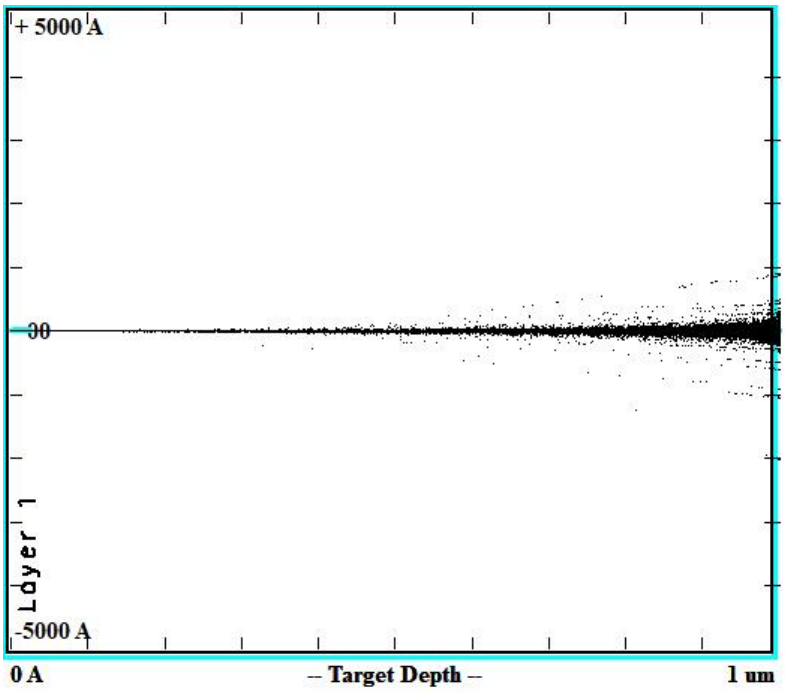

Figure 2.8: Calculation of 10000 protons scattering in resist on a silicon substrate (Copyright Ian Vickridge, Sorbonne University).

Another reason why we select proton beam as the ionization source for our experiment is simply because no one has ever applied Kossel diffraction onto multilayer characterization using proton beam before, meaning that we will be exploring a completely new characterization method.

SAFIR platform

The proton beam we work with is provided by the SAFIR (Système d'Analyse par Faisceaux d'Ions Rapides) platform of Sorbonne University in Paris, France. This research platform is based on a type AN-2000 electrostatic Van de Graaff particle accelerator associated with beamlines and experimental chambers.

The principle of the accelerator is to impart kinetic energy to charged particles, which are produced within an RF-type ion source. The different ionizable gases (H, He, ...), which are stored in the upper part of the accelerator, are introduced selectively via controllable thermomechanical valves. They are ionized by a radiofrequency field of the order of 100 MHz and then magnetically focused in the axis of the extraction channel. The presence of magnets increases the free path of free electrons, which increases the number of ionizations. The extraction electrode has a potential of a few thousand volts, which allows it to repel and expel the ions to the accelerator column. At the top of this column, the terminal is raised to a positive high voltage which creates a uniform potential gradient to accelerate the ions into a mono-charged and mono-kinetic beam. The beam is then deflected by an electromagnet to be directed towards the experimental chambers.

The accelerator is capable of generating ion beam of H^+, D^+, He^+, C^+, N^+, O^+ with a small divergence of 0.5 mrad and an energy up to 2.5 MeV. Spot size of the beam can be adjusted down to 1 mm^2. Available analyzing methods equipped at SAFIR include Rutherford backscattering spectrometry (RBS), particle induced X-ray emission (PIXE), nuclear reaction analysis (NRA), elastic recoil detection analysis (ERDA) and particle channelization in single crystals.

Chapter 3: Principles of the experimental methods

In this chapter, the main experimental methods for the characterization of periodic multilayer mirrors are presented with their basic principles.

3.1 X-ray reflectometry

X-ray reflectometry (XRR), also known as X-ray reflectivity, is a non-contact and non-destructive technique for structure determination of nanoscale thin films. Its principle is based on the X-ray specular reflection. A simplified setup of a X-ray reflectometer is presented in Figure 3.1, where a monochromatic X-ray beam is reflected by the sample (for example a periodic multilayer mirror as studied in this thesis). The radiation source can be an X-ray beam generated by a laboratory equipped X-ray tube or synchrotron radiation. The reflected intensity is recorded by a photon detector while varying the incident angle θ. Specular condition must be maintained during the measurement, meaning that incident angle should be equal to the reflection angle at all time. Since the radiation source is fixed in most cases, the sample and the detector are rotated with the angular values separately recorded by the goniometer. When the sample is rotated by an angle θ the detector is rotated twice as much 2θ. This acquisition mode is called θ-2θ scan.

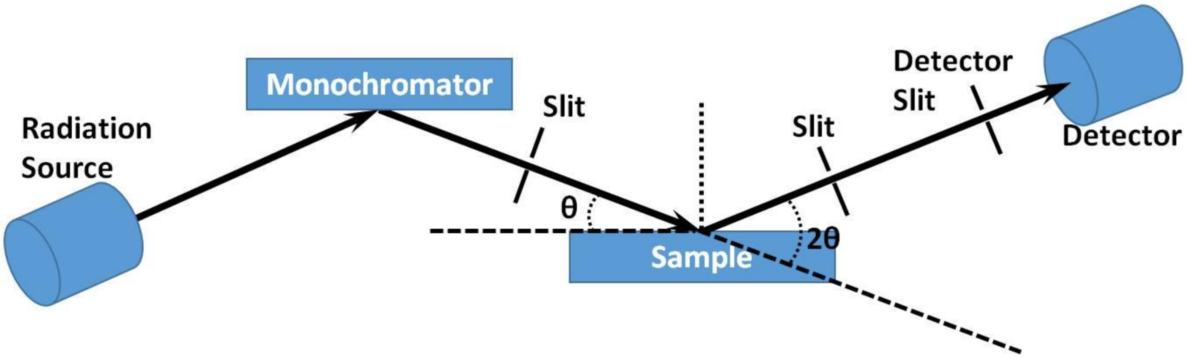

Figure 3.1: Diagram of a XRR setup.

As defined by Formula 3.1, the reflectivity is obtained as a function of the incident angle by normalizing the reflected intensity (I_r) by the incident intensity (I_0) of the X-ray beam.

$$\text{Reflectivity}\ (\theta) = \frac{\mathrm{I_r}}{\mathrm{I_0}} \qquad 3.1$$

The experimental XRR data can be analyzed by fitting to the measured XRR curve a simulated XRR curve based on a preset structural model of the sample [41]. The principle of the theoretical calculation is previously discussed in the Section 1.2.1. An example of the XRR curve fitting is presented in Figure 3.2, where an 8048 eV laboratory X-ray beam is used to measure the XRR curve of a Cr/Sc based multilayer mirror. For X-ray the refractive index is less than 1 (the refractive index of vacuum). At glancing angle (0-0.3° in the figure) the incident photon beam undergoes total external reflection as it bounces off the exterior of the material. As the angle increases, an intensity peak appears at about 2.6°. This is the first order Bragg peak satisfying the Bragg's law considering the X-ray wavelength and the multilayer period. It is then followed by the 2nd and 3rd order Bragg peaks at even higher angles. Outside the zones of total reflection and the Bragg peaks, the reflectance yields low value due to the absence of constructive interference of the reflected light.

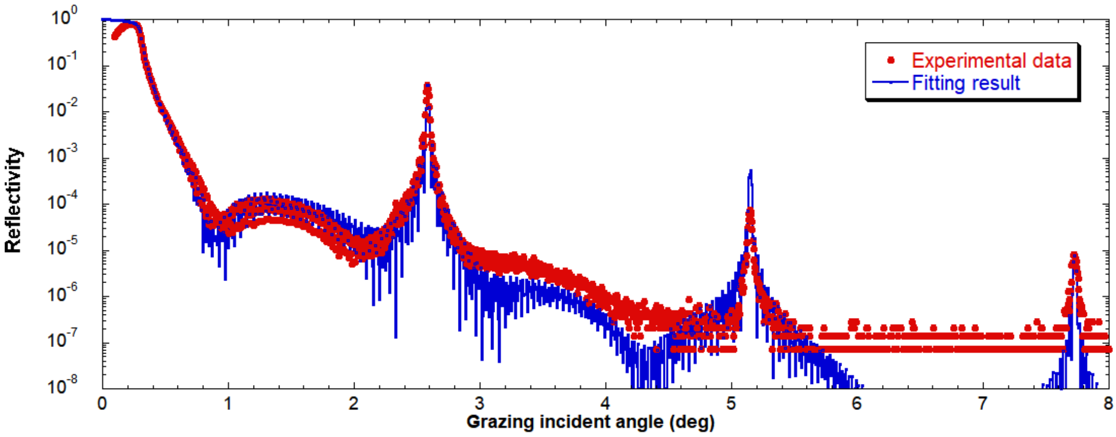

Figure 3.2: Experimental XRR curve (red) and fitting curve (blue) of a Cr/Sc based multilayer mirror.

XRR is not only a method to characterize the structure of a multilayer mirror but also a direct indication of the performance of a mirror when using an incident photon beam of an energy equal to the working energy (the energy of the application the mirror is designed for). Corresponding study is presented in Section 4.3.1 for a series of Cr/Sc based multilayer mirrors.

3.2 X-ray emission spectroscopy

X-ray emission spectroscopy (XES) concerns the detection and analysis of energy spectra of emitted X-ray photons of material following ionizations. It is a widely used non-destructive technique for material characterization and quantification. The principle of XES, presented in Figure 3.3 based on the quantification of electron energy levels of an atom, is the emission of an X-ray photon due to the de-excitation of an ionized atom. It contains two steps: first, the incident ionization source ejects an electron of an inner shell, creating a core hole; then an outer shell electron undergoes a transition following the quantum mechanical rules to replace the inner shell vacancy. A photon is emitted at the same time, possessing the energy of the transition and satisfying the energy conservation. Auger electron ejection may happen in the place of X-ray emission, but is not discussed in this thesis.

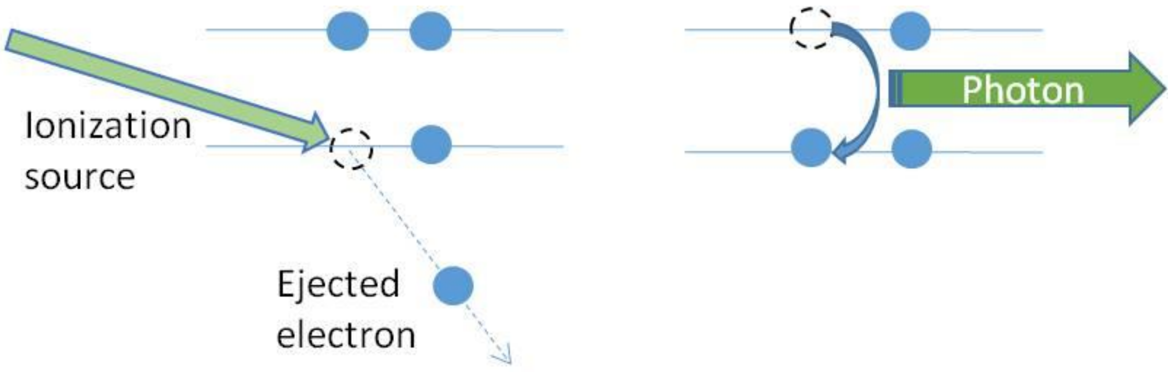

Figure 3.3: Principle of XES.

An energy dispersive detector can be used to record the XES spectrum, which is presented in Figure 3.4 (left), being the intensity of the measured X-ray photons as a function of their energy. The energy of an emission depends on the atomic constituents of the analyzed material and the type of the transition, which is shown in Figure 3.4 (right). These energies corresponding to the XES peaks reflect the electronic structure of the atoms. It is important to mention that the inevitable continuous baseline ranging across the whole XES spectrum (from zero to the energy of the incident ionization energy) is due to Bremsstrahlung, as discussed with the synchrotron radiation (Section 2.2.1), resulting from the deceleration of the ejected electrons.

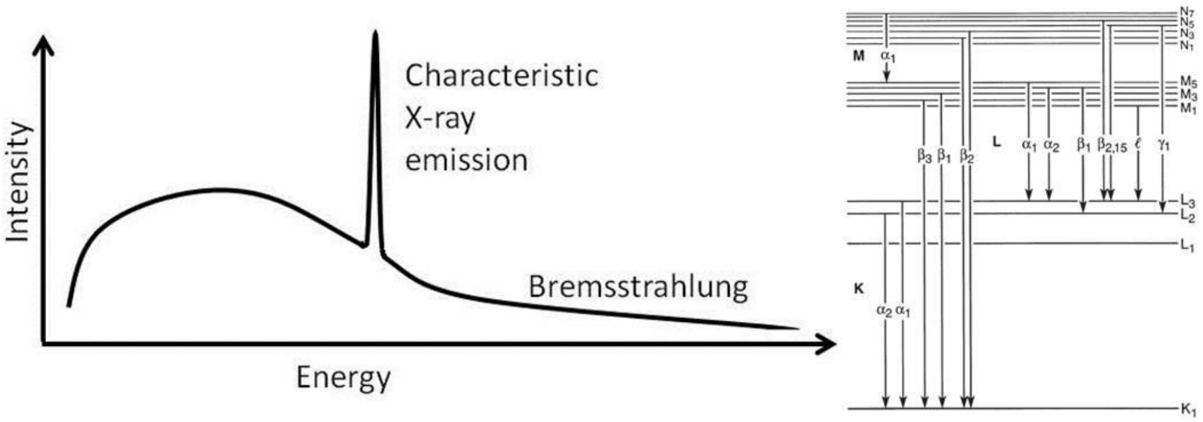

Figure 3.4: Typical XES spectrum (left) and types of X-ray emissions and corresponding transitions (right) [42].

XES is a powerful experimental tool for the determination of detailed electronic properties of the materials. Yet in this thesis, its main functionality fades in order to highlight the X-ray standing wave technique. In fact in later experimental chapters one may find that the position of the characterization XES peak is often considered known by comparing with values form the X-ray databases, as the materials that exist in the multilayer mirrors are known. We focus mainly on the intensity variation of the XES peak while modulating the XSW field within the multilayers for the purpose of their structural determination.

XES can be further divided, by distinguishing the ionization sources, into several sub-techniques of which two applied on XSW will be introduced: X-ray fluorescence (XRF) and particle induced X-ray emission (PIXE).

By definition, fluorescence is the emission of light by a substance that has absorbed light or other electromagnetic radiation. The ionization source used in our research projects is the synchrotron radiation (Section 2.2.1). One may modulate the XSW field within the multilayer by simply varying the incident angle of the photon beam, as described in Section 2.1.1. The characteristic X-ray emission peak on the spectra can be easily located by consulting the X-ray database as the elements that appear within the multilayer is known [42]. The ionization distribution (due to XSW) within the multilayer highly depends on the structure of the stack, making it possible to study the multilayer by analyzing the behavior of the characteristic X-ray emission intensity. The details will be discussed in Chapter 4 where the XRF-XSW study of a Cr/B_4C/Sc multilayer is presented.

Particle induced X-ray emission, an elemental technique first proposed by Sven Johansson in 1970, differs from XRF by using charged particles such as protons as ionization source. We select protons for their unique advantages as listed in Section 2.2.2. Just like XRF serves as the standard XSW precursor, the PIXE technique submits itself to serve for the detection of Kossel diffraction. While performing a PIXE measurement, proton backscattering spectrum can also be collected simultaneously, giving additional information. The details will be discussed in later chapters.

3.3 Hard X-ray photoelectron spectroscopy

X-ray photoelectron spectroscopy (XPS), also known as ESCA (electron spectroscopy for chemical analysis), is a powerful research tool for the study of the photoemission of an ionized substance. To describe its principle, one may again refer to Figure 3.3 which is the scheme of XES. XPS concerns but the first step in the figure: ionization. The incident ionization source, being a monochromatic X-ray beam, ejects a core level electron of the atom. The conservation of energy during this process can be described by the following equation:

$$h\nu = E_k + E_b + \phi \qquad 3.2$$

where hν is the energy of the incident photons, E_k is the kinetic energy of the ejected electron, E_b is the binding energy of the electron depending on the quantification of the atom as well as its chemical bond, ϕ is the so-call work function which represents the energy required for the electron to escape from the Fermi level to the vacuum. By measuring the kinetic energy of the emitted electrons, the binding energy of the core level from which the electrons are ejected can be obtained by applying Equation 3.2. The work function ϕ can be determined by spectral energy calibration with the spectrum of an element (such as Au and Pt) for which the binding energy E_b of certain core level is well known. Figure 3.5 shows the photoelectron spectrum of a Pd/Y multilayer with B_4C capping layer irradiated by a 10 keV synchrotron radiation where the photoemission peaks of different core levels of Pd and Y are presented.

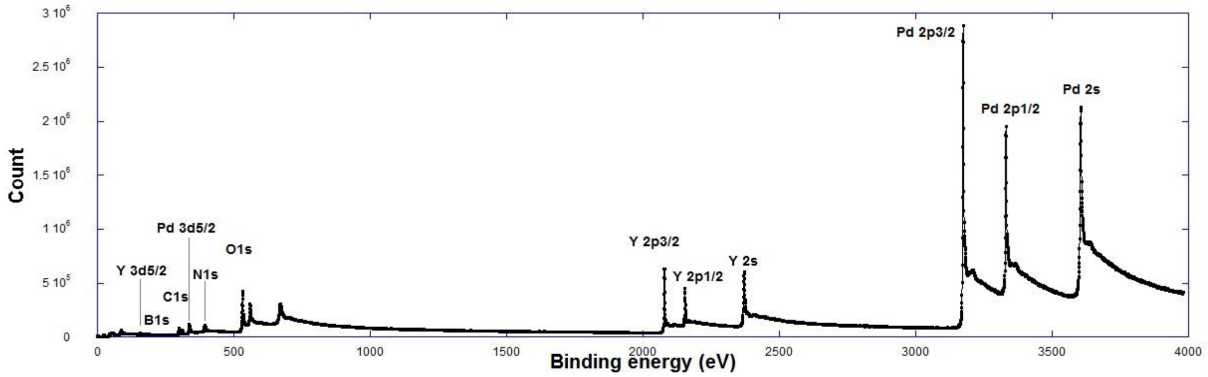

Figure 3.5: Photoelectron spectrum of a Pd/Y multilayer with B_4C capping layer irradiated by a 10 keV synchrotron radiation.

The probed depth of an XPS measurement depends on the inelastic mean free path (IMFP), which is a concept of how far an electron can travel through a material before losing its energy mainly due to its interaction with matter. Ignoring the electron diffraction, the IMFP p_E can be expressed by the following equation:

$$I(p) = I_0 e^{-p/p_E} \qquad 3.3$$

where I_0 is the original intensity of electrons emitted from the atoms and $I(p)$ is the intensity when the electrons travel through a distance of p in the material. The IMFP depends on the medium material as well as the energy of the electrons. It can be measured [43] or calculated with various theoretical models [44-47] of which the Monte Carlo calculation is well known and widely used.

XPS provides chemical state information of the measured substance. The local bonding environment varies for a species as it is affected by its chemical state (for example oxidation state) which results in a shift in energy of the photoemission peak, referred as the “chemical shift”, from its nominal position on the XPS spectrum. In general, the XPS study concerns the understanding of the chemical shifts of core level peaks. However in this thesis, we highlight the peak intensity variation due to the XSW modulation.

Hard X-ray photoelectron spectroscopy (HAXPES) [48,49] is an extension of conventional XPS technique. Although the soft X-ray range is widely used in the XPS experiments for its high-resolution and high efficiency, the low energy of soft X-ray leads to a short inelastic mean free path (IMFP) of the photoelectrons which limits the probed depth. HAXPES, on the other hand, provides a much higher value for the probed depth thanks to the long inelastic mean free path of the emitted electrons due to their high kinetic energy. Thus HAXPES is suitable to analyse a considerable part of structure buried under the surface. The disadvantage, being the low efficiency due to the low ionization cross section, can be counterbalanced by using high brilliance synchrotron radiation light source.

The details of HAPXES experiment will be discussed in Chapter 5.

Chapter 4: Study of Cr/Sc based periodic multilayers

4.1 Introduction

The Cr/Sc multilayer system discussed in this section is designed for the development of a high reflective mirror working in the water window range (2.3 – 4.4nm) [50]. Based on the Cr/Sc bilayer, derivative systems were also fabricated. Firstly B_4C barrier layer was inserted to increase the thermal stability and decrease the interdiffusion between Cr and Sc layers [51]. It has been reported that this kind of third material placed on interfaces of the original multilayer structure exhibits increased reflectivity in multiple systems such as Mo/Si [52,53], Sc/Si [54,55], Si/Gd [56] and Co/Mg [57]. Such material was inserted at either Cr-on-Sc or Sc-on-Cr interfaces and should lead to different optical performances following the model of Larruquert [58]. Secondly, a CrN/Sc sample was also fabricated by adding nitrogen into the sputtering gas (argon) during deposition; this would decrease the interdiffusion and sharpen the interfaces [59], and thus a higher reflectivity is expected.

XRR study will be presented first. The optical performances of all studied multilayer mirrors at their application energy will be compared. We present the fitting of the soft XRR data to explore the structure (layer thickness and interface roughness) of the multilayers.

The second method is standing wave enhanced X-ray fluorescence (XRF-XSW). When the reflected beam is generated at the Bragg condition for a super-lattice like the periodic Cr/Sc multilayer, the period of the XSW equals the periodicity of the reflecting planes. By scanning the fluorescence yield around the Bragg angle, the position of the elements on either side of the interface can be revealed.

Kossel diffraction study is presented in the end of this chapter. This technique requires a periodic structure to diffract the emitted radiation, thus it has been applied to study crystals and interferential multilayers. However, to the best of our knowledge, Kossel lines have never been observed in multilayers upon particle excitation. Our work shows that it is possible to study multilayers having a nanoscale period upon proton irradiation through the observation of Kossel lines.

4.2 Experimental methods

Samples were prepared by using magnetron sputtering with no substrate bias. The purity of Cr, Sc and B_4C targets was better than 99.9%. The substrates were sliced and polished Si (100) wafers. Pure Ar gas was used for Cr, Sc and B_4C layers whereas a mixture of Ar and N_2 gas (80% Ar, 20% N_2) was used for CrNx deposition. The Cr and CrNx layers were deposited by DC magnetron sputtering with a 50 mA current. Sc and B_4C layers were deposited by RF magnetron sputtering with a power of 50 and 150 W respectively. The thickness of each layer was determined by the velocity of the substrate over the deposition area. The original design was 100 periods of Cr/Sc bilayer covered by a 3 nm-thick B_4C capping layer in order to protect the sample from oxidization. Hard XRR measurements were performed using a commercial grazing incident reflectometer (BRUKER Discover D8) equipped with Cu K radiation source (8048 eV). Table 4.1 presents for each sample the detailed structural parameters as designed and extracted from the fitting of the measured XRR curve. The notation of sample structure starts at bottom of stack. The measured period values are different from the expected values for the deposition. For example, samples 2 and 3 were both expected to have 2.2 nm for each period, yet the determined values are 1.72 nm, about 20% less. Such a change of the period (contraction) is due to the intermixing of different layers which will be described later. Sample 5 (Cr/Sc) and 6 (CrN/Sc) have almost the same period compare to the expected value. This indicates that the intermixing is very likely due to the B_4C layer.

Table 4.1: Designed structural parameters of the samples and period deduced from the fitting of the measured hard XRR curves.

Sample	**Structure**	**Period (nm)**	**Cr (nm)**	**Sc (nm)**	**B_4C (nm)**	**Measured period (nm)**
1	$[B_4C/Cr/Sc]_{100}$ + B_4C cap	1.9	0.6	1.0	0.3	1.65
2	$[Cr/B_4C/Sc]_{100}$ + B_4C cap	2.2	0.6	1.0	0.6	1.72
3	$[B_4C/Cr/Sc]_{100}$ + B_4C cap	2.2	0.6	1.0	0.6	1.72
4	$[B_4C/Cr/Sc]_{100}$ + B_4C cap	2.5	0.6	1.0	0.9	1.83
5	$[Cr/Sc]_{100}$ + B_4C cap	1.6	0.6	1.0	/	1.58
6	$[CrN/Sc]_{100}$ + B_4C cap	1.6	0.6(CrN)	1.0	/	1.66

Soft X-ray characterization was done using XRR and XRF-XSW. Experiments were performed on the BEAR beamline at the ELETTRA synchrotron radiation center. The choice of the incident photon energy for XRR measurements was made in accordance with X-ray absorption spectroscopy (XAS) data measured in the total electron yield mode. The retained values are corresponding to the maximum of the first XAS peaks associated to the Sc L3 and Cr L3 absorption edges. For XSW measurements we chose the energy associated to Cr L3 edge. The angle between the incident beam and the fluorescence detector, a silicon drift detector (SDD), was fixed at 60°. The fluorescence light was measured selecting the energy window around the Cr L emission (572.8 eV). Being that the energy resolution of the detector is about 100 eV, in this way we excluded the contribution coming from Sc L emission (395.4 eV). The intensity of Cr L emission was scanned as a function of the grazing incident angle, leading to the so-called XSW curve.

The sample selected for the PIXE experiment is the Cr/B_4C/Sc periodic multilayer (sample 2 in Table 4.1). Working with this Cr/B_4C/Sc multilayer enabled us to measure well-resolved Sc and Cr K lines and to detect them at reasonable grazing angles. Protons of 2.0 MeV produced by the Van de Graaff accelerator of the SAFIR Platform of the Sorbonne University were used to excite the sample. With such energy, the protons ionize the Sc and Cr atoms in their K shell uniformly over the full multilayer thickness. The size of the beam on the sample was approximately 2 mm and the beam current maintained between 100 and 150 nA for the duration of the experiments. Possible evolution of the multilayer composition was monitored simultaneously via the elastically backscattered protons detected in a passivated implanted planar silicon (PIPS) detector, placed at 165° with respect to the direction of the proton beam.

The setup for the Kossel experiment is shown in Figure 4.1. The angle between the incident proton beam and the X-ray detector (SDD, silicon drift detector) was fixed at 90°. In addition to the beryllium window protecting the detector from the atmosphere, a 60 µm thick Mylar film was placed in front of the detector to block the scattered protons. Overall transmission for the Sc K and Cr K lines is greater than 0.65 and practically zero for the Sc and Cr L lines, and also for the B and C K lines. We rotated the sample so that the angle θ between the sample surface plane and the direction of the SDD, was varied around the Bragg angle, which is around 4° for the Cr Kα emission and 5° for the Sc Kα emission (see below).

The distance between the sample and the detector was 115 mm and a slit of ≈0.2 mm width was placed in front of the collimator of the SDD, giving an angular resolution of about 0.1°.

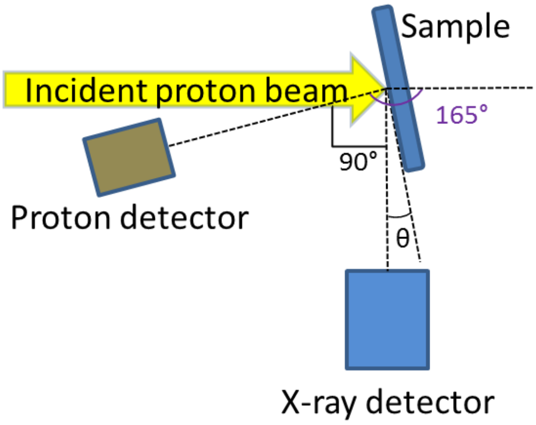

Figure 4.1: Experimental setup for the Kossel experiment. The sample is rotated so that the detection angle θ is around the first order Bragg angle calculated by considering the emission wavelength and multilayer period. The X-ray and proton detectors are fixed.

4.3 Results and discussions

4.3.1 X-ray reflectometry

The XRR curves measured at the application photon energy of 395 eV are presented in Figure 4.2. Note that a better reflectivity can be achieved by multiple means such as increasing the number of periods. In this paper we only focus on the influence of the variation of barrier layer or sputtering gas to the reflectivity. Fig. 4.2(a) displays the comparison of all samples. As expected from the values in Table 4.1, the smallest value of the period gives rise to the highest Bragg angle. In addition the peak reflectivity and bandwidth differs from one sample to another. An obvious difference in reflectivity can be observed in Fig. 4.2(b) between sample 2 (namely Cr/B_4C/Sc) and sample 3 (B_4C/Cr/Sc) which only differ by the order of the layers. For sample 2, B_4C barrier layers are located at Sc-on-Cr interfaces while for sample 3, they are located at Cr-on-Sc interfaces. The higher reflectance of sample 2 is in line with the prediction of the theoretical model of Larruquert [60] which considers the contrast of refractive index of the materials for a given deposition order in a single period. Such difference may also have other origin such as the difference in interdiffusion between B_4C-on-Cr and B_4C-on-Sc interfaces. Another group of comparisons is formed with samples 1, 3 and 4 (Fig. 4.2(c)) where the only changing parameter is the thickness of B_4C layer varying from 0.3 to 0.9 nm. The Bragg peak is (as expected) shifted according to the period change while the reflectivity remains almost constant. We may also put into this group of comparison the sample 5 (Cr/Sc) as the one with no B_4C barrier layer at all. It is clear that the barrier layer here has negative effect on the reflectivity of the mirror. The last comparison (Fig. 4.2(d)) concerns the two bilayer systems: sample 5 (Cr/Sc) and sample 6 (CrN/Sc). The introduction of nitrogen results in a doubled reflectance, which is probably due to sharpened interfaces. Furthermore, the shift of the Bragg angle peak position indicates an increase of the period upon nitridation (in agreement with Table 4.1).

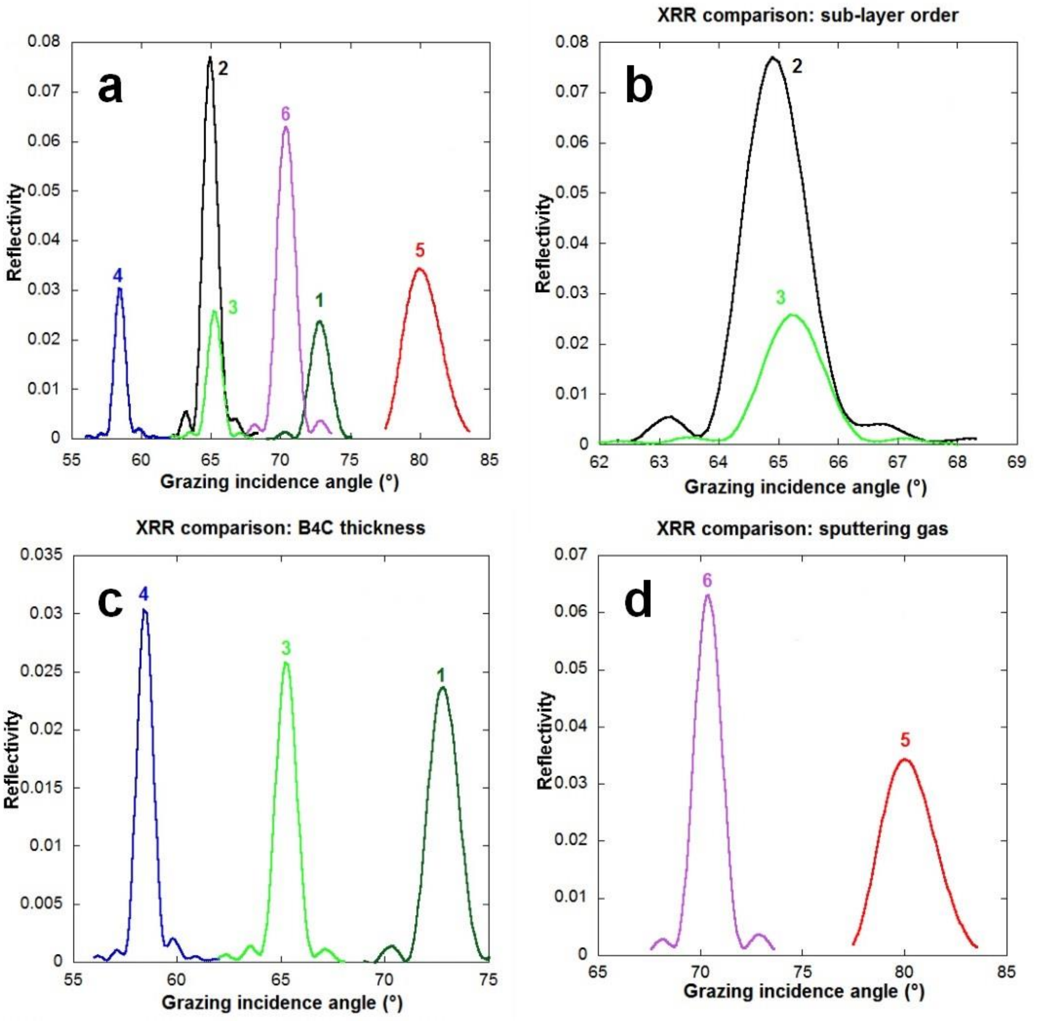

Figure 4.2: XRR curves measured at 395 eV, numbers in the figures represent samples in Table 4.1: (a) Overview for Cr/Sc based samples; (b) Comparison of the influence of layer order, samples 2 and 3; (c) Comparison of the influence of B_4C barrier layer thickness, samples 1, 3 and 4; and (d) Comparison of the influence of nitrogen in sputtering gas, samples 5 and 6.

Following the discussion of the optical performances of all samples, we illustrate the method of how XRR and XRF data are used to get a reliable description of the stack by taking sample 2 (Cr/B_4C/Sc tri-layer) as an example. According to the literature [61], the B_4C layer is totally consumed by Cr: the barrier layer is actually a mixture which consists of 70% of Cr and 30% of B_4C. We note the mixed layer as CrB_4C. The refractive index of the CrB_4C used in the fitting process (carried out with IMD software [41]) is adjusted accordingly using the tabulated values of Cr and B_4C from CXRO database [3]. We consider a three-layer model: the [Cr/CrB_4C/Sc] structure repeated 100 times over Si substrate. A layer of B_4C is put on top of such multilayer as capping layer.

We calculate the reflectivity while varying the parameters: thickness of each layer and roughness/interdiffusion of each interface. Fig. 4.3(a) and 4.3(b) show the XRR spectra of sample 2 measured at an incident photon energy of 395 eV (energy of end-use application) and of 574.8 eV (energy of maximum absorption) respectively, compared to the simulations. Between these two fittings, a variation of 1.4% for thickness and roughness of each layer is used. We believe such variation is tolerable as the experimental conditions may change slightly between the two individual experiments. For example the two XRR measurements were performed at different grazing incident angle range. This will cause a difference in the area of the illuminated area. Finally we obtained the structure for sample 2: Cr/CrB_4C/Sc presented in Table 4.2, where the fitting results of XRR measurements performed with different incident photon energies are compatible. Such result shows a non-proportional deviation of the thicknesses for the different layers compared to the designed (expected) values as well as grave intermixing extent. The severe intermixing also explains the large discrepancy between the measured, as-fabricated period thickness and their design values.

Table 4.2: Structural parameters, thickness (d) and roughness/interdiffusion (δ), of the sample Cr/CrB_4C/Sc extracted from the fitting of the measured XRR curves with different incident photon energies. The designed values of this sample is presented in the last line of the table.

Photon energy (eV)	**Period (nm)**	**d Cr (nm)**	**d CrB_4C (nm)**	**d Sc (nm)**	**δ Cr (nm)**	**δ CrB_4C (nm)**	**δ Sc (nm)**
8048	1.72	0.60	0.20	0.92	0.66	0.58	0.18
395.0	1.74	0.61	0.20	0.93	0.69	0.59	0.19
574.8	1.71	0.59	0.20	0.92	0.64	0.57	0.17

/	2.20	0.60	0.60	1.00	/	/	/

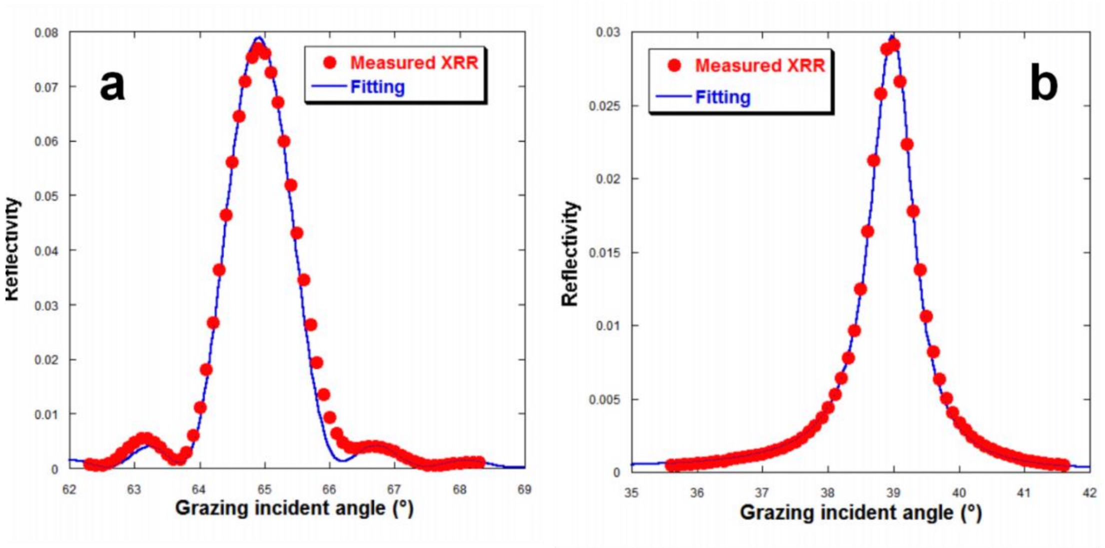

Figure 4.3: XRR of sample 2 Cr/CrB$_4$C/Sc multilayer mirror at 395 eV(a) and 574.8 eV (b). Red dots: experiment; blue line: fit.

4.3.2 X-ray fluorescence spectroscopy

We use XRF-XSW to verify the structure we obtained from XRR fitting. The experimental result obtained from XRF-XSW is compared to the simulation generated with the code FLUORT [27]. In the fluorescence calculation all parameters (thicknesses of the layers and roughness of each interface) determined from XRR fitting are applied. As shown in Figure 4.4(a), for sample 2 (Cr/CrB$_4$C/Sc) the experimental XSW curve (red dots) is in agreement with the simulated curve (blue line) in terms of position, shape and amplitude of the intensity modulation. While FLUORT reproduces the overall features present in the experimental data, better agreement is possible if additional physics —diffuse scattering and the Kossel effect [15]— are included in the models. The Kossel effect results from the diffraction of fluorescence radiation emitted from the periodic structure of the multilayer. This is illustrated in Figure 4.4(b) in the case of sample 3 (namely B$_4$C/Cr/Sc) on the 40 — 95° angular range. On the large-scale XSW curve, a first feature is located at 60° while a second structure is present around 80°. Such phenomenon happens to each sample with a varying intensity (the scattered intensity for sample 2 is low enough to be negligible). These features can be explained geometrically, taking into account that the angle between the incident X-ray beam and the SDD detector is fixed at 60°, as presented in Figure 4.5. The 60°

grazing incident angle corresponds to the specular condition (see Figure 4.5(a)) and the large tails on both sides of the peak is due to diffuse scattering. The scattered photons of the incident beam contribute to the background since the energy of the fluorescence photon (572.8 eV) is close to the one of the incident photon (575.2 eV) and cannot be resolved by the SDD detector. The secondary peak around 80° is due to the Kossel effect (see Figure 4.4(b)), which results in a wide and smooth peak given the large solid angle of the detector in our experimental configuration. To take into account these two contributions (diffuse scattering and Kossel diffraction), two Gaussian curves have been added to the original simulation of the XSW curve roughly centered at 60 and 80° respectively. Using this approach, we obtain better agreement in the angular region where the standing wave feature is present (Figure 4.4(c)).

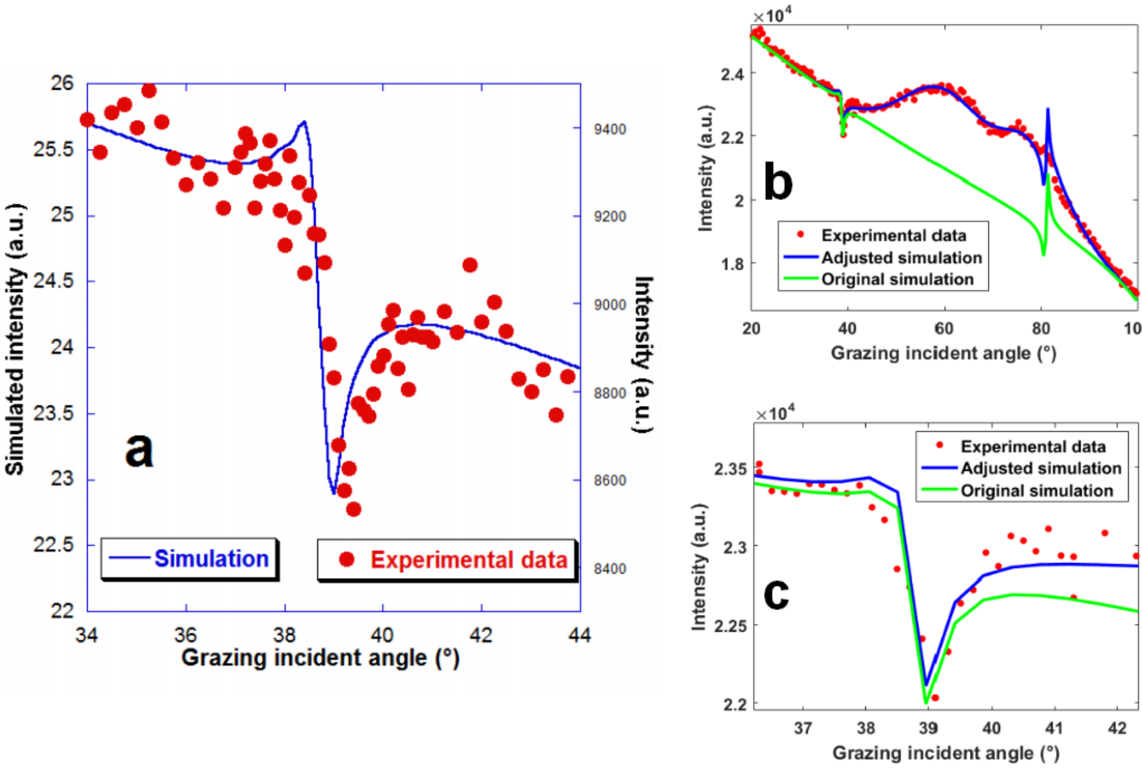

Figure 4.4: (a) XSW curve of the intensity of the Cr Lα emission of sample 2 Cr/B_4C/Sc multilayer mirror with an incident photon energy at 574.8 eV. (b) Large-scale angular scan of XSW curve at 575.2 eV of sample 3 B_4C/Cr/Sc multilayer; red dots : experimental data; green line: raw simulation; blue line : simulation taking into account the diffuse scattering and Kossel effect. (c) Comparison of experimental curve and adjusted simulations for sample 3 in the zone of interest.

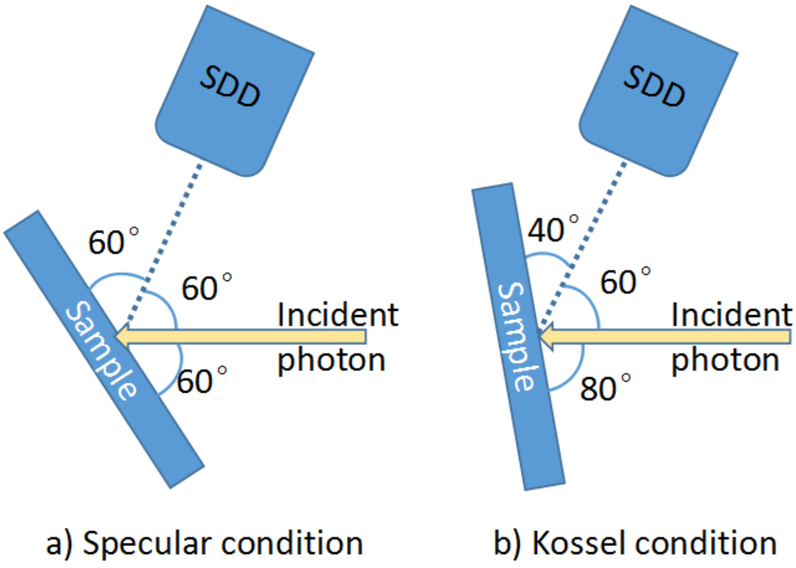

Figure 4.5: XRF-XSW experimental geometry: there is a fixed angle of 60° between the directions of the incident and the detection of the emitted photons. The XSW curve is obtained by rotating the sample. (a) when the glancing angle of the photon beam on the sample surface is equal to 60°, the detector is in the specular direction; (b) when the glancing angle of the photons is around 80°, the Kossel condition is fulfilled because the detection angle corresponds to the value of the Bragg angle of the emitted radiation.

4.3.3 Particle induced X-ray emission

We present in Figure 4.6 the 2.0 MeV proton elastic backscattering spectrum obtained from the Cr/B_4C/Sc multilayer for a total proton dose of 600 µC. Protons scattered from the Cr and Sc atoms appear in the peak near 1800 keV. The area of this peak was monitored, and did not change during the measurements, indicating no measurable loss of matter induced by the beam. As a further precaution, during PIXE measurements, the proton beam was moved on the sample surface, from one pristine zone to another, so that the dose did not exceed 600 µC at a given location.

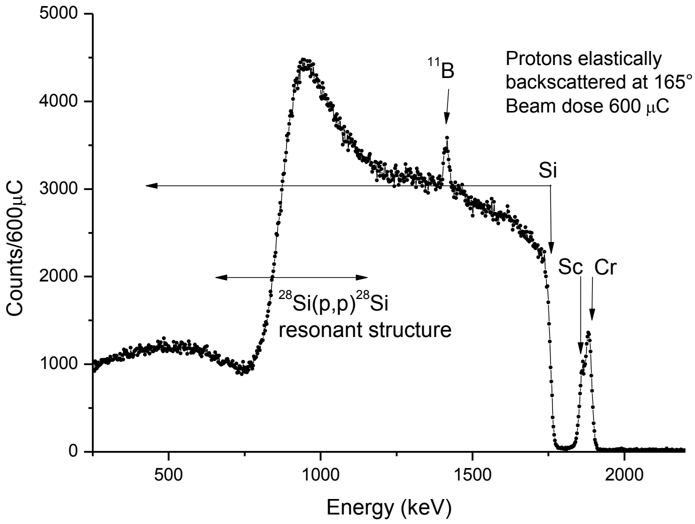

Figure 4.6: 2.0 MeV proton elastic backscattering spectrum obtained from the Cr/B_4C/Sc multilayer. The surface energies of the various elements are indicated by the downward arrows. The scattering cross sections on the light elements are highly non-Rutherford: in particular the ^{11}B(p,p). ^{11}B cross section is much greater than the Rutherford cross-section which explains why the ^{11}B peak is visible in spite of the very small quantity of boron, and the highly non-Rutherford ^{28}Si(p,p). ^{28}Si cross-section is manifested in the resonant structure obtained from the thick silicon substrate.

We show in Figure 4.7 the proton induced X-ray emission spectrum of the multilayer obtained with a proton dose of 270 μC. The Kα and Kβ lines of both scandium and chromium are well resolved. Their energies are respectively, 4090 and 4460 eV (0.303 nm and 0.278 nm respectively) for scandium and 5414 eV and 5947 eV (0.230 nm and 0.208 nm respectively) for chromium [62]. Moreover, since the proton-induced Bremsstrahlung background is very small, in the following we only consider the intensity under each peak and do not perform any fitting of the spectra or background subtraction. The Kossel experiment consists of observing these intensities as a function of the detection angle θ and plotting them to obtain what we call Kossel curves.

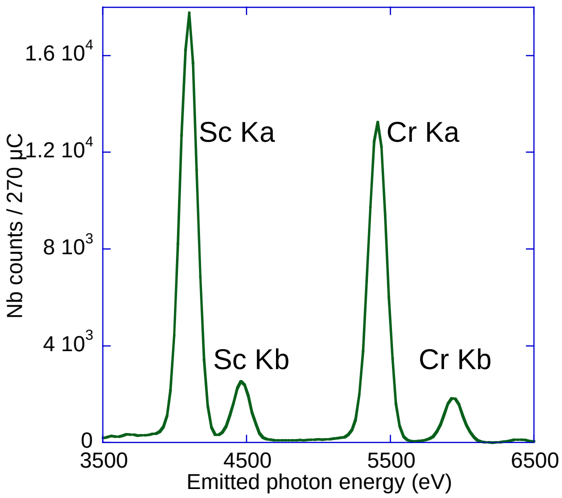

Figure 4.7: X-ray emission spectrum of the Cr/B4C/Sc multilayer induced by 2 MeV protons.

We show in Figure 4.8 the Kossel curves for the Sc and Cr Kα emissions toward the low angles and starting from zero. At each angle, the proton dose is 30 µC. The angular step is 0.2° except in the region of the strongly varying intensity where it is 0.05°. For both curves, the intensity increases first sharply and then smoothly. The intensity increase is due to the total internal reflection of the radiation emitted within the sample. The angular shift observed in Figure 4, between the onset of the Sc and Cr curves, about 0.15°, comes from the difference of the mean optical indices of the multilayer at the energies of Sc Kα and Cr Kα radiations. The sharp edge inflection point is the angle of the total internal reflection and is chosen to calibrate the angular scale. This last angle is calculated (with a typical uncertainty of ±0.01°), by optical simulation of the reflectance at the two corresponding energies, as 0.56° for Sc and 0.42° for Cr. The uncertainty on the absolute value of the experimental angles is estimated to be 0.05° (the angular step around the inflexion point) while the relative uncertainty is lower than this value.

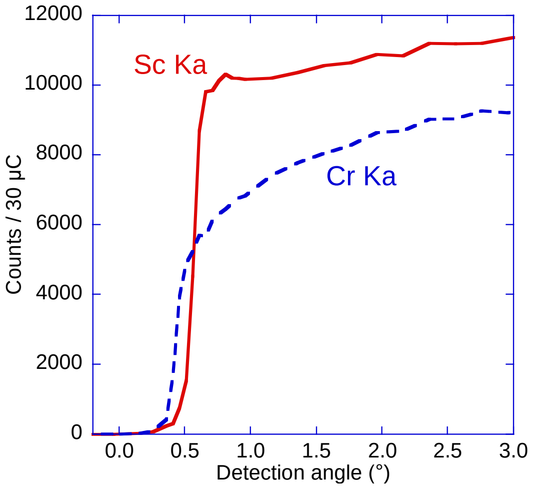

Figure 4.8: Wide scan of the Kossel curves for the Sc K (solid curve) and Cr K (dashed curve) emissions.

Figure 4.9 shows the Kossel curves obtained in the range of the Kossel feature with a 0.05° angular step and using the angular calibration determined above. At each angular position, the total dose was 120 µC for the Sc Kα curve, and 150 µC for the Cr Kα curve. The error bars represent one standard error. Experimental curves are compared to simulations [63] that calculate the electric field generated within the periodic stack by the emitted radiation according to the reciprocity theorem. The parameters of the multilayer (thickness, roughness) introduced in the simulation are those deduced from XRR analyses. The simulations are convolved with an experimental function (a rectangle) having a 0.1° width representing the angular resolution of the experimental setup. Let us note that in the case of proton excitation, simulations are easier to perform than those in the cases of electron and X-ray excitations, where the depth-dependent ionization probability should be considered; electrons loose significant energy within the thickness of the stack while X-rays are either attenuated or even create standing waves within the periodic structure.

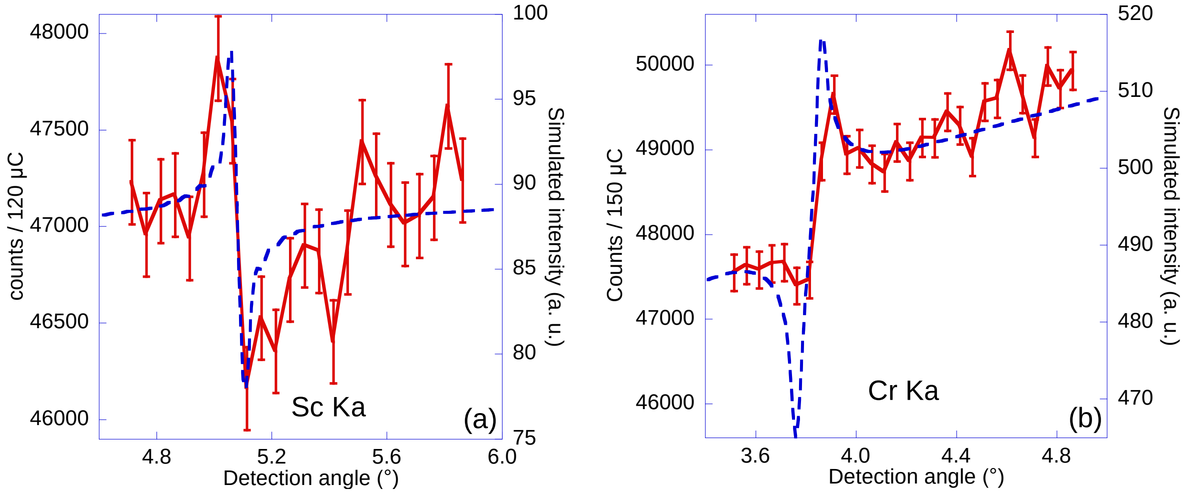

Figure 4.9: Kossel curves for the Sc Kα (a) and Cr Kα (b) emissions displayed in a narrow angular range around the Bragg angle calculated at the first diffraction order with the wavelength of the corresponding radiation and the period of the multilayer: experiments (solid curves); simulations (dashed curves).

The experimental Kossel features, Figure 4.9, lack a little contrast, i.e. the difference of intensity between the maximum and the minimum is small, owing to the relatively large angular resolution and to the limited counting statistics. This last point comes from the required angular aperture of the detection system, which leads to a very small solid angle of collection of the X-rays. It is observed, in agreement with the simulations, that the intensity fluctuations in the case of the Sc Kα curve, passing first by a maximum then by a minimum, separated by about 0.1° (see Figure 4.9(a)), are reverse with respect to Cr Kα curve, (see Figure 4.9(b)). The inflexion points of the Kossel curve discontinuities, at 5.10° and 3.85° for the Sc and Cr respectively, are consistent (within their ±0.05° uncertainty) with the angular values of 5.086° and 3.840° calculated with Bragg's law corrected from refraction, using the Sc and Cr emission wavelengths and multilayer period. This can be seen from the position of the Kossel features, well in agreement with the simulations.

The intensity modulation observed in the Kossel curve when scanning the detection angle comes from the variation of the location of the electric field inside the stack since changing the angle moves the system of standing waves perpendicular to the layers of the stack. To illustrate this point we consider the Sc Kossel curve and the depth distribution of the electric field, which, around the Bragg angle, has nearly the same period as the multilayer. When the detection angle is equal to the Bragg angle, i.e. corresponding approximately to the inflexion point of the sharp intensity decrease, Figure 4.9(a), the maxima of the electric field are located at the interfaces between the Sc and B4C layers. Shifting the detection angle by -

0.035° moves the maxima of the electric field to the centre of the Sc layers, as shown as an example in Figure 4.10. Shifting the detection angle by +0.015° and +0.03° with respect to the Bragg angle moves the maxima of the electric field at the interfaces between the B_4C and Cr layers, and at the centre of the Cr layers, respectively (not shown here). This provides a mean to selectively excite different locations of a multilayer, either inside its layers or at its interfaces.

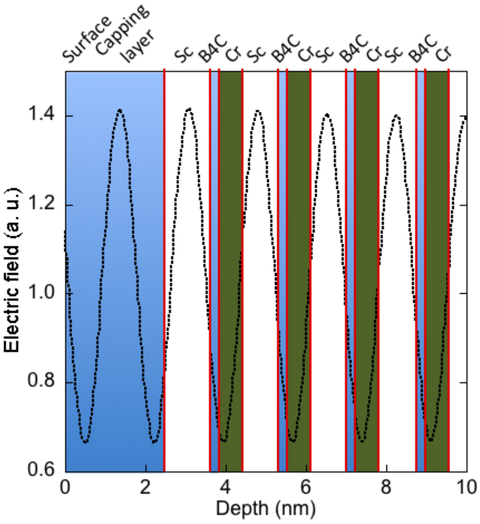

Figure 4.10: Depth distribution of the electric field generated within the Cr/B_4C/Sc multilayer by the emitted Sc Kα radiation. The calculation illustrated here is made for an angle -0.035° away from the Bragg angle. Only the capping layer and the first four periods of the multilayer are represented.

4.4 Conclusions

We tested and compared the optical performance of a series of multilayer mirrors based on the Cr/Sc system. B_4C barrier layers are found to be more effective at Sc-on-Cr interfaces than at Cr-on-Sc interfaces to improve the performance of the mirror: the reflectivity is increased by approximately 3 times (from 2.5% to 7.7%, which is the highest among the samples) at the energy of end-use application of the mirror (395 eV). The data indicates that B_4C barrier layer even has negative effect for the reflectivity of the mirror in the Cr-on-Sc case. Severe intermixing between Cr and B_4C is reported, which also causes the decrease of the period of the samples from 13% to 20% compare to the designed period. There is evidence that the introduction of nitrogen in the sputtering gas has positive effect (approximately doubled reflectivity) for the improvement of the performance of Cr/Sc system.

Two different methods, XRR and XRF-XSW, are simultaneously applied for the determination of both the layer thickness and roughness/interdiffusion of the Cr/CrB$_4$C/Sc sample with a parameter variation tolerance of 1.4%. In such way the determined structure of the sample is more reliable. To get a better fit of the XSW curve, we use an empirical model of the background originating from scattering and Kossel diffraction. Yet a mathematical calculation of the scattering is still in need to simulate it. For the moment the XRF-XSW simulation can be applied only as a verification method. But recent research declares success in fitting both XRR and XRF curves together [64], and we are trying to develop our own fitting process to make it possible to determine the structure independently with XRF-XSW. Like IMD for the XRR curve fitting, our process would be able to model several variables (thickness, roughness/interdiffussion, etc.) simultaneously for a XRF-XSW curve fitting. Eventually a structure of the multilayer with all variables will be obtained once a good agreement is reached between the experimental data and the simulation calculated with the variables.

We have observed for the first time the Kossel interferences of proton-induced X-ray emission lines in a multilayer. This was achieved by using a Cr/B$_4$C/Sc periodic stack and observing the Sc Kα and Cr Kα characteristic emissions. Owing to the low background radiation, the X-ray spectra lead directly to the Kossel curves. The agreement between the experiments and the simulation is excellent regarding the shape and position of the Kossel features, although it may be improved regarding the contrast of these features obtained in this pioneering experiment. The counting statistics for a given incident proton fluence could be improved by changing the angle of incidence between the protons and the sample surface and thus increasing the apparent thickness of the sample seen by the proton beam, or by using a colour camera [65] sensitive both to the location and energy of the detected X-rays. This second solution could provide 1 to 2 orders of magnitude greater X-ray yield per incident proton and could open the way for systematic use of proton-induced X-ray emission with Kossel interferences to probe the nanoscale layers and interfaces of periodic multilayers, see Chapter 5. Thus, it will become possible to obtain with proton-induced X-ray emission under Kossel interferences the same kind of results and information as those obtained by the widespread X-ray standing wave technique.

4.5 Related publications

The contents of this chapter are based on the following publications:

[1] Wu M, Burcklen C, André J-M, Guen K L, Giglia A, Koshmak K, Nannarone S, Bridou F, Meltchakov E, Rossi S de, Delmotte F and Jonnard P. Study of Cr/Sc-based multilayer reflecting mirrors using soft x-ray reflectivity and standing wave-enhanced x-ray fluorescence. *Optical Engineering*, 56, 117101, 2017.

[2] Wu M, Le Guen K, André J-M, Ilakovac V, Vickridge I, Schmaus D, Briand E, Steydli S, Burcklen C, Bridou F, Meltchakov E, de Rossi S, Delmotte F and Jonnard P. Kossel interferences of proton-induced X-ray emission lines in periodic multilayers. *Nuclear Instruments and Methods in Physics Research Section B: Beam Interactions with Materials and Atoms*, 386, 39–43, 2016.

Chapter 5: Study of Pd/Y based periodic multilayers

5.1 Introduction

The Pd/Y multilayer was first proposed and studied by Montcalm et al. [66]. Such material combination is promising as simulation gives an up to 65% reflectivity of such design for radiation with 9.5 nm wavelength. The potential applications vary from EUV spectroscopy, plasma diagnosis to synchrotron radiation or free electron laser instruments [67]. A crucial factor is found that may compromise the performance of the mirror: the interdiffusion of Pd and Y. Nitridation of the Pd/Y multilayer by introducing nitrogen during the deposition process can reduce the interdiffusion [68,69]. Inserting B_4C barrier layers at the interfaces is reported by Windt as another effective means to obtain smoother interfaces and thus improve the optical performance of the Pd/Y system [70].

In this chapter, we start by using hard X-ray photoemission spectroscopy combined with X-ray standing waves to characterize two series of Pd/Y multilayers designed to work in the 7.5-11 nm wavelength range. The samples of the first series are deposited either with or without nitrogen introduced in the sputtering gas while the ones of the second series are deposited with B_4C barrier layers located at different interfaces of the originally designed Pd/Y multilayer. The experiments consist in obtaining the core level spectra of the various elements for a series of grazing angles. The angular scan is made in the range given by the Bragg law, the multilayer period and the incident photon energy. Given the period of the multilayer and the presence of a 2.5 nm-thick B_4C capping layer, the photon energy is chosen to be 10 keV in order to probe the first 5-6 periods of the stack. Thus the Bragg angle is a little less than 1°.

Kossel diffraction of particle induced X-ray emission using 2 MeV protons is then performed for the same samples. The intensity of characteristic Pd Lα X-ray emission is measured as a function of the detection angle (grazing exit). An oscillation of its intensity is observed when the detection angle varies around the Bragg angle, which corresponds to the energy of the emission and the period of the multilayer. Use of the X-ray color camera enables the whole setup to be fixed so that no angular scan is required, greatly simplifying the experimental condition. From the features of the Kossel curves, we are able to deduce that nitrided Pd/Y multilayers exhibit much less layer intermixing than the non-nitrided multilayers. The experimental results show that it is possible to distinguish by the shape of Kossel curves of multilayers with B_4C barrier layers located in different interfaces. This demonstrates that Kossel diffraction is structural sensitive.

5.2 Theoretical prediction of interdiffusion

The mixing enthalpy ΔH is calculated using the Miedema model [71] to theoretically explain and confirm the existence of the interdiffusion between Pd and Y. For a material combination of two transition metals such as palladium and yttrium which can be treated as non-ordered alloy, the mixing enthalpy can be predicted using the following expression:

$$\Delta H = \frac{2Pc_{Pd}\, f_Y^{Pd} V_{Pd-alloy}^{2/3}\left[-\left(\phi_Y - \phi_{Pd}\right)^2 + \frac{Q}{P}\left(n_{ws}^{Y\ 1/3} - n_{ws}^{Pd\,1/3}\right)^2\right]}{n_{ws}^{Y\ -1/3} + n_{ws}^{Pd\,-1/3}} \qquad 5.1$$

$$f_Y^{Pd} = C_Y^S \qquad 5.2$$

$$C_Y^S = c_Y V_Y^{2/3} / (c_Y V_Y^{2/3} + c_{Pd} V_{Pd}^{2/3}) \qquad 5.3$$

where C^s is the surface density of each atom, c_{Pd} and c_Y are the mole fractions, V_{Pd} and V_Y are the atomic volumes of Pd and Y, respectively. *P* and *Q* are two constants which depend on the type of the system. Here, according to the literature [72], *P* is 14.1 and *Q/P*=9.4. *Φ* is the electronegativity, *V* is the molar volume and n_{ws} is defined as the electron density at the boundary of the Wigner-Seitz cell (its average over the cell boundary) as derived for the pure elements in the metallic state. The values of the used parameters are given in Table 5.1. The electron densities are usually given in terms of density units (1 d.u. = 6.75×10^{22} electron/cm^3. As the combination of the two metals leads to a change in terms of the atomic volume, another volume expression is required, which is:

$$V_{Pd-alloy}^{2/3} = V_{Pd}^{2/3}\left[1 + a f_Y^{Pd}\left(\phi_Y - \phi_{Pd}\right)\right] \qquad 5.4$$

where *a* is constant equal to 0.04 for Pd according to the Miedema model.

Table 5.1: Constants used in the calculation of mixing enthalpy according to the Miedema model.

Element	**Φ (V)**	**n_{ws} (d.u.)**	**V(cm^3/mol)**

Pd	5.45	4.66	8.92
Y	3.20	1.77	19.72

In Equation 5.1, the first negative term in the bracket is proportional to the square of difference in the electronegativity parameters, which shows the tendency for compound formation. The second positive term presents the discontinuity in electron density at the Wigner-Seitz boundary of Pd and Y, which elucidates the tendency of phase separation. With all considerations mentioned above, the result of the calculation is presented in Figure 5.1 where a negative ΔH value is obtained for any mole fraction, indicating that the mixing of these two metals is expected for this system. Such prediction is verified from the Pd-Y binary phase diagram [73] showing that multiple possible compounds may form. Unfortunately the constants for the calculations concerning B_4C are not available in the literature to our knowledge, thus the intermixing of Pd-B_4C and Y-B_4C cannot be predicted with mixing enthalpy.

However the enthalpy of formation ΔHf of palladium as well as yttrium borides and carbides can be found in the literature [74]. For B_4C/Pd the enthalpy of formation is positive, indicating a low probability of the formation of chemical compound. However for Y, ΔHf of YB_2, YB_4, Y_2C and Y_2C_3 are -36, -52, -32 and -51 respectively in kJ/mol. The chemical reactions of Y-B and Y-C are then expected. Yet seen the values, the chemical selectivity of the reactions (Y-B or Y-C) cannot be predicted. The ΔH_f of Y/Pd is found to be -94 kJ/mol as another evidence of the Pd-Y interdiffusion, in agreement with our calculation of mixing enthalpy with different Pd-Y mole fractions.

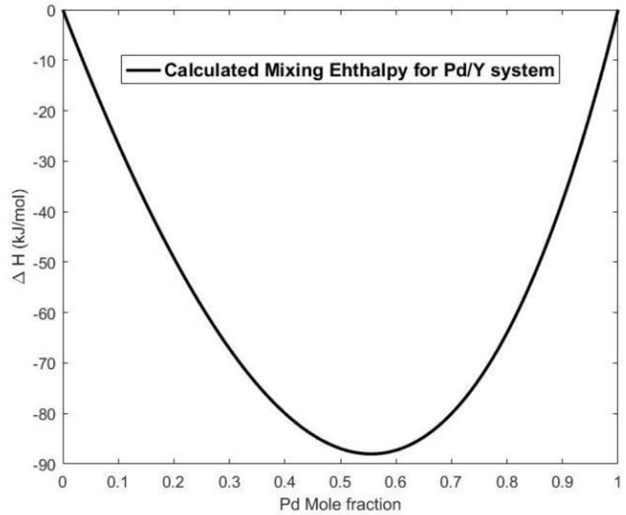

Figure 5.1: Calculated mixing enthalpy for the Pd/Y system according to the Miedema model.

5.3 Experimental methods

5.3.1 Deposition of the samples

Samples are deposited using DC magnetron sputtering technique. The original design for the mirror is Pd/Y repeating 40 times and deposited on sliced and polished Si (100) wafers with a 4 nm period thickness (2 nm Pd and 2 nm Y). A 2.5 nm B_4C capping layer is deposited on top of the sample to prevent the oxidation of the component metals.

The samples of the first series differ by the sputtering gas, for which a mixture of argon (Ar) and nitrogen (N_2) gases was used. The purpose of adding N_2 during the deposition is to passivate the layers for a better stability of interfaces and essentially decrease the interdiffusion between Pd and Y layers [68]. The volumetric concentration of nitrogen in the sputtering gas varies from 0% to 8% for different samples. For the deposition of each sample, the sputtering gas remains the same during the whole process, that is to say Pd, Y and B_4C layers are deposited in the presence of nitrogen.

Three other samples are prepared for the second series: 1 nm thick B_4C barrier layers are inserted at either interface of these two metals or even both interfaces to prevent the interdiffusion of the two metals. Thus the new structures of the samples are B_4C/Pd/Y (1/2/2 nm), Pd/B_4C/Y (2/1/2 nm) and B_4C/Pd/B_4C/Y (1/2/1/2 nm). The order of the layer is from the top to the bottom of the stack, so B_4C/Pd/Y means B_4C-on-Pd, then Pd-on-Y, Y-on-B_4C and so on. Considering the X-ray attenuation and the IMFP of the emitted photoelectrons, we grow only 20-period structures for the last sample, which is thicker than others, instead of standard 40-period original structures.

5.3.2 Hard X-ray photoelectron spectroscopy

Selection of the incident beam energy for HAXPES

Two different incident energies of the photons were chosen for the measurements: 3 and 10 keV. We chose 10 keV for long enough inelastic mean free paths, see Table 5.2. In this case, the calculated inelastic mean free path of Pd $3d_{5/2}$ photoelectron is 8.5 nm [4545] (thus 9665 eV kinetic energy of the photoelectron) and we were able to probe approximately

25 nm, which represents the first 5 to 6 periods below the B_4C capping layer. Even for Pd $2p_{3/2}$ for which the inelastic mean free path is 6.4 nm, a 19 nm probe depth is expected (no more than 4 periods probed). The 3 keV beam is, on the other hand, relatively more sensitive to the surface. A 3.0 nm inelastic mean free path leads to an analyzed thickness around 9 nm, which is no more than the two first periods of Pd/Y. With such energy we can focus on the effect of the protection against the oxidation provided by the B_4C capping layer.

Table 5.2: Cross section for the incident photons and calculated inelastic mean free path for the corresponding photoelectrons.

Comparison of two chosen incident beam energies

Incident beam energy	Core level	Cross section	Kinetic energy	Inelastic mean free path
3 keV	Pd $3d_{5/2}$	1.396×10^{-24} m^2	2665 eV	3.0 nm
10 keV	Pd $3d_{5/2}$	1.694×10^{-26} m^2	9665 eV	8.5 nm
10 keV	Pd $2p_{3/2}$	6.516×10^{-25} m^2	6827 eV	6.4 nm

Using hard X-rays is quite beneficial in the aspect of the probed depth, but it brings disadvantage at the same time, which is the small cross section, see also Table 5.2. For Pd $3d_{5/2}$ level, as the incident photon energy increases from 3 to 10 keV, the cross section drops from 1.4×10^{-24} m^2 to 1.7×10^{-26} m^2 [75], which is only 1.2% of the previous one. A smaller cross section inevitably leads to a weaker intensity of the detected signal. That is why such measurements call for high brilliance synchrotron source.

Instrumental setup

The HAXPES measurement was performed on the GALAXIES beamline [20] of the SOLEIL synchrotron facility where a monochromatic focused beam is provided with the highest flux possible in the 2.4-12 keV spectral range with the photon energy bandwidth between 100 meV and 1 eV. The kinetic energy of the photoelectrons is measured with a hemispherical electron analyzer. For the angular scans for the XSW measurements, the achievable angular resolution is approximately equal to 0.008°. The instrumental setup is presented in Figure 5.2(A). The samples were setup on a goniometer so that the angle between the incident photon beam and the sample surface was well defined and close to the first order Bragg angle which is corresponding to the photon energy and the multilayer period. The electron analyzer was placed perpendicular to the incident beam in the reflecting plan. The angle between the incident beam and the sample can be changed by rotating the sample. According to the simulation an over 70% reflectivity of the incident radiation can be expected at the first order Bragg angle. This indicates an intense x-ray standing wave field, leading to a clear depth distribution of the ionization rate as presented in Figure 5.2(B) for the $B_4C/Pd/B_4C/Y$ sample. The enhanced ionization can be found at the anti-nodal plans of the field while the reduced ionization can be found at the nodal plans.

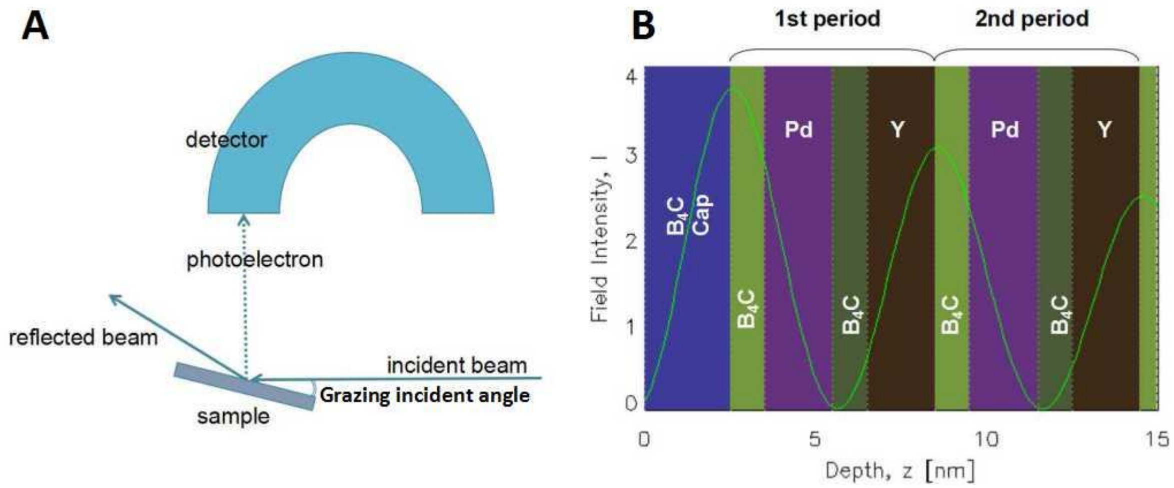

Figure 5.2: (A) Scheme of the instrumental setup, (B) calculation of the depth distribution of the x-ray standing wave electric field within the $B_4C/Pd/B_4C/Y$ multilayer (6.2 nm period), with the incident beam (10 keV) introduced at first order Bragg angle (0.63°).

Energy calibration of the HAXPES spectra

The energy of the photoemission spectra were calibrated with Au 4f core level peak. We performed the reference measurement for a pure gold sample with all the experimental conditions same as those with the multilayer samples, including incident beam energy (both 3 and 10 keV) and scanning interval of the grazing incident angle calculated respectively. Along the scanned angular range we found around 0.12 eV variation of the energy offset as presented in Figure 5.3. This energy offset is used to complete the relation between the measured kinetic energy of the photoelectron and binding energy which is between core level and Fermi level. However in the interesting zone where the XSW feature is expected, which is about 0.75-1.05° and 2.7-3.2° for 10 and 3 keV measurements respectively, the variation is limited to 0.05 eV. Such variation is small enough to be considered as uncertainty, thus we consider the energy offset as a constant. Quantitatively speaking we set the values of the energy offset to 5.0 eV for 3keV measurements and 19.3 eV for 10 keV measurements.

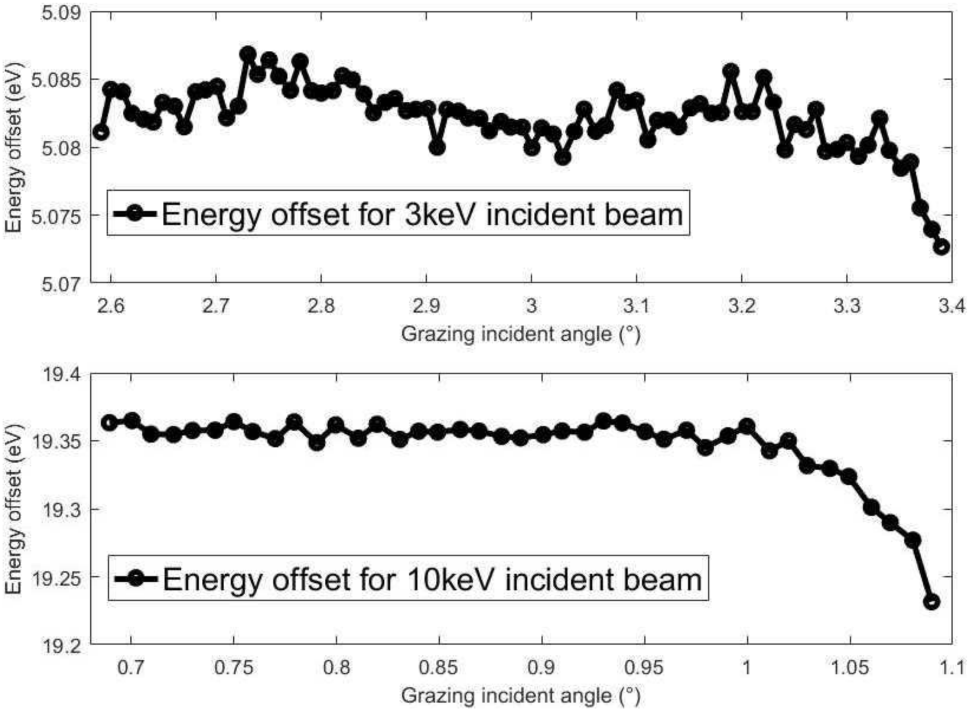

Figure 5.3: Energy offset for 3 keV (top) and 10 keV (bottom) incident beams as a function of the grazing angle, *i.e.* the angle between the sample surface and the direction of the incident beam. Angular range is selected as the same for the XSW measurements for the Pd/Y multilayer samples.

We measured Pd $2p_{3/2}$ and $3d_{5/2}$, Y $2p_{3/2}$ and $3d_{5/2}$, B 1s, C 1s, N 1s and O 1s HAXPES spectra. For each characteristic photoemission a series of spectra was obtained for different grazing incident angles, the Pd $2p_{3/2}$ spectra of the sample prepared with 6% of N_2 are recorded at a photon energy equal to 10 keV. There is an obvious variation of the intensity of the spectra around the Bragg angle (0.8-0.9°) forming a particular shape, which is the typical feature of XSW effect. For each spectrum we calculate the integral of the photoemission peak intensity considering a Shirley background [76]. The so-called XSW curves are obtained by depicting the integrated intensity as a function of the grazing incident angle.

5.3.3 Particle induced X-ray emission

The proton beam is generated by the Van de Graaff accelerator of the SAFIR platform. The proton energy is set at 2.0 MeV, which is suitable to ionize the Pd atoms in their L shell uniformly through the whole multilayer. The energy loss of the proton beam is only about 0.5% after penetrating the multilayer whose total thickness is approximately 200 nm.

X-ray color camera

The X-ray color camera, or energy sensitive CCD camera, is an iKon-M from Andor Technologies equipped with a 1024×1024 sensor array with 13×13 μm pixels. Instead of using the native spatial resolution, we select a 4×4 binning leading to a resolution of 256×256. Such selection improves the energy resolution by minimizing the charge sharing effect between adjacent pixels while still providing adequate angular resolution. It also simplifies the data treatment by reducing the size of data files. The camera spans an angular range of 2.7° corresponding to 256 horizontal pixels in Figure 5.4.

For a given X-ray emission, we measure its intensity as a function of the detection angle with the X-ray color camera while irradiating the sample with the proton beam. The experimental setup is schematically presented in Figure 5.4 where the X-ray color camera is placed perpendicular to the incident proton beam with a 200 μm beryllium film to filter the scattered protons. The experimentally obtained image of particle induced X-ray emission (PIXE) presented in Figure 5.4 is the spatial distribution of total X-ray intensity on the detected area for B_4C(2.5 nm)/[Pd(2 nm)/B_4C(2 nm)/Y(2 nm)]$_{\times 40}$/Si multilayer obtained after a 2 hour irradiation with about 35 nA of 2 MeV protons in a 2 mm beam spot. This corresponds to about 5×10^{16} protons cm^{-2}. The Kossel feature cannot be observed on this image yet. It requires further treatment, which will be explained later, to be extracted from this image.

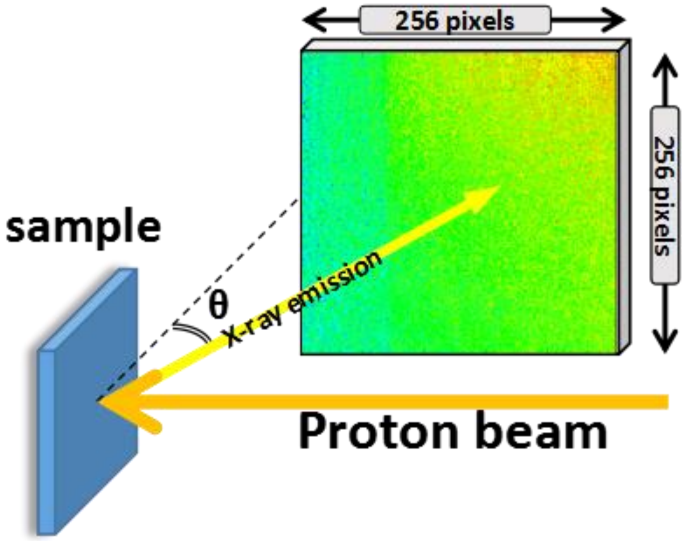

Figure 5.4: Geometry of the experimental setup. θ is the detection angle. The presented experimental image is the spatial distribution of total X-ray intensity on the detector array for B_4C(2.5 nm)/[Pd(2 nm)/B_4C(2 nm)/Y(2 nm)]$_{\times 40}$/Si multilayer irradiated as described in the text.

Acquisition of PIXE-Kossel curves

Note that a complete X-ray spectrum is recorded by each pixel of the X-ray color camera. To identify the emission peaks, we sum the spectra recorded by all pixels in order to get more reliable statistics. An overview (intensity in log scale) of the summed X-ray spectrum of the B_4C(2.5 nm)/[Pd(2 nm)/B_4C(2 nm)/Y(2 nm)]$_{\times 40}$/Si sample as well as the zoomed range of interest (intensity in linear scale) are presented in Figure 5.5. The Y Kα emission can be observed on the spectrum at photon energy near 15 keV, but due to its low intensity and small estimated angular range for Kossel detection (about 0.5° grazing exit angle, in the total reflection zone), it would not be possible to observe its Kossel oscillation. The energy calibration of the spectrum is carried out with Pd Lα (2.838 keV) and Y Kα (14.958 keV) peaks. Y Lα and Si Kα emissions are not considered because their energies are close to the low energy limit of the camera and their detection is not as efficient as Pd Lα emission. Pd Lβ emission is not discussed either because its intensity is much less than that of the of Pd Lα emission and would not bring supplementary information. The Pd Lα1 and Lα2 emissions are not resolved, the difference in their energies being less than the detector resolution of about 150 eV at Mn Kα (5.9 keV).

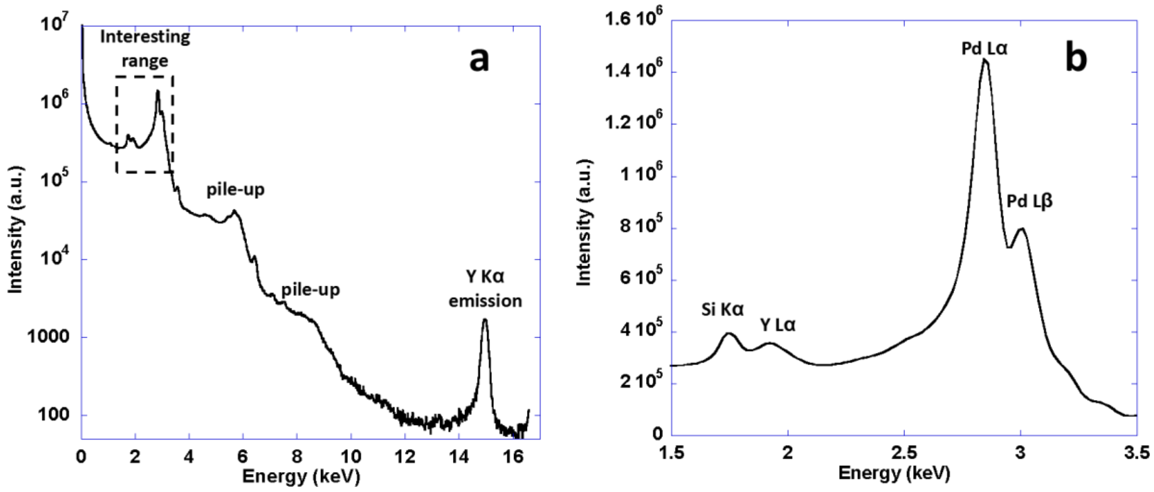

Figure 5.5: Spectrum of B_4C(2.5 nm)/[Pd(2 nm)/B_4C(2 nm)/Y(2 nm)]$_{\times 40}$/Si multilayer: (a) overview, intensity in log scale; (b) zoomed range of interest, intensity in linear scale.

A region of interest (ROI) is placed on the spectrum in order to distinguish the Pd Lα emission from other photons, see Figure 5.6(a) where the intensity of Pd Lα emission is obtained by integrating the shadowed area. The ROI width of 100 eV is based on a compromise between obtaining good statistics and limiting the influence of the Pd Lβ emission. An image of the spatial distribution of the Pd Lα emission intensity (Figure 5.6(b)) is obtained after applying the energy filtering ROI of Figure 5.6(a) to the total intensity image presented in Figure 5.4. While it is not possible to observe the Kossel feature in Figure 5.4, now it can be clearly seen in Figure 5.6(b). Finally we integrate this filtered image along the vertical pixels in order to obtain the Kossel curve which is presented in Figure 5.6(c).

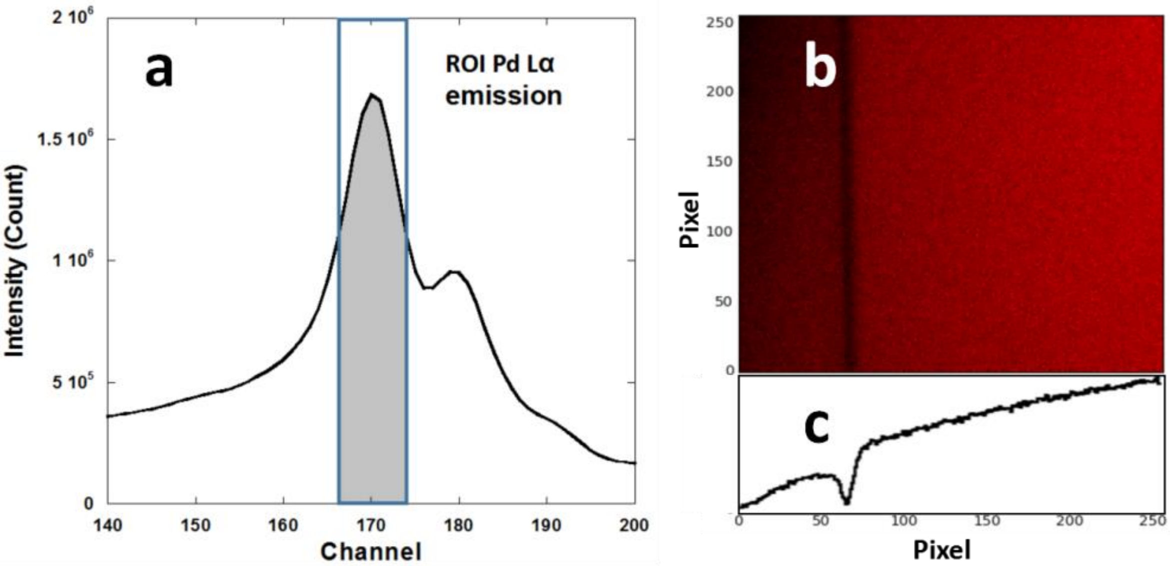

Figure 5.6: (a) Selection of the ROI for Pd Lα emission; for the case already depicted in Figure 5.5(b); (b) image of the intensity of X-ray emission, of which the energy is in the ROI; (c) Kossel curve depicted by integrating the X-ray emission intensity along the vertical pixel.

The ROI imaging method is practical to obtained the PIXE-Kossel curve. However the intensity integral in the ROI takes into account the background of the spectrum, causing the inaccuracy of the PIXE-Kossel curve. To optimize the acquisition, batch fitting is performed based on preset emission peaks. That is to say, for each horizontal position of the X-ray camera in Figure 5.4, we sum up the spectra along the vertical pixel. In this way, for each angle value, one corresponding X-ray emission spectrum is obtained. The idea is to fit each spectrum of each angle separately and extract the intensity of the desired characteristic emission to draw the PIXE-Kossel curve. Figure 5.7 presents the fitting of one of the spectra. The spectral background is eliminated as well as the influence of the “tails” of neighbor emission peaks.

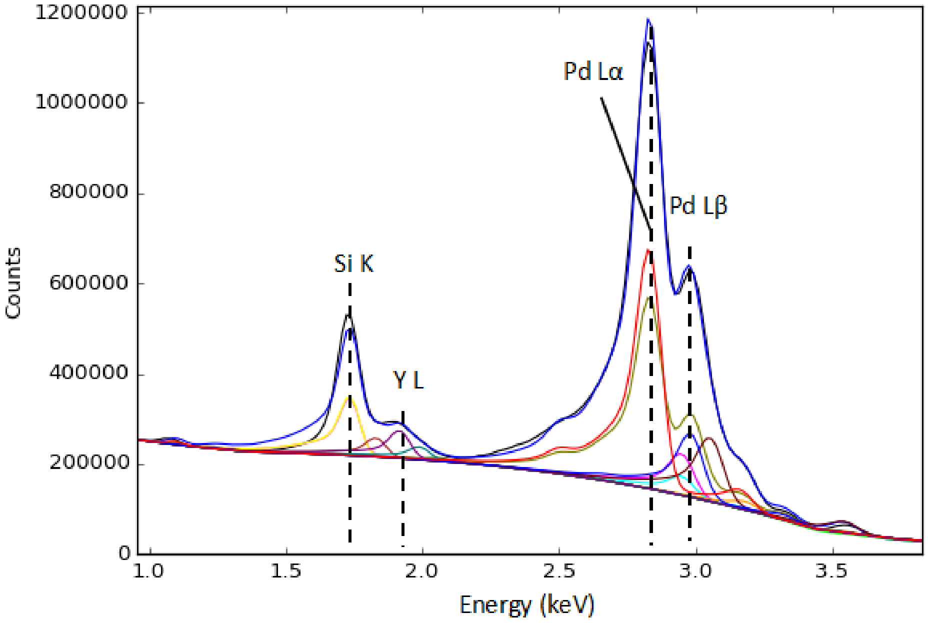

Figure 5.7: Fitting of the X-ray emission spectrum of a B_4C/Pd/B_4C/Y multilayer bombarded by a 2 MeV proton beam.

Figure 5.8 shows the comparison between the two data treating methods. By applying batch fitting, we inevitably lose intensity and eventually statistics of the acquisition. Yet the advantage of batch fitting speaks for itself in Figure 5.8(b) where the oscillation of the curve at about horizontal pixel (channel) 50 disappears compared to the curve obtained by ROI imaging. Such position is related to the Kossel feature corresponding to the Pd Lα emission. Batch fitting cleans the influence of the Pd emission over Y emission, making the PIXE-Kossel curve more precise and reliable.

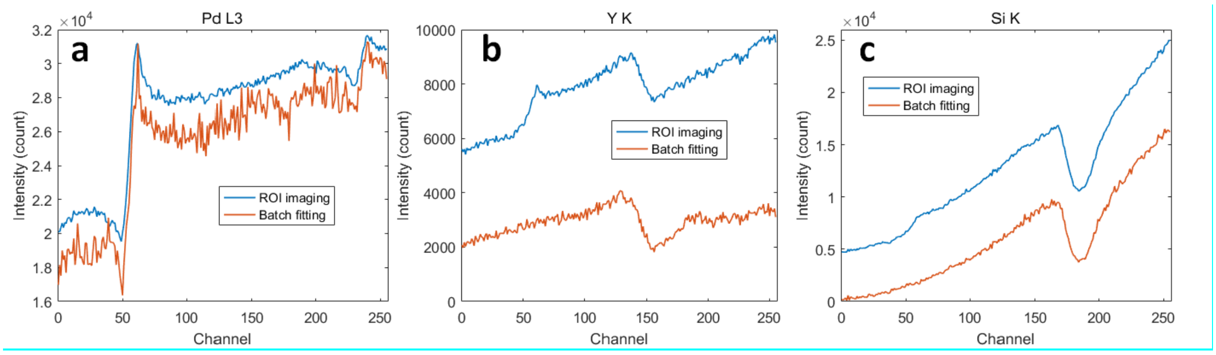

Figure 5.8: Comparison of PIXE-Kossel curves of a B_4C/Pd/B_4C/Y multilayer bombarded by a 2 MeV proton beam obtained by ROI imaging and batch fitting: (a) Pd Lα, (b) Y L, (c) Si K.

Besides, if we put aside the intensity loss and consider only the shape of the PIXE-Kossel curves, the one obtained by batch fitting presents a slightly higher contrast (Figure 5.9).

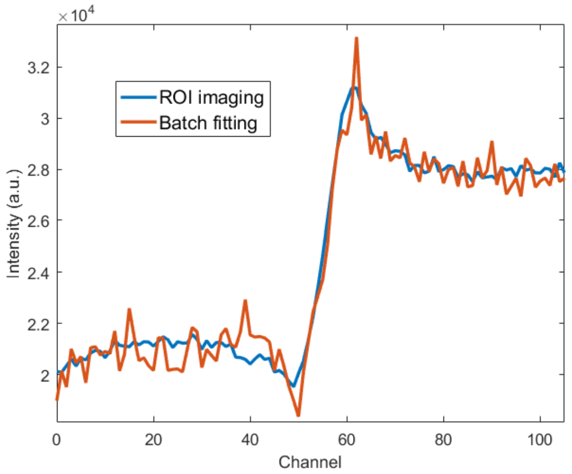

Figure 5.9: Detail of Pd Lα PIXE-Kossel curves of a B_4C/Pd/B_4C/Y multilayer bombarded by a 2 MeV proton beam obtained by ROI imaging and batch fitting.

Advantageous as it is, batch fitting is not selected for the data analysis because the fitting configuration must be adjusted all time according to the spectrum and the concerned characteristic X-ray emission peaks. Thus it is difficult to find a uniform configuration to analyse all the spectra. For a global comparison of all samples, ROI imaging is selected eventually.

Stability of the measurement

To check the stability of the measurement and possible sample damage from the proton irradiation, we consider the sample B_4C(2.5 nm)/[Pd(2 nm)/B_4C(2 nm)/Y(2 nm)]$_{\times 40}$/Si and continue measuring for over 7 hours. The result is presented in Figure 5.10 where the curve intensities are normalized by the proton beam current and the acquisition time. We divide this series of measurements into 4-time slices and depict separately the related Kossel curves of Pd Lα emission to see if any deformation of the Kossel feature happens. The oscillation maintains its shape, indicating that the structure of the multilayer is not changed during the measurement and the proton beam causes no discernible change to the sample structure. We can safely say that the whole experiment is non-damaging because the standard acquisition time for each sample is about 2 hours.

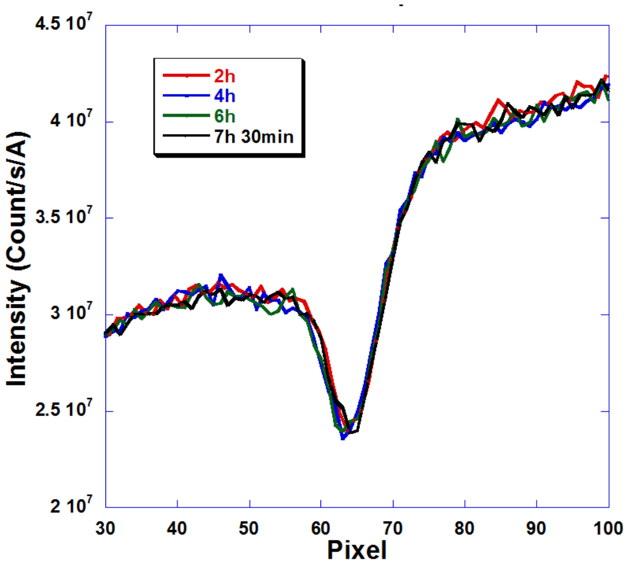

Figure 5.10: Non-damaging test of the sample B_4C(2.5 nm)/[Pd(2 nm)/B_4C(2 nm)/Y(2 nm)]$_{\times 40}$/Si.

Angular calibration

The relation between the grazing exit angle and the channel in pixel of the detector is determined with the angular variation of Pd Lα emission intensity of the 4-layer sample B_4C(2.5 nm)/[B_4C(1 nm)/Pd(2 nm)/B_4C(1 nm)/Y(2 nm)]$_{\times 20}$/Si where both the first and second orders of the Kossel diffraction can be observed. The calibration method, which is based on the comparison between experimental and simulated Kossel curves, is presented in Figure 5.11. The experimental data and its derivative enable us to locate the position of the Kossel oscillation in pixels, which together with the angle of the Kossel oscillation from simulated curve gives 1° equals to 94.42 channel. Thus the angular range of the X-ray color camera is 256/ 94.42 = 2.71°. The simulation method will be presented later.

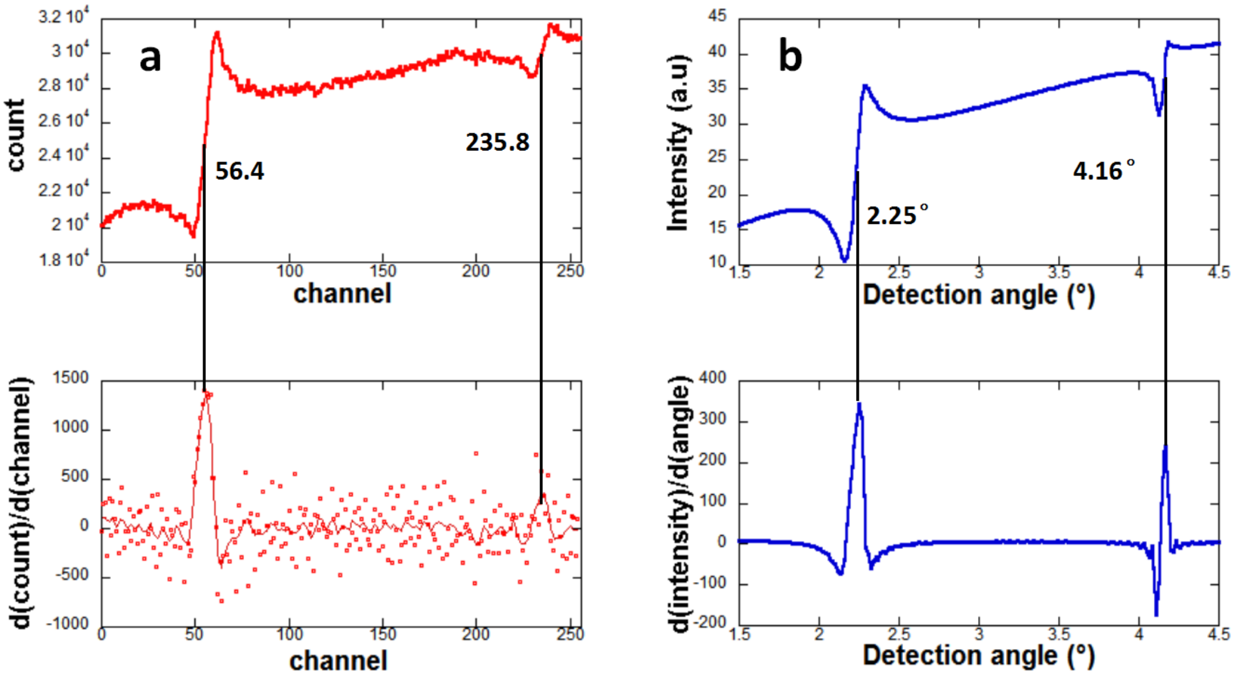

Figure 5.11: Calibration of the detection angle using the comparison between a) experimental and b) simulated Kossel curves.

5.4 Results and discussions

5.4.1 Pd/Y multilayer with nitridation

Grazing incident reflectometry

The experimental and fitted GIXR curves are presented in Figure 5.12. The parameters, *i.e.* thickness and interface width of the various layers, of the samples are then extracted from the fitting procedure and are listed in Table 5.3. The interface width in this table stands for both the geometrical roughness and the interdiffusion of the materials at the interfaces between the described layer and the previous one. For a Pd/Y multilayer modeled with perfect interfaces (no interface roughness nor interdiffusion), we expect a high reflectance as presented in Figure 5.12 (dotted line). However the interdiffusion, as predicted, is so severe that we barely observe the reflectance peak at the first order Bragg angle even seeing the curve in logarithm scale. The value of the interface width is almost as high as the layer thickness itself and the interferential contrast between different layers is almost completely lost. Nitridation of the multilayers during the deposition process obviously improve the quality of the mirrors as intense Bragg peaks appear on the GIXR curves for all nitridated samples as shown in Figure 5.12, indicating a much better defined periodicity.

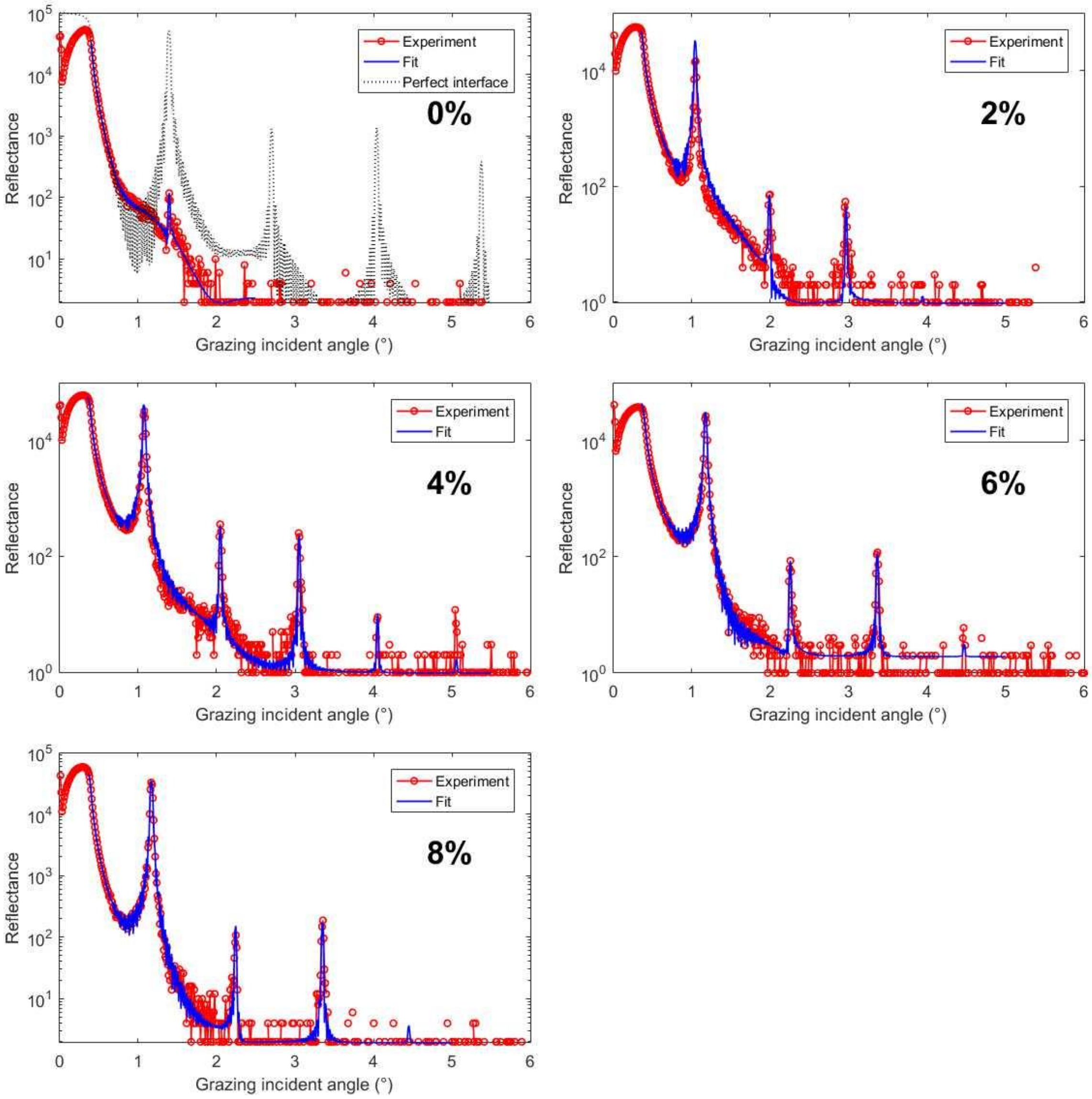

Figure 5.12: Measured (red dots) and fitted (blue lines) GIXR curves of the multilayers with different concentration of nitrogen in the sputtering gas (logarithm scale). The dotted line in A presents the calculated reflectance of the original design without interface roughness nor interdiffusion.

The same conclusion can be drawn by reading from Table 5.3 showing the layer thickness and interface width for each sample. The nitridated samples have much smaller values of interface width, indicating that the interdiffusion between Pd and Y is well reduced.

Table 5.3: Designed structures and values of the parameters extracted from the fit of the experimental GIXR curves of the samples.

Sample	**N_2 in the sputtering gas**	**Designed Pd/Y thickness (nm)**	**Pd/Y thickness** (and interface width) **(nm) extracted from the fitting of GIXR curves**
1	0%	2/2	**1.87** (1.67) / **1.43** (1.35)

2	2%	2/2	**2.25** (0.56) / **2.26** (0.45)
3	4%	2/2	**2.20** (0.51) / **2.18** (0.32)
4	6%	2/2	**2.05** (0.41) / **1.92** (0.33)
5	8%	2/2	**2.17** (0.34) / **1.88** (0.34)

HAXPES with 10 keV incident beam

We present in Figure 5.13 the XSW curves of the characteristic photoemissions of Pd/Y multilayers prepared with 2, 4, 6 and 8% of N_2 respectively measured with the 10 keV incident photon energy. The XSW curve of the sample deposited in the pure Ar sputtering gas was not measured since it presented a poor reflectivity, which prevents the formation of an intense and well-contrasted oscillating electric field. Such poor reflectivity is predicted by the calculation using Miedema's model in Section 5.2 as a result of severe interdiffusion. On each standing wave curve (except for the noisy ones), we observe a peak and a valley which represent the standing wave enhancement and reduction respectively. Depending on the considered core level peak in the photoemission spectra, the peak in the XSW curve can occur at lower angle than the valley or inversely. We take the sample deposited with 8% nitrogen mixed in Ar as an example, when the incident angle draws close to the Bragg angle, the constructive interferences first occur in Y layers and we observe a peak on the Y (both 2p and 3d) standing wave curve. Given that the period of the electric field equals to the period of the stack, we observe the valley on the Pd (both 2p and 3d) standing wave curve representing the destructive interferences. We keep increasing the incident angle, and the constructive interferences move from Y layers to Pd layers. As a result we observe that the Y curve drops into the valley while the Pd curves rises to form a peak.

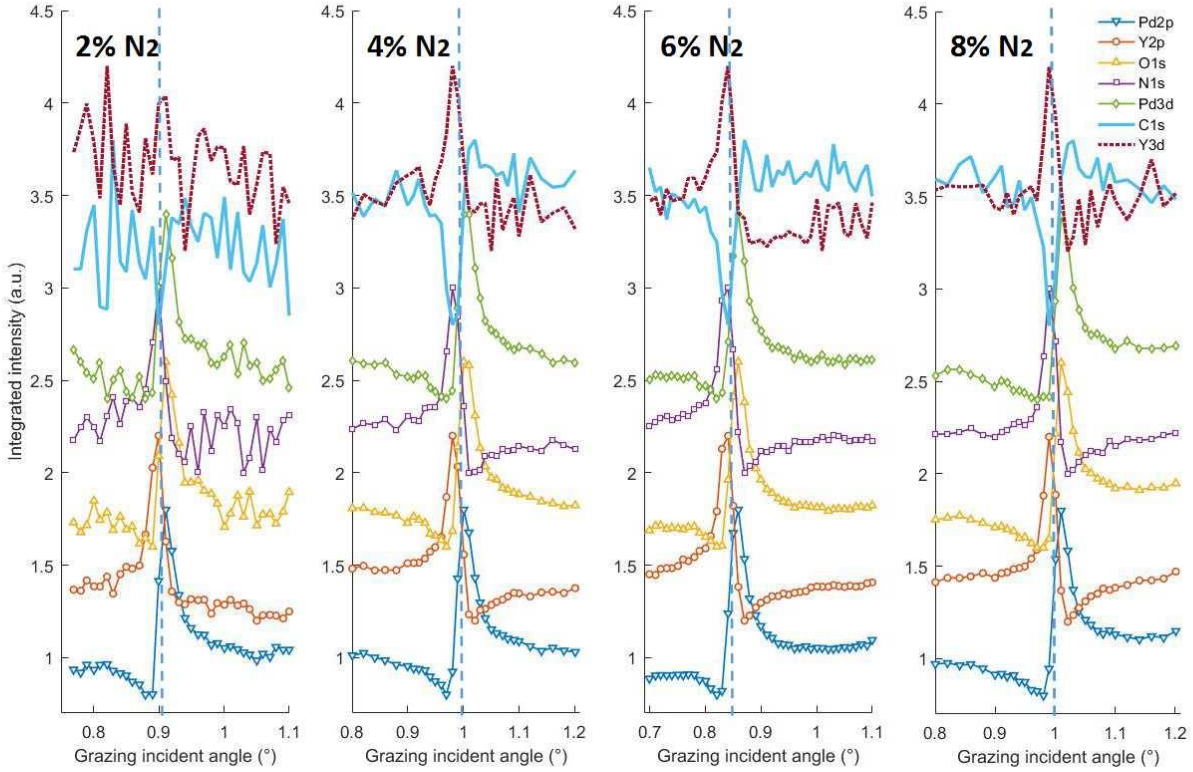

Figure 5.13: XSW curves, extracted from photoemission spectra, of the Pd/Y multilayers prepared with 2, 4, 6 and 8% of N_2 respectively measured with a 10 keV incident photon energy. The corresponding Bragg angle of each sample is presented with the vertical dot line.

O 1s standing wave curves are found to be similar to the Pd 2p and 3d curves. They all show a valley first (at the same incident angle) and then the peak (at another same incident angle) on their curves. If we focus on the peak position and shape of the N 1s and the Y 2p and 3d XSW curves, we find that the curves for the samples prepared with 4, 6 and 8% of N_2 have the similar shape (there is too much noise in the sample with 2% of N_2, especially for the Y 3d curve). At the first glimpse of such phenomenon, we thought it reveals the chemical selectivity of these four elements (Pd-O and Y-N). Yet one may find loophole by consulting the electron binding energy database. The O 1s level binding energy is expected to be about 533 eV, close value is found for Pd $3p_{3/2}$ level (532-533 eV for Pd metal). The O 1s photoemission peak is in fact masked by the Pd $3p_{3/2}$ peak, causing the false impression that O shares the same depth profile with Pd. The same conclusion can be drawn for N (1s) and Y (3s).

Caused by unexpected coincidences of the similarity in electron binding energies, such conclusion is disappointing. Yet it serves as an important alarm for the future study and experiment design. To study the oxidation or nitridation of the materials, it is suggested to avoid certain elements of which certain core levels possess similar electron binding energy with the ones of O and N. Such elements include but are not limited to Pd, Y (3s 392 eV), Mo ($3p_{3/2}$ 394 eV), Sc ($3p_{3/2}$ 398 eV), ...

However we are still able to retrieve some information about the effect of N on the Pd-Y interface. A standard peak decomposition treatment for photoemission is done for the Y 2p spectra, see Figure 5.14. The spectrum in Figure 5.14 (left) is actually the sum of all spectra of different grazing incident angles. We consider this in order not to miss any possible chemical components. A 4-peak model is used originally, but in the end only 2 components are necessary to fit the experimental data (namely Y metal and Y-N bonding). Then the XSW curves are depicted, but this time instead of integrating the total intensity of the experimental data, we distinguish the two components by integrating separately the sub-peaks, see Figure 5.14 (right). The XSW curve of Y-N is divided by its intensity ratio to the Y metal peak since the Y-N peak intensity is very weak compared to the Y metal peak. As a result, we confirm that the nitrogen distribution in the Y layers is homogeneous. The N 1s decomposition is not presented here as multiple chemical components are found for N, and we are yet to find which one represents N-Y chemical bond.

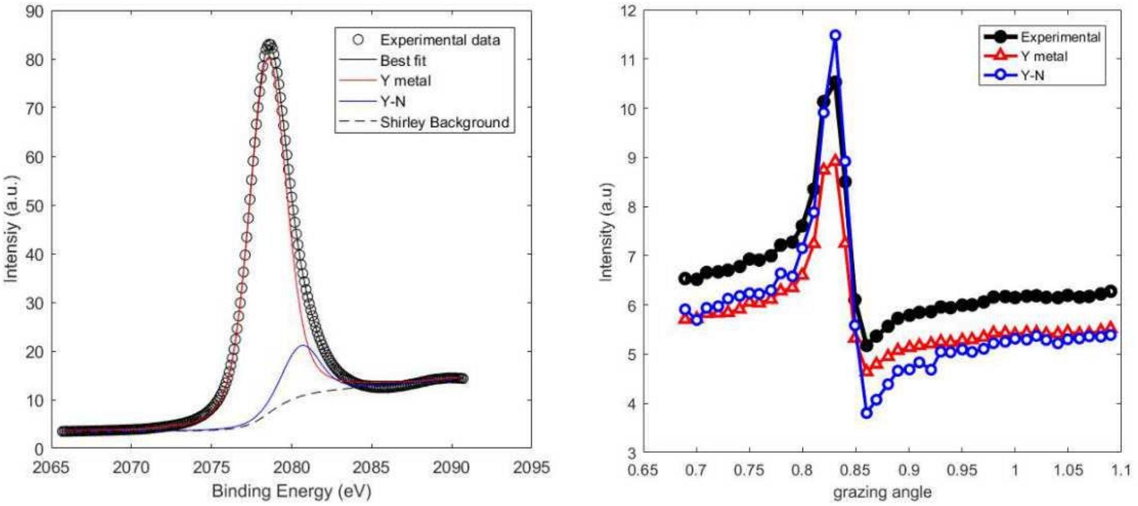

Figure 5.14: Y $2p_{3/2}$ photoemission spectrum of the sample with 6% nitrogen in the sputtering gas (left), and the XSW curves corresponding to the sub-peaks (right).

A clear difference is found in contrast of the XSW curves that represent Y metal and Y-N bond. This is an evidence that YN has a relatively sharpened interface against Pd compared to Y metal as presented in Figure 5.15. Such result is in line with the one reported in the literature [68] that the formation of YN could be the reason that the interdiffusion is reduced.

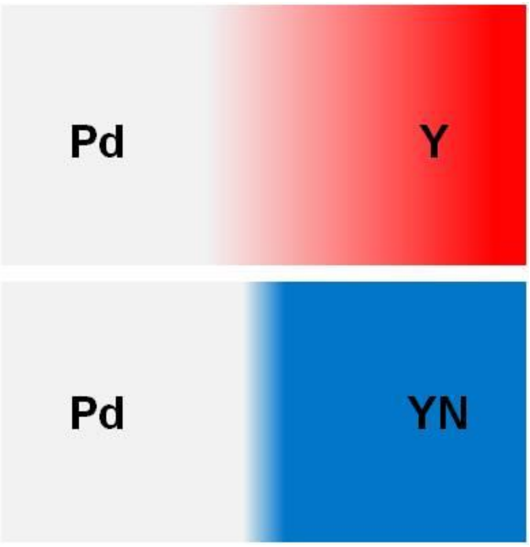

Figure 5.15: Schema of material distribution at Pd-Y interface.

HAXPES with 3 keV incident beam

We present the XSW curves obtained by irradiating the samples prepared with 2, 4 and 6% of N_2 respectively with a 3 keV incident photon energy. The results are shown in Figure 5.16. The effect of nitrogen against interdiffusion is clear as we can barely observe the XSW feature of Y 3d and N 1s curves of the 2% nitrogen sample, and the feature becomes observable in the other two samples with higher nitrogen concentration.

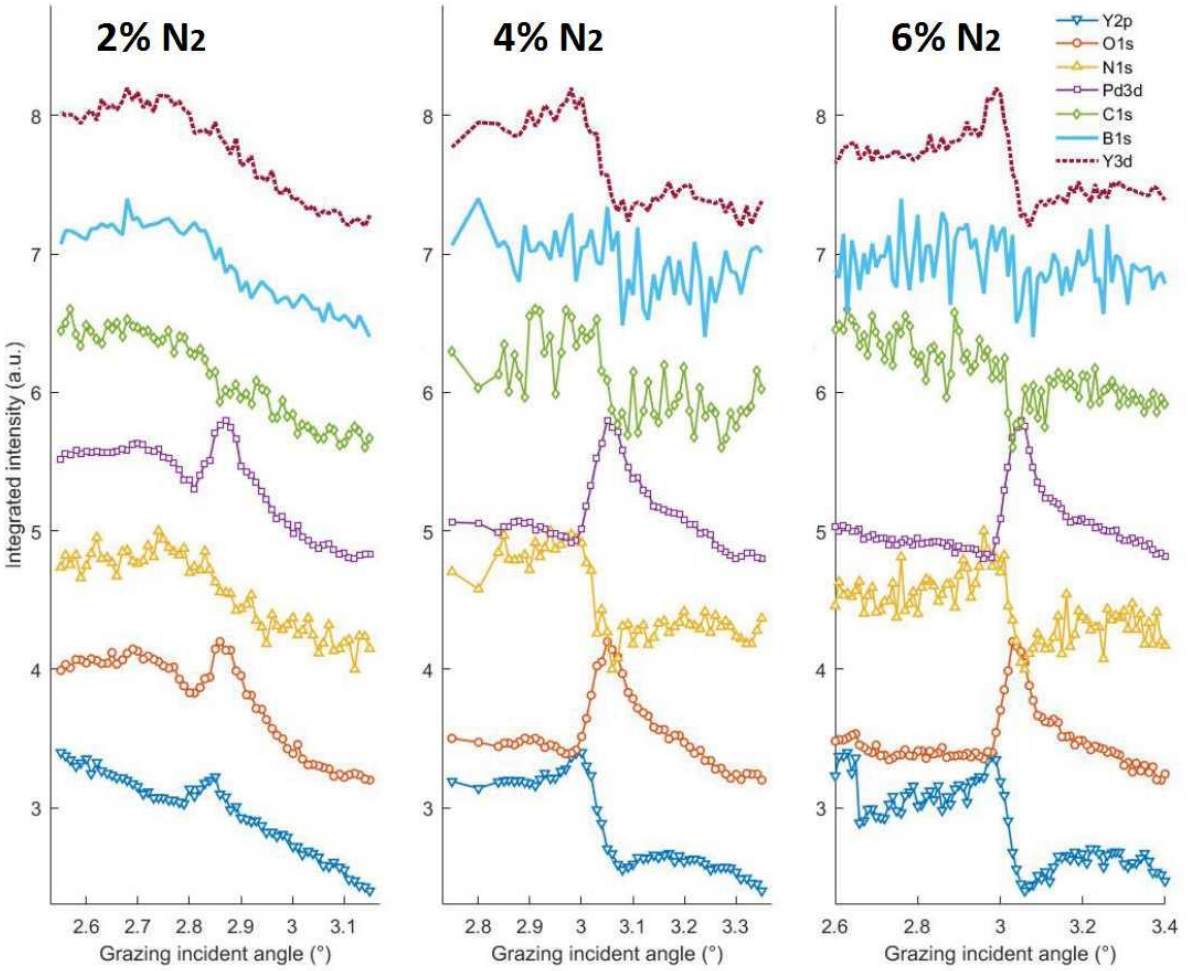

Figure 5.16: XSW curves, extracted from photoemission spectra, of the Pd/Y multilayers prepared with 2, 4 and 6% of N_2 respectively measured with a 3 keV incident photon energy.

It is noticeable that, when the nitrogen concentration in the sputtering gas increases, the B 1s and C 1s XSW curves become noisy owing to the decrease of their spectral intensities. This phenomenon is due to the rise of B_4C sputtering yield as the nitrogen content increases in the sputtering gas during the deposition. The sputtering time was reduced in order to maintain the thickness of the capping layer. As a result the B_4C capping layer was actually thinner than expected. This can be experimentally observed by comparing the total B 1s photoemission intensity (the integral of the photoemission peak) of these samples as shown in Figure 5.17.

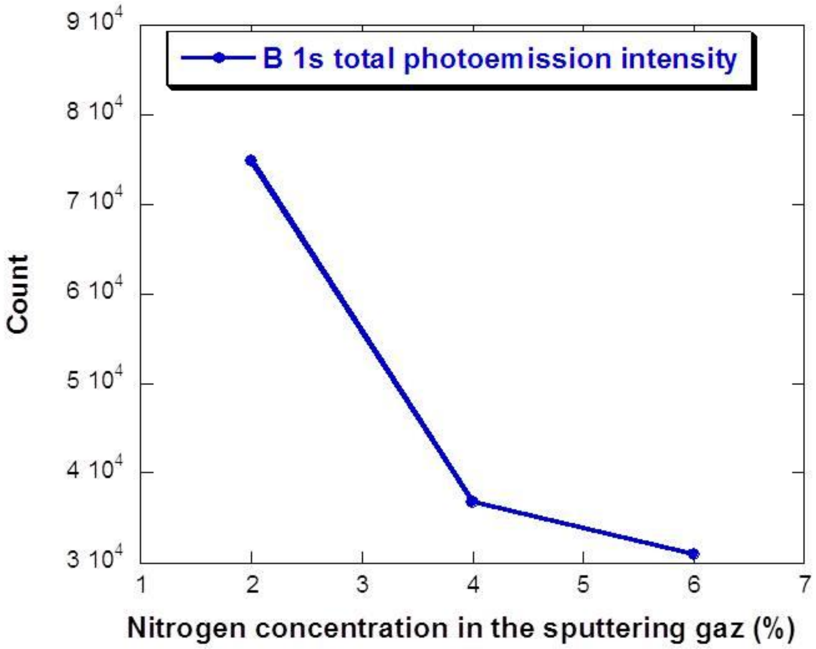

Figure 5.17: B 1s photoemission intensity as a function of the nitrogen concentration in the sputtering gas during the deposition of the samples.

Decomposition of B 1s and C 1s HAXPES spectra

To verify in a more detailed means the capping layer loss upon the introduction of nitrogen, decomposition is performed for B 1s (Figure 5.18) and C 1s (Figure 5.19) spectra. In order to improve the statistic, since the spectra of these two elements are rather noisy due to their low intensities compared to Pd and Y spectra, for each sample the spectra of different incident angles (ranging 1.8° around the first order Bragg angle) are summed up.

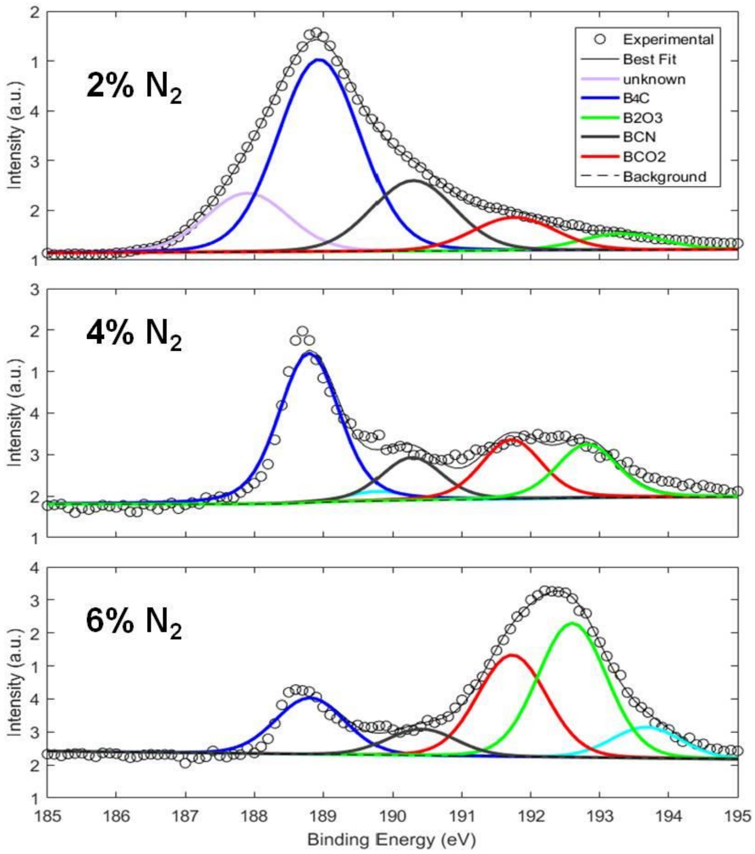

Figure 5.18: Decomposition of B 1s spectra of the samples.

There is an obvious relative intensity decrease of the B_4C and BCN component of the B 1s spectral peak as the nitrogen percentage increases, confirming the previous assumption of capping layer loss. The boron on the surface appears more as BCO_2 and B_2O_3.

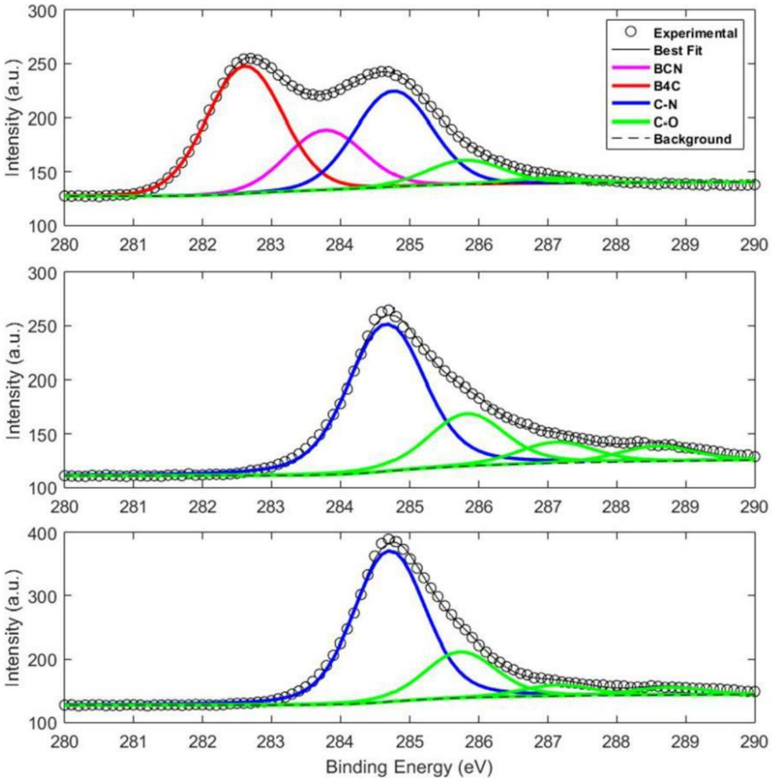

Figure 5.19: Decomposition of C 1s spectra of the samples.

We also look at the C 1s spectra. We find that when the N_2 percentage is 4%, the B_4C contribution is already invisible along with BCN. The organic contamination on the surface of the sample becomes dominant. The cap material loss is then further confirmed.

Particle induced X-ray emission

We present the Kossel curves for Pd Lα emission of this series of samples. To facilitate the comparison of the shapes of the curves, for each sample the origin of the detection angle is set to the Bragg angle, which corresponds to the center of its Kossel oscillation. Figure 5.20 shows the Kossel curves of the Pd/Y multilayers deposited with a proportion of N_2 within the argon sputtering gas ranging from 0 to 6%. For the Pd/Y multilayer grown in pure argon we observe no Kossel feature at all. This indicates that the intermixing is so severe that even the periodicity of the multilayer is compromised. As the proportion of N_2 increases, we start to observe the Kossel feature and its contrast (defined as the difference between the maximal and minimal intensity values as the detection angle crosses the Bragg angle) increases as well. As expected [68,69], the nitrogen has a positive effect in preventing or reducing the intermixing at the interfaces of the multilayer.

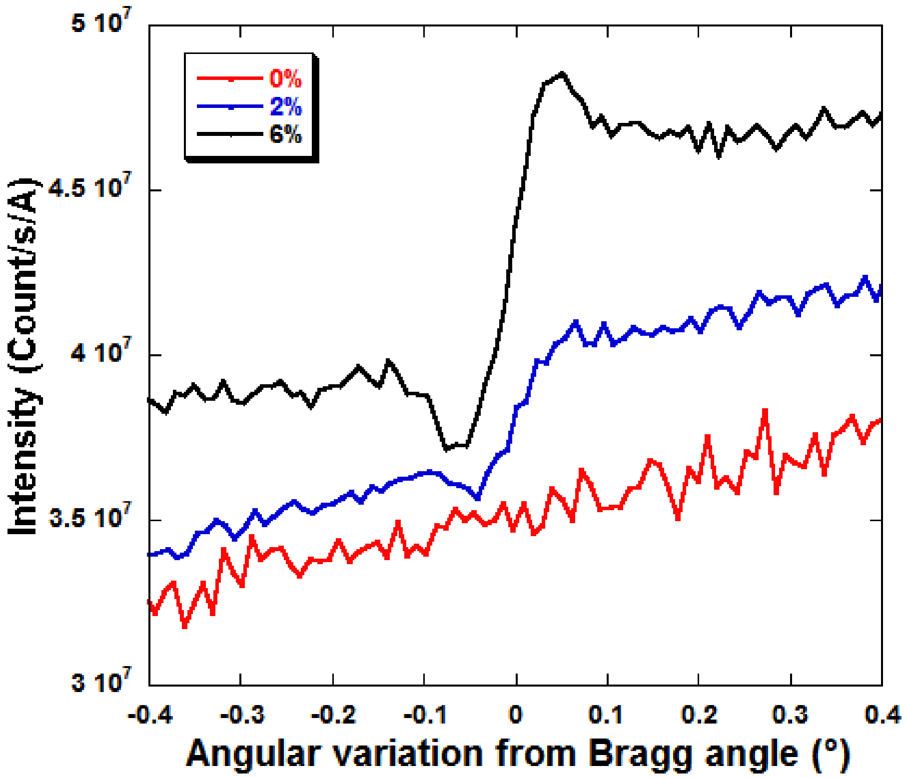

Figure 5.20: Kossel curves for Pd Lα emission of all measured samples of the series fabricated with different concentration of N_2 in the sputtering gas.

5.4.2 Pd/Y multilayer with B_4C barrier layers

Grazing incident reflectometry

The experimental and fitted GIXR curves are presented in Figure 5.21. The parameters, *i.e.* thickness and interface width of the various layers, of the samples are then extracted from the fitting procedure and are listed in Table 5.4. To distinguish the samples easily, in the following we use sample numbers as indicated in Table 5.4. The interface width in this table stands for both the geometrical roughness and the interdiffusion of the materials at the interfaces between the described layer and the previous one. For a Pd/Y multilayer modeled with perfect interfaces (no interface roughness nor interdiffusion), we expect a high reflectance as presented in Figure 5.21(A) (dotted line). However the interdiffusion, as predicted, is so severe that we barely observe the reflectance peak at the first order Bragg angle even seeing the curve in logarithm scale. The value of the interface width is almost as high as the layer thickness itself and the interferential contrast between different layers is almost completely lost. With B_4C layers as barriers, clear reflectivity patterns are observed for the other samples as presented in Figure 4. The interdiffusion is obviously reduced as we can read from Table 5.4. The fitting results show that the interdiffusion at Y-on-Pd interfaces (1.23 nm, sample 4) is stronger than the one at Pd-on-Y interfaces (0.80 nm, sample 3).

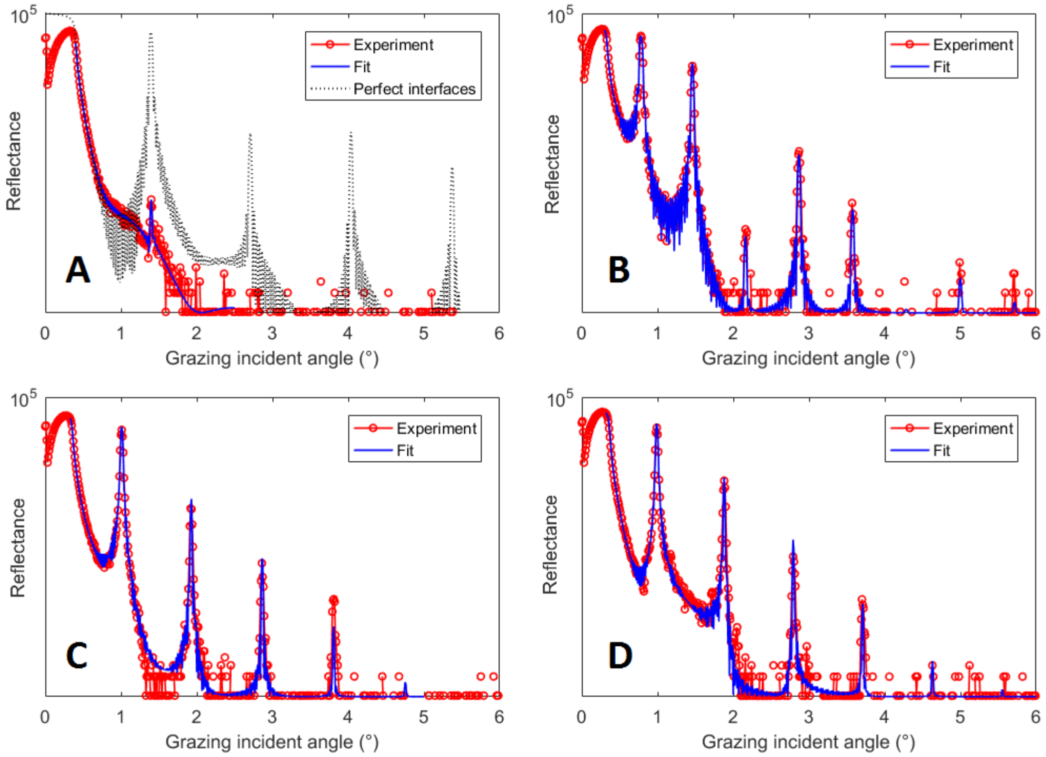

Figure 5.21: Measured (red dots) and fitted (blue lines) GIXR curves of the multilayers (logarithm scale). A: sample 1 (Pd/Y); B: sample 2 (B_4C/Pd/ B_4C/Y); C: sample 3 (B_4C/Pd/Y); D: sample 4 (Pd/ B_4C/Y). The dotted line in A presents the calculated reflectance of the original design without interface roughness nor interdiffusion.

Table 5.4: Designed structures and values of the parameters extracted from the fit of the experimental GIXR curves of the samples.

Sample	**Structure**	**Designed thickness (nm)**	**Thickness** (interface width) **(nm) extracted from the fit of GIXR curves**
1	$[Pd/Y]_{40}$	2/2	**1.87** (1.67) / **1.43** (1.35)
2	$[B_4C/Pd/B_4C/Y]_{20}$	1/2/1/2	**0.99** (0.35) / **2.10** (0.26) / **0.83** (0.27) / **2.29** (0.55)
3	$[B_4C/Pd/Y]_{40}$	1/2/2	**0.86** (0.34) / **2.30** (0.32) / **1.50** (0.80)
4	$[Pd/B_4C/Y]_{40}$	2/1/2	**2.19** (1.23) / **1.02** (0.30) / **1.57** (0.40)

HAXPES with 10 keV incident beam

As the 3 keV measurements mostly focus on the study of B_4C cap which is deposited for both series of samples, only 10 keV measurements are presented for the samples with interface barrier layers.

The angular variations of B 1s, Pd $2p_{3/2}$ and Y $2p_{3/2}$ photoemission spectra of the sample B_4C/Pd/B_4C/Y are presented in Figure 5.22(A)-(C). The B 1s spectra photoemission are rather noisy due to the much lower ionization cross section compared to the ones of Pd $2p_{3/2}$ and Y $2p_{3/2}$. The so-called HAXPES-XSW curves (Figure 5.22(D)) are depicted by integrating the intensity of the core level photoemission peaks and plotting the integrals as a function of the grazing angle. The integration of each photoemission peak takes into account the subtraction of a Shirley background. The photoemission spectra of Pd 3d and Y 3d core levels are also recorded at the same time but are not presented here because their HAXPES-XSW curves has approximately the same shape of the ones of 2p and will not bring additional information. There is ignorable minor difference which is due to the incertitude or acquisition statistic because of the low intensities of 3d core level peaks. Neither are the spectra of C 1s presented, owing to the surface contamination, as the samples are preserved in the atmosphere environment.

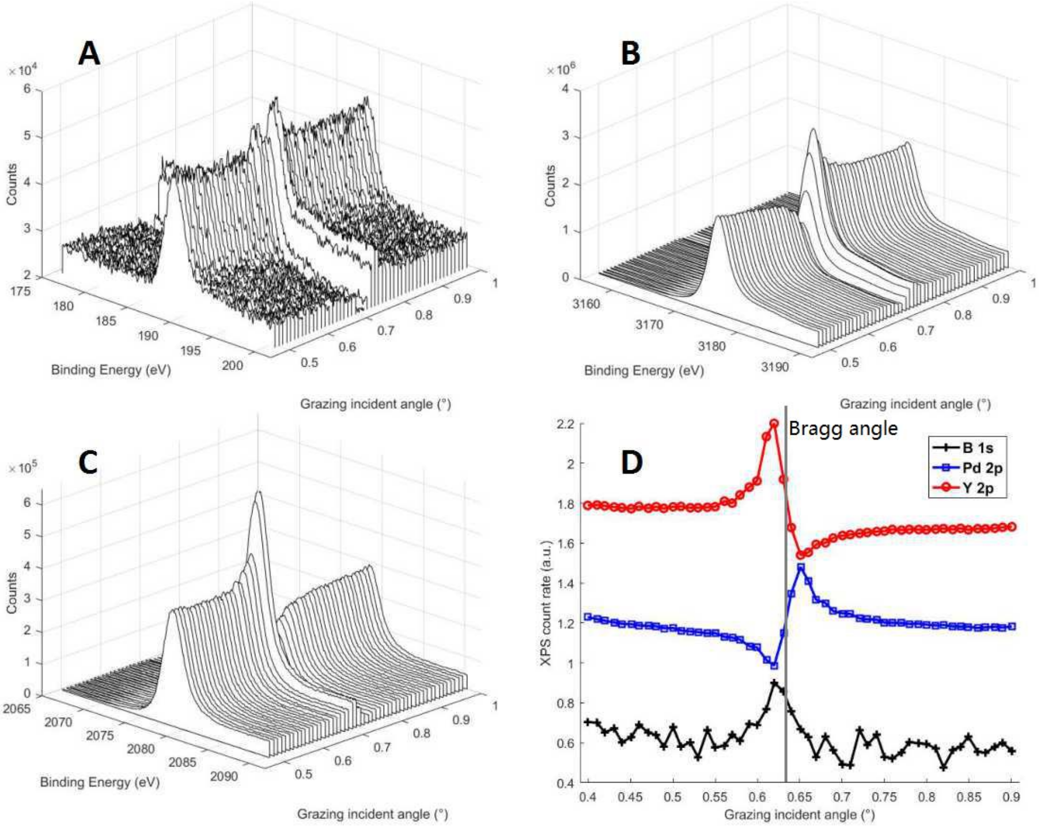

Figure 5.22: Photoemission spectra of the B_4C/Pd/B_4C/Y multilayer as a function of the grazing incident angle in the vicinity of the Bragg angle (grey solid line) for different core levels. A: B 1s, B: Pd $2p_{3/2}$, C: Y $2p_{3/2}$, D: the corresponding HAXPES-XSW curves.

The photoemission peaks are decomposed in order to obtain the depth distribution of different chemical states for each element. We are able to retrieve some information from the Pd $2p_{3/2}$ and Y $2p_{3/2}$ spectra whose quality is reliable. Pd $2p_{3/2}$ photoemission of sample 2 is presented in Figure 5.23(A) where four Voigt peaks are used to fit the experimental curve, which is the sum of the spectra of all angular values in order to gain precision. For the Voigt function, the Gaussian width is 2.00 eV, which is estimated from the bandwidth of the incident photon beam; the Lorentzian width is 2.05 eV, taken from the literature [77]. The Pd metal peak is found at 3175.2 eV in binding energy. We consider other peaks with higher binding energies as satellite peaks, as were reported by de Siervo [78]. The HAXPES-XSW curve related to each Pd $2p_{3/2}$ component (metal and satellites) is plotted in Figure 5.23(B). The angular dependent variations of the intensities of all the satellite peaks are superposed to the one of metal peak, indicating an identical depth distribution. We have considered the possibility that the peak located at 3176.7 eV (blue solid line in Figure 5.23(A), main contribution beside the Pd metal belongs to the Pd oxide. However, it is very unlikely that the oxide have the same depth distribution as the Pd metal. Indeed, the deposition of the samples is performed in pure argon. Thus the oxidation of the sample, if it penetrates the 2.5 nm B_4C capping layer and enters into the multilayer, may only happen from the surface. In this case, it would be expected to have a pronounced attenuation in the depth distribution. The observation of the identical depth distribution of each contribution of the photoemission spectrum is an evidence for the assumption that the other peaks are but satellites peaks. Since only one chemical state (metal) of Pd is found in the multilayer, the diffusion of Pd and B_4C layers does not form new chemical compound (Pd-B or Pd-C). The prediction by the positive enthalpy of formation of B_4C/Pd is confirmed. However we cannot tell if Pd and Y form any compound or alloy because even if they do, the binding energy of the alloy peak would be very close to the one of the metal peak. Given the current energy resolution, it is impossible to distinguish alloy and metal from the HAXPES spectra. The decomposition of Pd $2p_{3/2}$ photoemission spectra of other samples brings the same conclusion, thus is not presented here.

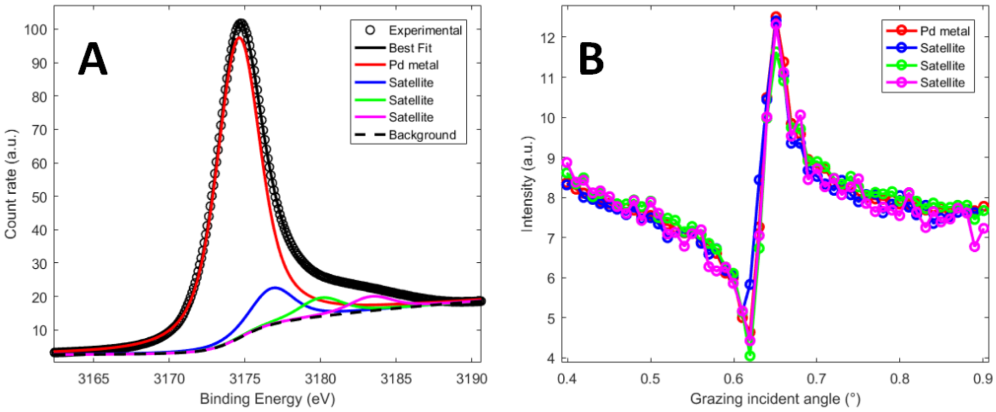

Figure 5.23: (A) decomposition of the sum of all Pd $2p_{3/2}$ photoemission spectra of sample 2 and (B) HAXPES-XSW curves of the corresponding components.

Analogous treatment is done for the Y $2p_{3/2}$ core level peak. The experimental spectrum is best fitted using 2 Voigt with 2.00 eV Gaussian width and 1.43 eV Lorentzian width [77]. As presented in Figure 5.24(A), the major component located at 2078.9 eV in binding energy should be Y metal. The oxidation does not penetrate into the Y layers as previously discussed. The peak which is found at 2081.6 eV stands for the chemical compound of either Y-C or Y-B. To explore the depth distribution of these two chemical states of Y, their HAXPES-XSW curves are depicted for samples 2, 3 and 4 in Figure 5.24(B)-(D) respectively. First we look at the curves of the sample 3 $[B_4C/Pd/Y]_{40}$ in Figure 5.24(C). Compared to Y metal, the HAXPES-XSW curve of the compound shifts towards the higher angles, indicating that such compound is located deeper than Y metal in each period. It is then located at the Y-on-B_4C interfaces. On the contrary, for the sample 4 $[Pd/B_4C/Y]_{40}$ in Figure 5.24(D), we have the angular shift of compound curve towards the lower angles. The compound is then located at a shallower depth than the Y metal, which should be the B_4C-on-Y interfaces. The unique appearance of such compound at Y-B_4C interfaces confirms our assumption of its nature: Y-B or Y-C. In the case of sample 2 $[B_4C/Pd/B_4C/Y]_{20}$ we have B_4C barrier layers on both sides of Y layer. In Figure 5.24(D), we observe an angular shift of the compound curve towards the lower angles. It means that the formation of this kind of Y compound has a preference, or is more active, to happen at B_4C-on-Y interfaces than at Y-on-B_4C interfaces. Like the Pd $2p_{3/2}$ spectra, Y $2p_{3/2}$ spectra cannot bring us information on whether there is any chemical compound formed at Pd-Y interfaces because it is not possible to distinguish the alloy peak from the metal peak on the HAXPES spectra. The HAXPES-XSW curves of C 1s and B 1s (not presented) are very noisy due to the low intensity of their photoemission spectra. As a consequence, we cannot tell if the Y compound is Y-B or Y-C.

The results obtained by HAXPES-XSW are in line with the values of enthalpy of formation ΔH_f found in the literature [74].

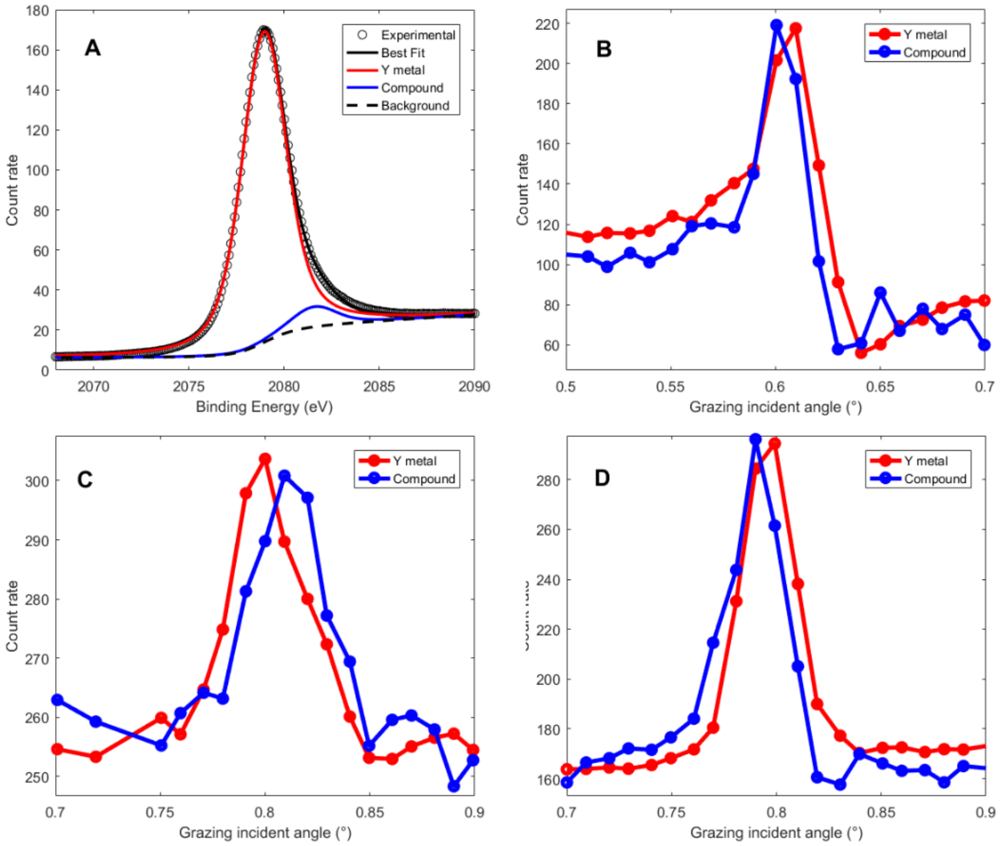

Figure 5.24: (A) decomposition of the sum of all Y $2p_{3/2}$ photoemission spectra of sample 2. HAXPES-XSW curves of the corresponding component peaks of different samples, (B) sample 2, (C) sample 3, (D) sample 4.

The structural parameters in Table 5.4 determined by GIXR fitting are introduced into the software YXRO [79] in order to calculate the variation of the photoemission intensity as a function of the grazing incident angle. The calculation takes into account of the complex refractive index of each material, the atomic cross section as well the structure of the multilayer. The IMFP of the photoelectrons is calculated by YXRO. Such prediction is presented in Figure 5.25 for sample 2 where the HAXPES-XSW curves of Pd $2p_{3/2}$, Y $2p_{3/2}$ and B 1s core levels are calculated. As seen in Figure 5.2(B), when the grazing incident angle is at the first order Bragg angle (0.63° for sample 2), the anti-nodal plans of the periodic X-ray standing wave field are located at Y-on-B_4C interfaces. Since both the multilayer and the electric field are periodic with an identical period value, the same field distribution can be expected for each period of the stack with the progressive loss of amplitude due to the attenuation of the radiation. When the incident angle varies through the Bragg angle, the location of the anti-nodal plans moves accordingly from Y layers into B_4C layers then Pd layers. This angular order of the ionization enhancement of the elements is reflected in Figure 5.25. As the grazing angle varies from low to high values, a rise of the Y $2p_{3/2}$ HAXPES-XSW curve first appears at 0.61°. It is then followed by the rise of the B 1s and Pd $2p_{3/2}$ curves at 0.63° and 0.66° respectively. As the B_4C layers are sandwiched between the Pd and Y layers, the B 1s HAXPES-XSW curve is rather more symmetrical instead of appearing as the “Z” form like the Pd and Y curves.

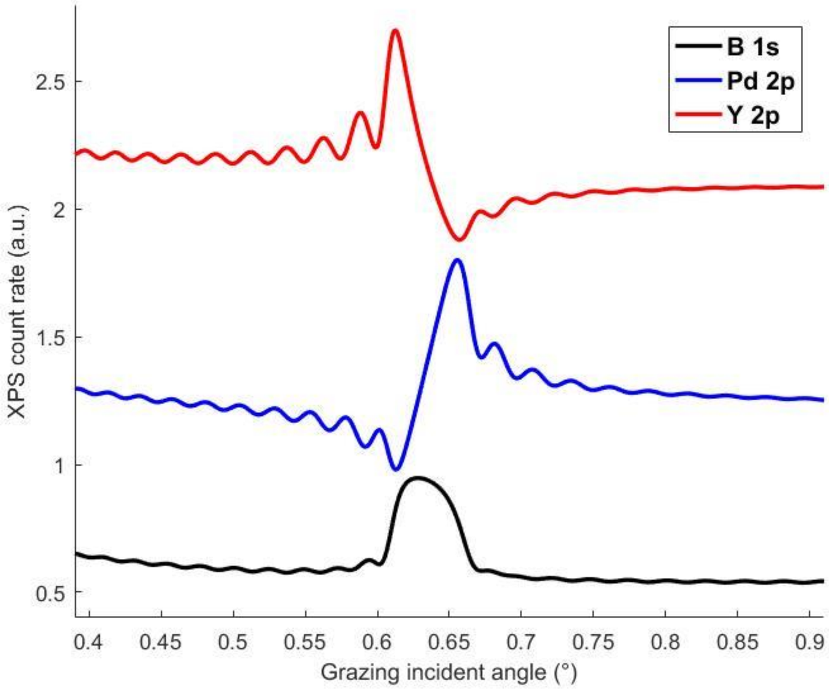

Figure 5.25: Simulation of the variation of the intensities of core level peaks for sample 2: B 1s in black, Pd $2p_{3/2}$ in blue and Y $2p_{3/2}$ in red. The curves are vertically shifted for the sake of readability.

Secondary oscillation of the calculated curves appears due to the interference between various reflections (so-called Kiessig fringes) resulted from the limited number of periods, which is 20 for sample 2. These simulations are far from what is experimentally observed (Figure 5.22(D)). This discrepancy is overcome by taking into account of the instrumental angular resolution (0.008°) and the horizontal divergence of the incident photon beam (0.026°). Such broadening can be mathematically simulated by applying a convolution by a gate function onto the simulation curve which is originally calculated with a step of 0.001°. The size of the gate function is then adjusted according to the angular resolution and beam divergence, and the effect is presented in Figure 5.26 in the case of the Y $2p_{3/2}$ HAXPES-

XSW curve. The Kiessig fringes disappear and the adjusted simulation shows a better agreement with the experimental data.

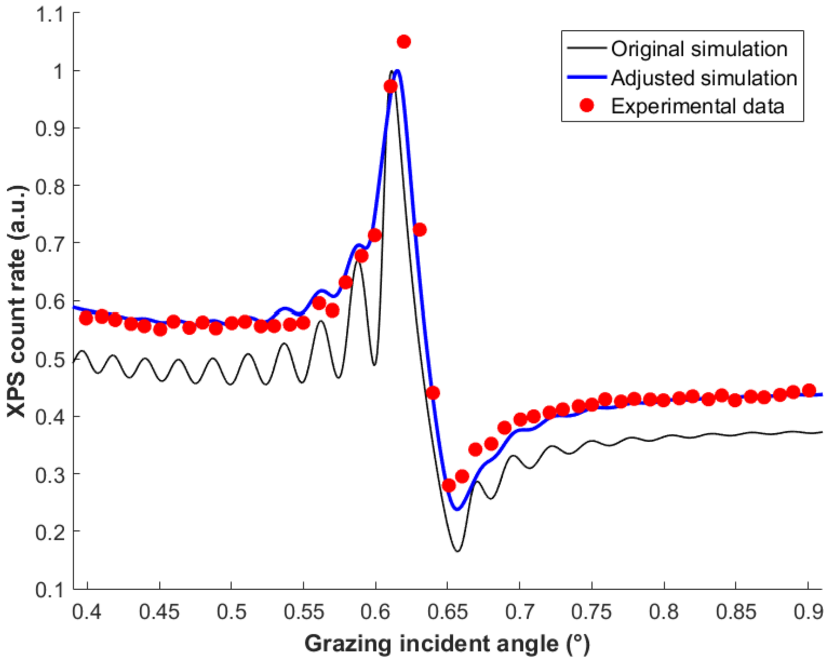

Figure 5.26: Comparison of the experimental (red dots) and calculated Y $2p_{3/2}$ HAXPES-XSW curves for the sample 2 with (blue line) and without (black line) angular broadening.

Figure 5.27 presents the HAXPES-XSW curves related to Pd 2p, Y 2p and B 1s peaks of sample 2 and their simulations with the broadening effect considered. The comparison shows a fine agreement indicating that the structure determined by GIXR is reliable as the shapes of these curves tightly correspond to the distribution of each element. For the other samples, the fitting of experimental curves based on the GIXR structural parameters the experimental curves is much less successful. The model used for GIXR fitting may be far too simple to describe the structure of the multilayer, especially concerning the depth distribution of all elements, even all chemical states. The reason that it works fine for sample 2 could be that the B_4C layers on each interface stabilize the multilayer by preventing the interdiffusion of Pd and Y atoms, making the situation relatively simpler compared to other samples. The model used for the GIXR fitting of such 4-layer sample is thus suitable in this case. Unfortunately for the moment we do not possess a fitting process to determine the structure of the multilayer independently.

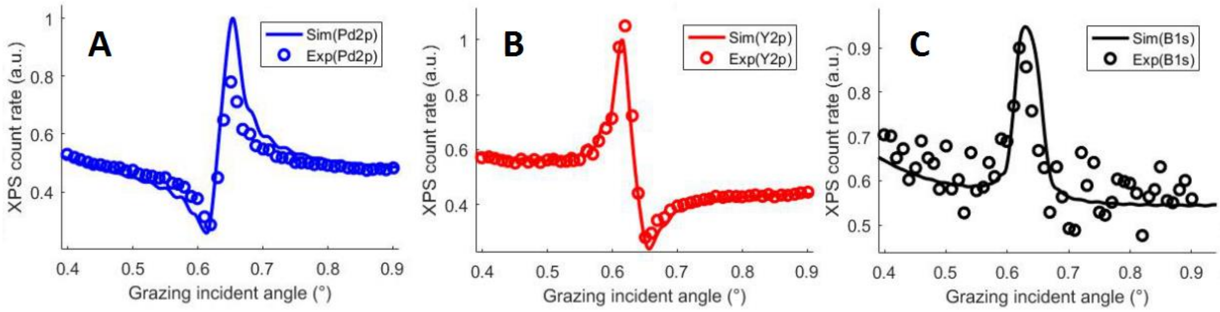

Figure 5.27: Comparison of experimental and simulated HAXPES-XSW curves for sample 2. A: Pd $2p_{3/2}$, B: Y $2p_{3/2}$ and C: B 1s.

Particle induced X-ray emission

We present the Kossel curves for Pd Lα emission of this series of samples. The origin of the detection angle is set to the Bragg angle for simplification as explained previously in Section 5.4.1. Figure 5.28 presents the Kossel curves of the multilayers with 1 nm B_4C diffusion barriers at one given interface or at both interfaces. The Kossel feature of each sample can be clearly observed. For the two samples with 1 nm B_4C barrier layer inserted at either Y-on-Pd or Pd-on-Y interfaces (noted as B4C/Pd/Y_122 and Pd/B4C/Y_212 respectively), the Kossel features are different when the detection angle is higher than the Bragg angle. The first one exhibits an intensity maximum at +0.05° while the latter shows rather flattened feature at the same angular position. When inserting 1 nm B_4C at both interfaces (the sample labeled as B4C/Pd/B4C/Y_1212), the intensity maximum at +0.05° become even more obvious, however at -0.05° the intensity decrease of the curve is more flattened than the two samples mentioned above. Here we do not present the sample mentioned in the previous section with 2 nm B_4C barrier layer because it is considered expendable for the long-time non-damaging test. Thus it is unsuitable to be put in the comparison series.

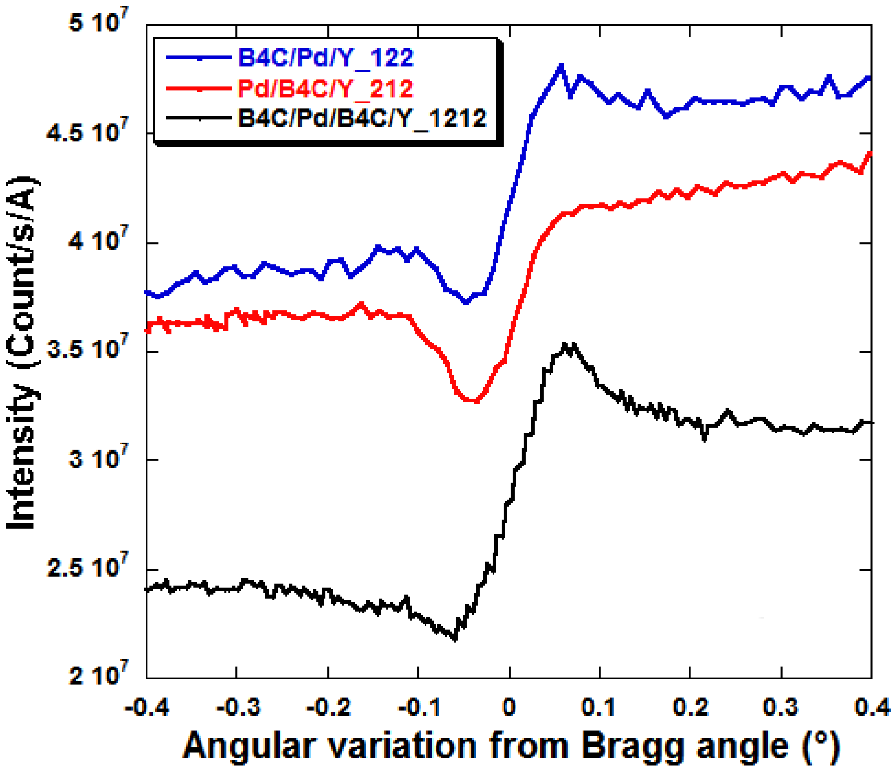

Figure 5.28: Kossel curves for Pd Lα emission of all measured samples of the series of samples with B4C barrier layers at one given interface or at both interfaces. The name of the samples refers both to the order of the layers within the period and to the thickness (in nm) of the individual layers.

To simulate the PIXE-Kossel curve, we build a model of the multilayer using the structural parameters (thickness and roughness of the layers) determined by grazing incident X-ray reflectivity. The simulation method is originally designed for X-ray fluorescence calculation under Kossel effect [27]. It calculates the electric field generated by the emitted X-ray within the multilayer under X-ray irradiation. We make an approach in order to adapt it to the PIXE-Kossel calculation. Since the ionization is uniform through the whole multilayer, we consider the incident proton beam as a photon beam with neither attenuation nor refraction. Such approach actually simplifies the calculation. An example of the simulation is given in Figure 5.29 where both experimental and simulated the PIXE-Kossel curves are presented in the near Bragg angle zone. The agreement is fairly good showing that the PIXE-Kossel curve can be used to determine the structure of multilayer stack.

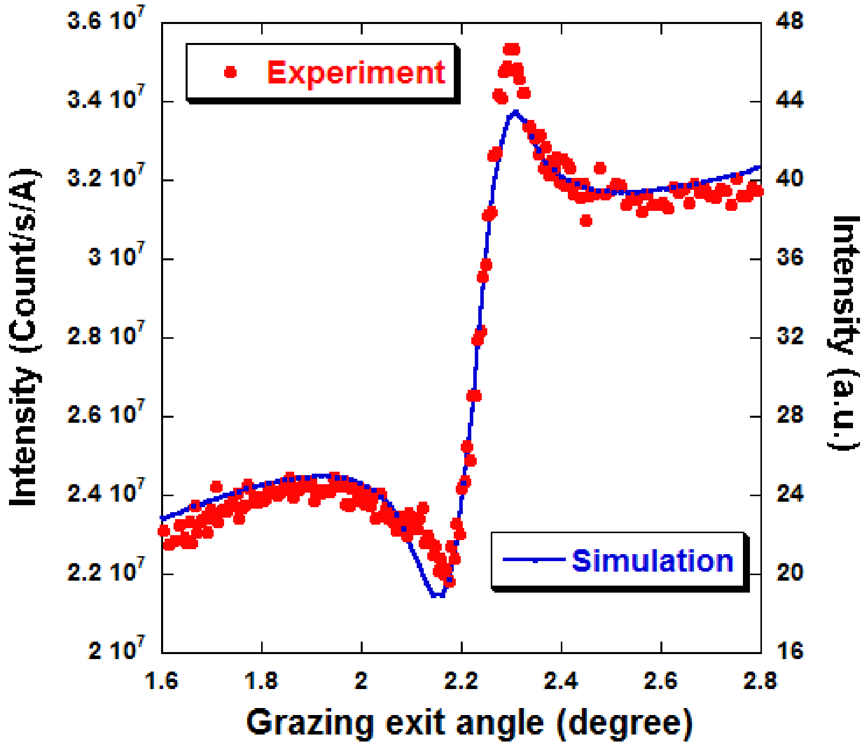

Figure 5.29: Comparison between experimental result and simulation of the PIXE-Kossel curves of the sample B_4C(2.5 nm)/[B_4C(1 nm)/Pd(2 nm)/B_4C(1 nm)/Y(2 nm)]$_{\times 20}$/Si.

5.5 Conclusions

The interdiffusion of the two metals in the Pd/Y system, predicted by calculating the mixing enthalpy using the Miedema model, is clearly observed by analyzing the GIXR measurements.

HAXPES-XSW curves are presented, measured at 3 and 10 keV of excitation energy, of each element present within a series of B_4C/[Pd/Y]$_{x40}$ multilayers differing by the amount of N_2 introduced in the sputtering gas during deposition. The B_4C capping layer is found to be thinner than expected due to the rise of B_4C sputtering yield as the nitrogen content increases in the sputtering gas during the deposition. The sputtering time was reduced in order to maintain the thickness of the capping layer, yet it was reduced too much. According to the XSW curves obtained by the decomposition of Y 3d photoemission spectrum, YN has a relatively sharpened interface against Pd compared to Y metal. The formation of YN could be the reason that the interdiffusion is reduced. Unfortunately, the O 1s and N 1s photoemissions are masked by the ones of Pd $3p_{3/2}$ and Y 3s respectively. In the future study of the oxidation or nitridation of the materials, it is suggested to avoid certain elements of which certain core levels possess similar electron binding energy with the ones of O and N. Such elements include but are not limited to Pd, Y (3s 392 eV), Mo ($3p_{3/2}$ 394 eV), Sc ($3p_{3/2}$ 398 eV), ...

To study the efficiency of the insertion of B_4C barrier layer at one or both interfaces, B_4C/Pd/Y, Pd/B_4C/Y and B_4C/Pd/B_4C/Y multilayers are also considered. The thickness and roughness/interdiffusion of the Pd and Y layers in these series are determined by fitting the experimental GIXR spectra. The interfaces are found to be asymmetrical since interdiffusion is stronger at Y-on-Pd interfaces than at Pd-on-Y interfaces. The HAXPES-XSW measurements further help explore the nature of the interdiffusion of Pd and Y. The interdiffusion of Pd into the B_4C layers does not form any chemical compound. On the contrary, Y forms chemical compound with either B or C at the Y-B_4C interfaces. The formation of Y compound has a preference, or is more active, to happen at B_4C-on-Y interfaces than at Y-on-B_4C interfaces. Such chemical compound can be the reason why the interfaces are stabilized. A detailed description of the depth distribution of each element can be obtained by comparing the HAXPES-XSW curves with the calculations using YXRO. However a fitting process is in need in order to independently build up a model of the multilayer to determine its structure.

We have further proven the feasibility of using proton induced X-ray emission combined with Kossel diffraction to characterize the structure of nanometric multilayers. We have measured the Kossel diffraction of proton induced Pd Lα emission in Pd/Y based multilayers. Compared to our previous experiment [80], we have significantly improved the data acquisition with the X-ray color camera. We also demonstrate here that the shape of the Kossel curve is very sensitive to the detailed structure of the multilayer and its interface. In particular we confirm that nitridation during the multilayer deposition process has a positive effect in preventing or reducing the interdiffusion between Pd and Y layers, and we further show that Pd/Y based multilayers with B_4C barrier layers at different interfaces can be distinguished by the shape of their Kossel curves.

5.6 Related publications

The contents of this chapter are based on the following publications:

[1] Wu M-Y, Ilakovac V, André J-M, Le Guen K, Giglia A, Rueff J-P, Huang Q-S, Wang Z-S and Jonnard P. Study of Pd/Y based multilayers using high energy photoemission spectroscopy combined with x-ray standing waves. *Proceeding of SPIE*, 102350F, 2017.

[2] Wu M-Y, Le Guen K, André J-M, Jonnard P, Vickridge I, Schmaus D, Briand E, Walter P, Huang Q-S, Wang Z-S. Kossel diffraction observed with X-ray color camera during PIXE of nano-scale periodic multilayer. *Nuclear Instruments and Methods in Physics Research Section B: Beam Interactions with Materials and Atoms*, 2018 (in press).

[3] Wu M-Y, Huang Q-S, Le Guen K, Ilakovac V, Li B-X, Wang Z-S, Giglia A, Rueff J-P and Jonnard P. Characterization of Pd/Y multilayers with B_4C barrier layers using GIXR and x-ray standing wave enhanced HAXPES. *Journal of Synchrotron Radiation*, 25, 1417, 2018.

Chapter 6: Conclusion and perspectives

In this thesis, the X-ray standing wave technique, a non-destructive depth sensitive characterization method, has been applied to the study of periodic multilayer mirrors. Other experimental methods such as X-ray reflectivity and Rutherford backscattering of the protons were also reported as complementary techniques. Two systems, Cr/Sc and Pd/Y, were studied along with their derivatives.

For Cr/Sc based periodic mutilayer mirrors, their performances were tested by measuring the reflectance of the photon beam with the working energy (395 eV) for which these multilayers were designed. B_4C barrier layers were found to be more effective at Sc-on-Cr interfaces than at Cr-on-Sc interfaces to improve the performance of the mirror, making the reflectance increase by approximately three times. There was evidence that the introduction of nitrogen in the sputtering gas had positive effect, approximately doubled reflectance. By fitting the XRR data with simulation, structures of the multilayers were determined, including the layer thicknesses and interface roughness/interdiffusion. XRF-XSW has been applied onto one of the samples (Cr/CrB_4C/Sc) by calculating the theoretical XRF-XSW curve using the structural parameters determined by XRR fitting. The agreement between the simulated and experimentally obtained XRF-XSW curves has successfully confirmed the multilayer structure. With the same sample, we have observed for the first time the Kossel interference of proton induced X-ray emission in a multilayer by measuring the intensity variation of the Sc Kα and Cr Kα characteristic emissions as a function of detection angle. The developed PIXE-Kossel method could be a useful means for multilayer study with its own advantage compared to other characterization techniques.

The study of Pd/Y based multilayer mirrors contains two major parts: HAXPES-XSW and PIXE-Kossel. HAXPES-XSW revealed the elemental distribution of the elements present within the stacks. For the series of samples deposited in mixing sputtering gas (Ar and certain percentage of N_2), the B_4C capping layer was found to be thinner than expected due to the influence of N_2 to the B_4C sputtering yield. According to the XSW curves obtained by the decomposition of Y 3d photoemission spectrum, YN had a relatively sharpened interface against Pd compared to Y metal. The formation of YN could be the reason that the interdiffusion is reduced. In the future study of the oxidation or nitridation of the materials, it is suggested not to certain elements of which certain core levels possess similar electron binding energy with the ones of O and N in order to avoid spectral masking. Further analysis of the HAXPES-XSW curves helped explore the nature of the interdiffusion of Pd and Y into the B_4C barrier layer. The interdiffusion of Pd into the B_4C layers did not form any chemical compound. On the contrary, Y formed chemical compound with either B or C at the Y-B_4C interfaces. The formation of Y compound had a preference, or was more active, to happen at B_4C-on-Y interfaces than at Y-on-B_4C interfaces. Such chemical compound could be the reason why the interfaces were stabilized. A detailed description of the depth distribution of each element could be obtained by comparing the HAXPES-XSW curves with the calculations using YXRO. The feasibility of PIXE-Kossel method has been further proven. As a critical improvement a X-ray color camera was introduced to the instrumental setup, significantly improving the quality of the data acquisition compared to the previous experiment with Cr/Sc based multilayer. The obtained PIXE-Kossel curves, with their shapes sensitive to the structures of the corresponding multilayers, were compared to the simulations. From a practical point of view, the nitridation of the multilayer had a positive effect in preventing or reducing the interdiffusion between Pd and Y layers, and the Pd/Y based multilayers with B_4C barrier layers at different interfaces could be distinguished by the shape of their Kossel curves.

For perspectives, there are another two research projects going on as the study of the thesis approaches its end. The first project concerns the study of X-ray magnetic dichroism (XMCD) modulated by X-ray standing wave in a Mg/Co periodic multilayer. Such characterization method aims to study the interfaces of magnetic and periodic hetero-structures. XMCD enables the method to be sensitive to the magnetic character of the atoms present within the stack while XSW provides the depth sensitivity. It would be the first experimental proof of XMCD in X-ray emission and standing wave regime. A first testing experiment has been performed at Optics beamline of BESSY II synchrotron radiation facility. As presented in Figure 6.1, the intensity difference depending on the helicity of the light was clearly observed on the absorption spectrum of a magnetized Co/Mg multilayer recorded in the energy region around Co $L_{2,3}$ absorption edge. The absorption of right circularly polarized light (R) is higher than the left one (L) at Co L_3 edge, yet weaker at Co L_2 edge. However the dichroic effect was not as strong as expected [81] due to a too weak magnetization, as we simply used a permanent magnet, to reach the saturation value. Three energy values of the incident X-ray beam were selected, represented with the three black bars in Figure 6.1, in order to generate the fluorescence of Co atoms. They correspond to the previously mentioned Co absorption edges and an extra energy far over them. The angular dependence of the fluorescence intensity is presented in Figure 6.2, with both R and L circularly polarized light. Such result lacked critical success as dichroic effect could be hardly seen with the XCMD-XSW curves. Further study is being planned to improve the experimental condition in order to obtain better data.

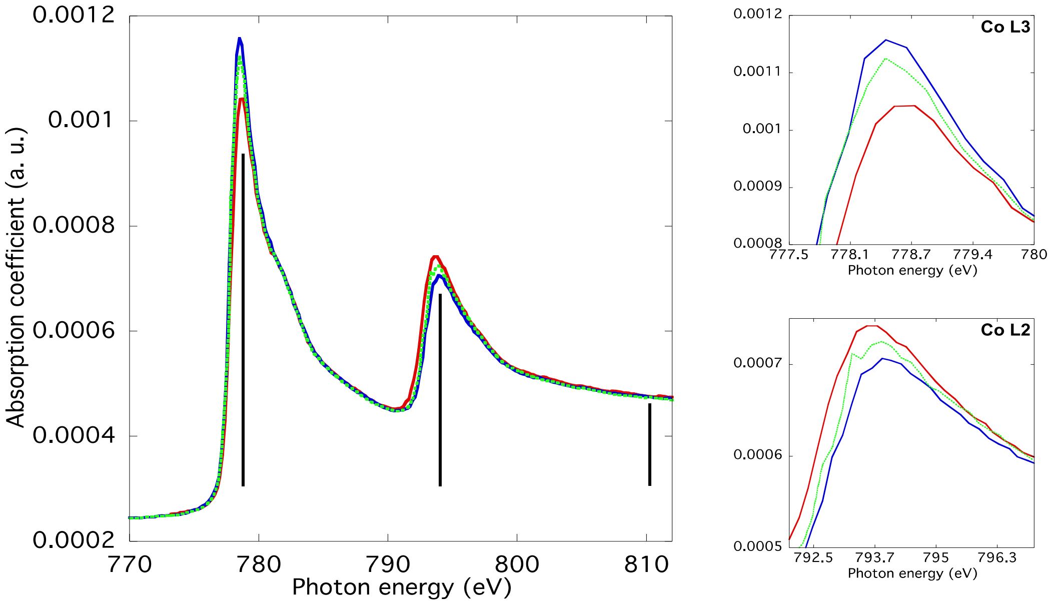

Figure. 6.1: Dichroism of the Co $L_{2,3}$ absorption spectrum of the magnetized Co/Mg multilayer obtained with left (red line) and right (blue line) circularly polarized radiations. The three vertical bars show the three incident photon energies chosen to perform the fluorescence measurements. The insets show the regions of the Co L_3 and L_2 maxima. For comparison, the measurement obtained with linear radiation (green line) is also shown.

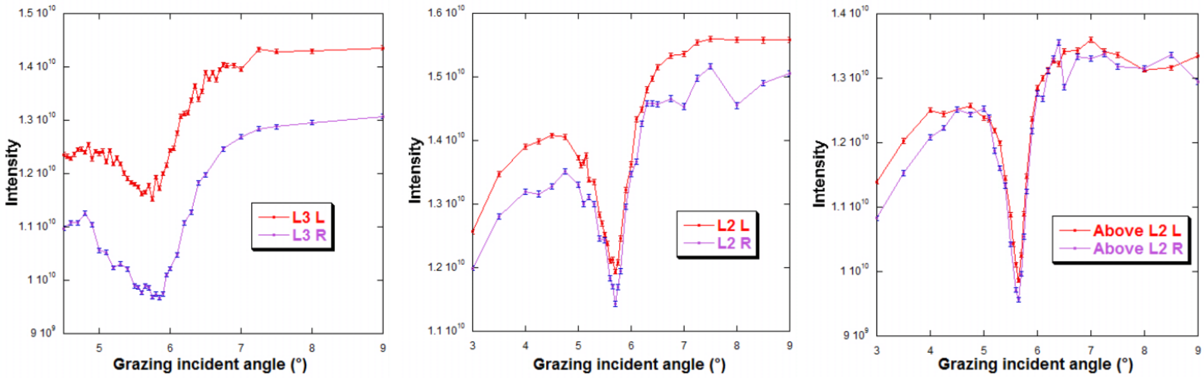

Figure. 6.2: XCMD-XSW of Co L emission of the magnetized Co/Mg generated with the three selected incident X-ray energies respectively with both left and right polarizations.

The second ongoing project concerns the study of X-ray standing wave modulated X-ray fluorescence and Kossel diffraction of periodic multilayer using a laboratory radiation source. As our collaborators in BLiX in Berlin has proven the possibility of a scan-free grazing exit mode XRF measurements in the laboratory using a CCD [82], we believe that such experimental setup is suitable to perform standard XSW or Kossel diffraction measurements as well. The preliminary results are quite promising as the oscillation of the X-ray emission intensity is observed due to XSW modulation. Some untreated raw data is presented in Figure 6.3. Further data analysis is in process.

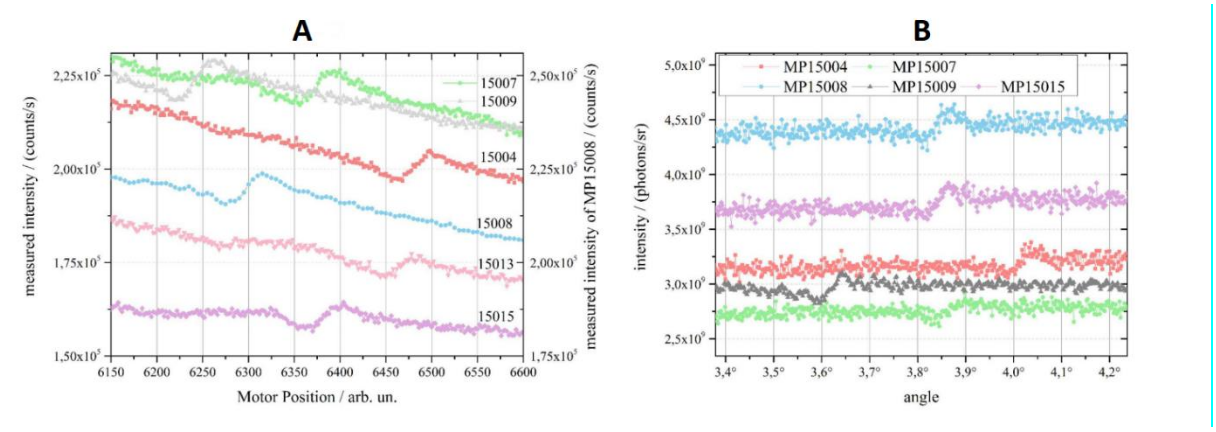

Figure. 6.3: Angular dependence of Cr Kα emission: (A) standard XSW (motor position is proportional to angular position) and (B) Kossel diffraction. Copyright Veonika Szwedowski, Technical University of Berlin.

Besides, a fitting process for the experimental data is in need to analyse the XSW/Kossel curves. For the instance, the standing wave techniques have provided valuable information of the studied multilayer systems. However, concerning the structure determination, we still rely on reflectance measurement and analysis. Although the theoretical calculation is already realized by running the simulation codes as demonstrated in this thesis (FLUORT for XRF-XSW and PIXE-Kossel, YXRO for HAXPES-XSW), the codes by themselves are unable to perform curve fitting to determine the multilayer structure independently. Curve fitting code combining the simulations codes is necessary and would push the limit of the power of X-ray standing wave techniques.

Other publications

Publications as co-author:

[1] André J-M, Jonnard P, Le Guen K, Wu M-Y, Dhawan R, Singh A, Modi M H, Lépy M-C, Ménesguen Y and Novikova A. Yoneda effect in planar x-ray waveguide. *VUVX2016 Zurich conference paper*.

[2] Le Guen K, André J-M, Wu M-Y, Ilakovac V, Delmotte F, de Rossi S, Bridou F, Meltchakov E, Giglia A, Nannarone S, Wang Z-S, Huang Q-S, Zhang Z, Zhu J-T, Tu Y-C, Yuan Y-Y, Vickridge I, Schmaus D, Briand E, Steydli S and Jonnard P. Kossel effect in periodic multilayers. *Jounal of Nanoscience and Nanotechnology* (submitted).

[3] Huang Q, Yi Q, Cao Z, Qi R, Loch R A, Jonnard P, Wu M, Giglia A, Li W, Louis E, Bijkerk F, Zhang Z and Wang Z. High reflectance Soft X-ray V/Sc multilayer mirror for the water window region. *Scientific Reports*, 7 (1), 2017.

[4] Jonnard P, André J-M, Le Guen K, Wu M, Principi E, Simoncig A, Gessini A, Mincigrucci R, Masciovecchio C and Peyrusse O. EUV stimulated emission from MgO pumped by FEL pulses. *Structural Dynamics*, 4 (5), 054306, 2017.

[5] Jonnard P, André J-M, Le Guen K, Wu M, Principi E, Simoncig A, Gessini A, Mincigrucci R, Masciovecchio C and Peyrusse O. Amplified spontaneous and stimulated Mg L emissions from MgO pumped by FEL pulses. *Proceeding of SPIE*, 102430D, 2017.

[6] P. Jonnard, M. Wu, J.-M. André, K. Le Guen, Z. Wang, Q. Huang, I. Vickridge, D. Schmaus, E. Briand, S. Steydli, and P. Walter, *Review of Scientific Instruments*, 89(9), 096109, 2018.

References

---

[1] Crookes W. On the illumination of lines of molecular pressure, and the trajectory of molecules. *Philosophical Transactions of the Royal Society*. 170, 135–164 (1878).

[2] Kevles B H. Naked to the Bone Medical Imaging in the Twentieth Century. Camden, NJ. Rutgers University Press. pp. 19–22 (1996). ISBN 0-8135-2358-3.

[3] Henke B L, Gullikson E M, and Davis J C. X-ray interactions: photoabsorption, scattering, transmission, and reflection at E=50-30000 eV, Z=1-92. *Atomic Data and Nuclear Data Tables*, 54 (2) 181-342, 1993.

[4] Stenzel O. Optical Coatings. Berlin, Heidelberg: Springer Berlin Heidelberg, vol. 54, 2014.

[5] Makhotkin I A. Structural and reflective characteristics of multilayers for 6.x nm wavelength. Enschede, University of Twente, 2013.

[6] Born M and Wolf E. Principles of optics. 1999: Cambridge University Press.

[7] Bräuer G, Szyszka B, Vergöhl M and Bandorf R. Magnetron sputtering – Milestones of 30 years. *Vacuum*, 84, 1354–1359, 2010.

[8] https://patents.google.com/patent/US4166018A/en

[9] De Stasio G *et al.*. Feasibility tests of transmission x-ray photoelectron emission microscopy of wet samples. *Review of Scientific Instruments*, 71 (1), 11–14, 2000.

[10] Adam J-F, Moy J-P, and Susini J. Table-top water window transmission x-ray microscopy: Review of the key issues, and conceptual design of an instrument for biology. *Review of Scientific Instruments*, 76 (9), 091301, 2005.

[11] Friedrich W, Knipping P, von Laue M. Interferenz-Erscheinungen bei Röntgenstrahlen". Sitzungsberichte der Mathematisch-Physikalischen Classe der Königlich-Bayerischen Akademie der Wissenschaften zu München. 303, 1912.

[12] Bragg W H, Bragg W L. The Reflexion of X-rays by Crystals. *Proceedings of the Royal Society of London. Series A*. 88 (605), 428–438, 1913.

[13] Batterman B W, Cole H. Dynamical Diffraction of X-rays by Perfect Crystals. *Reviews of Modern Physics*, 36, 681, 1964.

---

[14] Zegenhagen J, Kazimirov A. The X-ray Standing Wave Technique: Principles and Applications, World Scientific, 2013.

[15] Kossel W, Loeck V, Voges H. Die Richtungsverteilung der in einem Kristall entstandenen charakteristischen Röntgenstrahlung. *Zeitschrift für Physik*. 94, 139–144, 1935.

[16] Gog T, Novikov D, Falta J, Hille A and Materlik G. Kossel diffraction and X-ray standing waves: two birds of one feather. *Le Journal de Physique IV*, 4, C9–449, 1994.

[17] Schetelich C, Brenner S, Geist V. Laue and Kossel diffraction on quasicrystals by means of synchrotron radiation. *Journal of Synchrotron Radiation*, 5, 102–106, 1998.

[18] https://www.elettra.trieste.it/it/lightsources/elettra/elettra-beamlines/bear/bear.html

[19] Nannarone S. The BEAR Beamline at Elettra. *AIP Conference Proceedings*, 705, 450–453, 2004.

[20] https://www.synchrotron-soleil.fr/fr/lignes-de-lumiere/galaxies

[21] Céolin D, Ablett J M, Prieur D, Moreno T, Rueff J-P, Marchenko T, Journel L, Guillemin R, Pilette B, Marin T and Simon M. Hard X-ray photoelectron spectroscopy on the GALAXIES beamline at the SOLEIL synchrotron. *Journal of Electron Spectroscopy and Related Phenomena*, 190, 188–192, 2013.

[22] Langer E, Däbritz S. 75 years of Kossel patterns - past and future. *IOP Conference Series: Materials Science and Engineering*. 7, 01215, 2010.

[23] Lider V V. X-ray divergent-beam (Kossel) technique: A review. *Crystallography Reports*. 56, 169–189, 2011.

[24] Jonnard P, André J-M, Bonnelle C, Bridou F, Pardo B. Modulation of x-ray line intensity emitted by a periodic structure under electron excitation. *Applied Physics Letters*, 81, 1524–1526, 2002.

[25] Jonnard P, André J-M, Bonnelle C, Bridou F, Pardo B. Soft-x-ray Kossel structures from W/C multilayers under various electron ionization conditions. *Physical Review A*, 68, 32505, 2003.

[26] André J-M, Jonnard P, Pardo B. Radiation emitted by an oscillating dipole embedded in a periodic stratified structure: A direct matrix analysis. *Physical Review A*, 70, 12503, 2004.

[27] Chauvineau J-P, Hainaut O, Bridou F. Lignes de Kossel observées avec des multicouches périodiques Fe/C. *Le Journal de Physique IV*, 6, C4-773, 1996.

[28] Chuev M A, Koval'chuk M V, Kvardakov V V, Medvedev P G, Pashaev E M, Subbotin I A, Yakunin S N. Direct observation of anomalous Kossel lines. *Journal of Experimental and Theoretical Physics Letters*, 91, 191–195, 2010.

[29] Marchesini S, Belakhovsky M, Baron A Q R, Faigel G, Tegze M, Kamp P, Standing waves and Kossel line patterns in structure determination, *Solid State Communications*, 105, 685–687, 1998.

[30] Jonnard P, Yuan Y-Y, Le Guen K, André J-M, Zhu J-T, Wang Z-S, Bridou F. Spontaneous soft x-ray fluorescence from a superlattice under Kossel diffraction conditions. *Journal of Physics B: Atomic, Molecular and Optical Physics*, 47, 165601, 2014.

[31] Tu Y-C, Yuan Y-Y, Le Guen K, André J-M, Zhu J-T, Wang Z-S, Bridou F, Giglia A and Jonnard P. X-ray fluorescence induced by standing waves in the grazing-incidence and grazing-exit modes: study of the Mg–Co–Zr system. *Journal of synchrotron radiation*, 22, 1419–1425, 2015.

[32] Geist V, Flagmeyer R. The influence of the crystal lattice on the angular distribution of X-rays emitted from a GaP single crystal by fast proton bombardment. Physica Status Solidi A, 26, K1–K3, 1974.

[33] Roberto J B, Batterman B W, Kostroun V O, Appleton B R, Positive−ion−induced Kossel lines in copper. *Journal of Applied Physics*, 46, 936–937, 1975.

[34] Geist V, Flagmeyer R, Stephan D, Ullrich H-J. Kossel interferences of proton-induced Al Kα radiation. *Physica Status Solid A*, 40, 113–117, 1977.

[35] Geist V, Flagmeyer R, Otto G. Investigation of lattice deformation in proton bombarded GaP and ZnSiP2 by means of the proton-induced kossel effect. *Physics Letters A*, 64, 421–422, 1978.

[36] Geist V, Ehrlich C H, Flagmeyer R, Ullrich H-J, Greiner W, Rolle S. Investigation of GaN heteroepitaxial layers by means of the kossel effect technique. *Crystal Research and Technology*, 17, 245–251, 1982.

[37] Rickards J. Crystallography using the diffraction of proton induced X-rays. *Nuclear Instruments and Methods in Physics Research Section B: Beam Interactions with Materials and Atoms*, 24, 621–624, 1987.

[38] Schetelich C, Weber S, Geist V, Schlaubitz M, Ullrich H J, Kek S, Krane H G. Recording of Kossel patterns using monochromatic synchrotron radiation. *Nuclear*

Instruments and Methods in Physics Research Section B: Beam Interactions with Materials and Atoms, 103, 236–242, 1995.

[39] Drouin D, Couture A R, Joly D, Tastet X, Aimez V and Gauvin R. CASINO V2.42—A Fast and Easy-to-use Modeling Tool for Scanning Electron Microscopy and Microanalysis Users. *Scanning*, 29 (3), 92–101, 2007.

[40] Ziegler J F, Biersack J P and Ziegler M D. SRIM - The Stopping and Range of Ions in Matter. SRIM Co., 2008.

[41] Windt D L. IMD—Software for modeling the optical properties of multilayer films. *Computers in Physics*, 12(4), 360, 1998.

[42] http://xdb.lbl.gov/

[43] Powell C J, Jablonski A. Evaluation of Calculated and Measured Electron Inelastic Mean Free Paths Near Solid Surfaces. *Journal of Physical and Chemical Reference Data*, 28, 19–62, 1999.

[44] Ashley J C and Williams M W. Electron mean free paths in solid organic insulators. *Radiation Research*, 81, 364–373, 1980.

[45] Tanuma J, Powell C J, Penn D R. Calculations of electron inelastic mean free paths (IMFPS). IV. Evaluation of calculated IMFPs and of the predictive IMFP formula TPP-2 for electron energies between 50 and 2000 eV. *Surface and Interface Analysis,* 21, 165, 1993.

[46] Cumpson P J. Estimation of inelastic mean free paths for polymers and other organic materials: use of quantitative structure–property relationships. *Surface and Interface Analysis,* 31, 23–34, 2001.

[47] Gries W H. A Universal Predictive Equation for the Inelastic Mean Free Pathlengths of X-ray Photoelectrons and Auger Electrons. *Surface and Interface Analysis,* 24, 38-50, 1996.

[48] Fadley C S. Hard X-ray Photoemission: An Overview and Future Perspective, in: J. Woicik (Ed.), Hard X-Ray Photoelectron Spectroscopy (HAXPES), Springer International Publishing, Cham, 1–34, 2016.

[49] Fadley C S. Hard X-ray photoemission with angular resolution and standing-wave excitation. *Journal of Electron Spectroscopy and Related Phenomena*, 190, 165–179, 2013.

[50] Burcklen C, de Rossi S, Meltchakov E, Dennetière D, Capitanio B, Polack F and Delmotte F. High-reflectance magnetron-sputtered scandium-based x-ray multilayer mirrors for the water window. *Optics Letters*, 42, 1927, 2017.

[51] Prasciolu M, Leontowich A F G, Beyerlein K R and Bajt S. Thermal stability studies of short period Sc/Cr and Sc/B_4C/Cr multilayers. *Applied Optics,* 53, 2126, 2014.

[52] Bajt S, Alameda J B, Barbee T W, Clift W M, Folta J A, Kaufmann B B and Spiller E A. Improved reflectance and stability of Mo/Si multilayers. *Optical Engineering*, 41, 1797, 2002.

[53] S. Braun, Foltyn T, van Loyen L, Moss M, Leson A. *Proceedings of SPIE*, 5037, 274, 2003.

[54] Jankowski A F, Saw C K, Walton C C, Hayes J P and Nilsen J. Boron–carbide barrier layers in scandium–silicon multilayers. *Thin Solid Films*, 469–470, 372–6, 2004.

[55] Jonnard P, Maury H, Le Guen K, André J-M, Mahne N, Giglia A, Nannarone S and Bridou F. Effect of B4C diffusion barriers on the thermal stability of Sc/Si periodic multilayers. *Surface Science*, 604, 1015–21, 2010.

[56] Kjornrattanawanich B, Windt D L and Seely J F. Normal-incidence silicon–gadolinium multilayers for imaging at 63 nm wavelength. *Optics Letters*, 33, 965, 2008.

[57] Le Guen K, Hu M-H, André J-M, Jonnard P, Zhou S K, Li H C, Zhu J T, Wang Z S, Mahne N, Giglia A and Nannarone S. Introduction of Zr in nanometric periodic Mg/Co multilayers. *Applied Physics A*, 102, 69–77, 2011.

[58] Larruquert J I. Reflectance optimization of inhomogeneous coatings with continuous variation of the complex refractive index. *Journal of the Optical Society of America A*, 23, 99–107, 2006.

[59] Eriksson F, Ghafoor N, Hultman L and Brich J. Reflectivity and structural evolution of Cr/Sc and nitrogen containing Cr/Sc multilayers during thermal annealing. *Journal of Applied Physics*, 104, 063516, 2008.

[60] Larruquert J I. New layer-by-layer multilayer design method. *Journal of the Optical Society of America A*, 19 (2), 385–390, 2002.

[61] Burcklen C, Soufli R, Dennetiere D, Polack F, Capitanio B, Gullikson E, Meltchakov E, Thomasset M, Jérome A, de Rossi S and Delmotte F. Cr/B_4C multilayer mirrors: Study of interfaces and X-ray reflectance Journal of Applied Physics. 119 (12), 125307, 2016.

[62] Jonnard P, Bonnelle C. Cauchois and Sénémaud Tables of wavelengths of X-ray emission lines and absorption edges. *X-Ray Spectrometry*, 40, 12–16, 2011.

[63] Chambet Y, Etude experimentale de la diffusion des rayons x rasants par les multicouches pour optiques X-UV, PhD thesis, Université Paris 11, 1993.

---

[64] Haase A, Bajt S, Hönicke P, Soltwisch V and Scholze F. Multiparameter characterization of subnanometre Cr/Sc multilayers based on complementary measurements. *Journal of Applied Crystallography*, 49, 2161–2171, 2016.

[65] Ordavo I, Ihle S, Arkadiev V, Scharf O, Soltau H, Bjeoumikhov A, Bjeoumikhova S, Buzanich G, Gubzhokov R, Günther A, Hartmann R, Holl P, Kimmel N, Kühbacher M, Lang M, Langhoff N, Liebel A, Radtke M, Reinholz U, Riesemeier H, Schaller G, Schopper F, Strüder L, Thamm C and Wedell R. A new pnCCD-based color X-ray camera for fast spatial and energy-resolved measurements. *Nuclear Instruments and Methods in Physics Research Section A: Accelerators, Spectrometers, Detectors and Associated Equipment*, 654, 250–257, 2011.

[66] Montcalm C, Kearney P A, Slaughter J M, Sullivan B T, Chaker M, Pépin H and Falco C M. Survey of Ti-, B-, and Y-based soft x-ray–extreme ultraviolet multilayer mirrors for the 2- to 12-nm wavelength region. *Applied optics*, 35, 5134–5147, 1996.

[67] Corso A J, Zuppella P, Windt D L, Zangrando M, Pelizzo M G. Extreme ultraviolet multilayer for the FERMI@Elettra free electron laser beam transport system. *Optics Express*, 20(7), 8006, 2012.

[68] Xu D, Huang Q, Wang Y, Li P, Wen M, Jonnard P, Giglia A, Kozhevnikov I V, Wang K, Zhang Z and Wang Z. Enhancement of soft X-ray reflectivity and interface stability in nitridated Pd/Y multilayer mirrors. *Optics Express*, 23, 33018, 2015.

[69] Wu M-Y, Ilakovac V, Andr? J-M, Le Guen K, Giglia A, Rueff J-P, Huang Q-S, Wang Z-S and Jonnard P. Study of Pd/Y based multilayers using high energy photoemission spectroscopy combined with x-ray standing waves. *Proceedings of SPIE*, 102350F, 2017.

[70] Windt D L and Gullikson E M. Pd/B_4C/Y multilayer coatings for extreme ultraviolet applications near 10 nm wavelength. *Applied Optics*, 54, 5850, 2015.

[71] Miedema A R, De Chatel P F and De Boer F R. Cohesion in alloys—fundamentals of a semi-empirical model. *Physica B+C*, 100, 1–28, 1980.

[72] Yuan Y, Le Guen K, André J-M, Mény C, Ulhaq C, Galtayries A, Zhu J, Wang Z and Jonnard P. Interface observation of heat-treated Co/Mo2C multilayers. *Applied Surface Science*, 331, 8–16, 2015.

[73] Kardellass S, Selhaoui N, Iddaoudi A, Ait Amar M, Karioui R and Bouirden L. Thermodynamic assessment of the Pd–Y binary system. *MATEC Web of Conferences*, 5, 04032, 2013.

[74] Meschel S V and Kleppa O J. Thermochemistry of alloys of transition metals and lanthanide metals with some IIIB and IVB elements in the periodic table. *Journal of Alloys and Compounds*, 321, 183–200, 2001.

[75] Scofield J H. Theoretical photoionization cross sections from 1 to 1500 keV. Lawrence Livermore National Laboratory Rep. UCRL-51326, 1973.

[76] Shirley D A. High-resolution X-ray photoemission spectrum of the valence bands of gold. *Physical Review B,* 5, 4709, 1972.

[77] Campbell J L and Papp T. WIDTHS OF THE ATOMIC K–N7 LEVELS. *Atomic Data and Nuclear Data Tables*. 77, 1–56, 2001.

[78] De Siervo A, Landers R, De Castro S G C and Kleiman G G. Measurement of the 2p XPS spectra of 4d metals: Nb to Sb. *Journal of electron spectroscopy and related phenomena*, 88, 429–433, 1998.

[79] Yang S-H, Gray A X, Kaiser A M, Mun B S, Sell B C, Kortright J B and Fadley C S. Making use of x-ray optical effects in photoelectron-, Auger electron-, and x-ray emission spectroscopies: Total reflection, standing-wave excitation, and resonant effects. *Journal of Applied Physics*, 113, 073513, 2013.

[80] Wu M, Le Guen K, André J-M, Ilakovac V, Vickridge I, Schmaus D, Briand E, Steydli S, Burcklen C, Bridou F, Meltchakov E, de Rossi S, Delmotte F and Jonnard P. Kossel interferences of proton-induced X-ray emission lines in periodic multilayers. *Nuclear Instruments and Methods in Physics Research Section B: Beam Interactions with Materials and Atoms*, 386, 39–43, 2016.

[81] D. Zhu, Lensless Holography Methods for Soft X-ray Resonant Coherent Imaging, PhD Thesis, Stanford University, 2010.

[82] Szwedowski V, Baumann J, Mantouvalou I, Bauer L, Malzer W and Kanngie B. Scan-Free Grazing Emission XRF Measurements in the Laboratory Using a CCD Phys. *Status Solidi*, C, 6, 2017.

WU Meiyi – Thèse de doctorat - 2018

Développement de la méthodologie des ondes stationnaires pour sonder les processus physico-chimiques aux interfaces des multicouches périodiques

Résumé :

La qualité des interfaces dans les multicouches périodiques est essentielle au développement de miroirs réfléchissant efficacement dans les domaines des rayons X et extrême ultraviolet (X-EUV). De manière générale, la structure des interfaces dépend des possibles interdiffusion et processus chimiques aux interfaces entre couches. L'idée principale de cette thèse est d'appliquer la technique des ondes stationnaires dans le domaine X à la caractérisation de matériaux, principalement mais non exclusivement aux multicouches périodiques. Cette méthode est basée sur l'interférence de deux faisceaux de rayons X cohérents. L'interférence constructive sur un plan anti-nodal amplifie le champ électrique tandis que l'interférence destructive minimise ce dernier sur un plan nodal. Cette technique des ondes stationnaires dans le domaine X permet l'excitation (photoémission, fluorescence, ...) d'endroits spécifiques dans un empilement périodique de matériaux. De cette manière, les spectres expérimentaux ainsi obtenus sont principalement les spectres caractéristiques des atomes situés sur un plan anti-nodal. Combinée avec d'autres techniques expérimentales telles que la spectroscopie d'émission X (XES) ou la spectroscopie de photoélectrons dans le domaine X (XPS), une information sélective en profondeur, avec une sensibilité sub-nanométrique, peut être obtenue.

Mots clés : multicouches périodiques, ondes stationnaires de rayons X, diffraction de Bragg, réflectivité des rayons X, fluorescence X, diffraction de Kossel, spectroscopie de photoémission par rayons X durs, émission de rayons X induite par des particules.

Development of the X-ray standing waves methodology to probe the interfaces of periodic multilayers

Abstract :

The interfacial information of periodic multilayers can be crucial for the development of reflecting mirrors which operate in the X-ray and extreme ultraviolet (X-EUV) ranges. Such information may contain the interdiffusion and chemical process at the interfaces of the layers. The idea of this thesis is to apply the X-ray standing wave technique to the characterization of materials, mainly but not limited to the periodic multilayers. X-ray standing wave technique enables to enhance the excitation (photoemission, fluorescence etc.) of specific locations within a periodic stack. The nature of such advantage is the interference of two coherent X-ray beams. One may compare the X-ray standing waves with the mechanical standing waves. The constructive interference at the anti-nodal plane amplifies the electric field; while the destructive interference at the nodal plane minimizes the electric field. In this way, the experimental spectra obtained under standing wave field will be mostly the material located on the anti-nodal plane. Combined with other techniques such as X-ray emission spectroscopy and X-ray photoelectron spectroscopy, a depth-selective information with a sub-nanoscale sensitivity can be obtained.

Keywords : periodic multilayers, X-ray standing waves, Bragg diffraction, X-ray reflectivity, X-ray fluorescence, Kossel diffraction, hard X-ray photoemission spectroscopy, particle-induced X-ray emission.